FRACTURE TOUGHNESS AND FATIGUE CRACK GROWTH RATE CHARACTERIZATION OF IN718 FORMED BY LASER POWDER BED FUSION

THESIS

Charles C. Hohnbaum, Captain, USAF

AFIT-ENY-MS-19-M-220

DEPARTMENT OF THE AIR FORCE
AIR UNIVERSITY

AIR FORCE INSTITUTE OF TECHNOLOGY

Wright-Patterson Air Force Base, Ohio

AFIT-ENY-MS-19-M-220

FRACTURE TOUGHNESS AND FATIGUE CRACK GROWTH RATE CHARACTERIZATION OF IN718 FORMED BY LASER POWDER BED FUSION

THESIS

Presented to the Faculty
Department of Aeronautics and Astronautics
Graduate School of Engineering and Management
Air Force Institute of Technology
Air University
Air Education and Training Command
in Partial Fulfillment of the Requirements for the
Degree of Master of Science in Materials Science

Charles C. Hohnbaum, B.S. Mat.E.
Captain, USAF

21 March 2019

AFIT-ENY-MS-19-M-220

FRACTURE TOUGHNESS AND FATIGUE CRACK GROWTH RATE CHARACTERIZATION OF IN718 FORMED BY LASER POWDER BED FUSION

Charles C. Hohnbaum, B.S. Mat.E.
Captain, USAF

Committee Membership:

Maj Ryan O'Hara, PhD
Chair

Maj Ryan Kemnitz, PhD
Member

Reji John, PhD
Member

AFIT-ENY-MS-19-M-220

Abstract

Continuing improvement in the field of Additive Manufacturing (AM) of metals provides the opportunity for direct fabrication of aerospace parts. AM was once used in large part for rapid prototyping but improvements in technology and increases in the knowledge base of AM materials has provided the opportunity for manufacture of AM parts for operational use. The ability to create low numbers of unique parts without having to invest in expensive tooling provides great economic incentive to utilize this technique. Inconel 718 (IN718) is the most common high temperature alloy used in the aerospace industry and lends itself readily to formation by Laser Powder Bed Fusion (LPBF). The superior strength of IN718 at temperatures up to 650°C and its excellent corrosion resistance make it the alloy of choice for compressor blades in jet turbines. Extensive data exists for conventionally produced IN718 but gaps in the data are present for AM material. Two of these gaps that are addressed by this research are Fracture Toughness (FT) and Fatigue Crack Growth Rate (FCGR). A primary driver of the differences in behavior between conventionally manufactured and AM IN718 are the microstructural differences. Conventionally produced material has an equiaxed microstructure that provides isotropic material behavior. Conversely production by AM methods results in a highly directional microstructure related to the build direction of the part that drives anisotropy in material performance. It is hypothesized that a modified heat treatment that allows for re-crystallization of the columnar grains to grains that are more equiaxed will mitigate anisotropic material effects. This research will characterize the FCGR of As-Built (AB), Conventional Heat Treatment (CHT), and Modified Heat Treatment (MHT) conditions. Results of FCGR indicate the the MHT is successful at reducing

the overall FCGR of LPBF IN718. The standard heat treatment for wrought IN718 is shown to increase anisotropy in FCGR and give no improvement to the FCGR when compared to material in the AB condition.

Acknowledgments

This research would not have come to fruition without the assistance of many individuals and organizations. First without the support of my wife I surely would have turned into a basket case before finishing this project. My parents also deserve recognition for their early influence in instilling values and habits that would eventually lead me to continue pursuing my education. In the academic realm thanks goes out to my research advisor Maj Ryan O'Hara for his support in procuring resources and demystifying the black magic that is computer coding. Support by Ben Doane, Greg Cobb, Travis Shelton, and Megan Hartsfield allowed for the precise and rapid production of the 3D printed parts for this project. In the lab Jamie Smith and Mike Ranft were constantly available to provide assistance with testing machinery and ensured its functionality. Brian Crabtree and the team of machinists at the AFIT Model Shop were instrumental in applying their depth of skill to provide timely productions of test parts designed to exacting specifications. Maj David Newell developed the heat treating process that was central to this work and provided hours of consultation to the author to add to the understanding IN718. Dr. Reji John and Steve Thompson of AFRL lent invaluable technical knowledge in the field of fatigue and fracture testing and evaluation without which this research would never have reached its final form. Finally nothing that was accomplished would have been possible if the author had not known the saving power of Jesus Christ. It is through his power that I am the man I am today. All glory belongs to Him.

Charles C. Hohnbaum

Table of Contents

List of Figures

List of Tables

List of Symbols

α	Ratio of Crack Length to Specimen Width
ΔK	Stress Intensity FactorF Range
ΔP	Force Range
$\Delta\sigma$	Applied Stress Range
γ	Surface Energy
Π	Potential Energy
σ_f	Fracture Stress
σ_y	Yield Stress
σ_{ij}	Stress Tensor Near a Crack Tip
$\frac{da}{dN}$	Rate of Crack Extension
ε_{ij}	Strain Tensor Near a Crack Tip
a_c	Critical Crack Length for Propagation
a_c	Critical Crack Length
a_f	Final Crack Length
a_o	Initial Crack Length
k_1	Proportionality Constant
k_2	Proportionality Constant
K_P	Applied Stress Intensity Factor During Precracking
K_{IC}	Critical Stress Intensity Factor
K_{MAX}	Maximum Applied Stress Intensity Factor
N_f	Fatigue Crack Growth Life
u_x	Plane Stress Elastic Compliance for CT Specimens
A	Crack Area
a	Crack Length
B	Specimen Thickness
B	Specimen Thickness
C	Critical Strain Energy Release Rate
C	Power Law Coefficient
CMOD	Crack Mouth Opening Displacement
E	Elastic Modulus
J	J-integral
K	Stress Intensity Factor
m	Power Law Coefficient
n	Strain Hardening Exponent
P	Applied Load
R	Stress Ratio
r	Crack Tip Radius
W	Specimen Width
Y	Geometry Factor for an Edge Crack in an Infinite Medium
Y	Specimen Geometry Factor

FRACTURE TOUGHNESS AND FATIGUE CRACK GROWTH RATE CHARACTERIZATION OF IN718 FORMED BY LASER POWDER BED FUSION

I. INTRODUCTION

1.1 Background

Continuing improvement in the field of Additive Manufacturing (AM) of metals provides the opportunity for direct fabrication of aerospace parts. AM was once used in large part for rapid prototyping but improvements in technology and increases in the knowledge base of AM materials has provided the opportunity for manufacture of AM parts for operational use [15]. The ability to create low numbers of unique parts without having to invest in expensive tooling provides great economic incentive to utilize this technique[16]. Inconel 718 (IN718) is the most common high temperature alloy used in the aerospace industry and lends itself readily to formation by Laser Powder Bed Fusion (LPBF)[17]. The superior strength of IN718 at temperatures up to 650°C and its excellent corrosion resistance make it the alloy of choice for compressor blades in jet turbines[17]. While Ti-6AL-4V exhibits a better strength to weight ratio than IN718 its service ceiling is 450°C[18] make it unacceptable for higher temperature applications. Extensive data exists for conventionally produced IN718 but gaps in the data are present for AM material. Two of these gaps that are addressed by this research are Fracture Toughness (FT) and Fatigue Crack Growth Rate (FCGR). A primary driver of the differences in behavior between conventionally manufactured and AM IN718 are the microstructural differences. Conventionally produced material typically has an equiaxed microstructure that provides isotropic material behavior[1]. Some conventionally produced materials do display directional behavior. Rolled plate and extruded materials display elongated grains in the direction of rolling or extrusion and these can affect material performance in a desirable or undesirable manner[19]. Production by AM methods results in a highly directional microstructure related to the build direction of the part that drives a degree of anisotropy in material performance[10]. It is hypothesized that a modified heat treatment that allows for re-crystallization of the columnar grains to grains that are more equiaxed will mitigate anisotropic material effects. This research will characterize the FCGR of As-Built (AB), Conventional Heat Treatment (CHT), and Modified Heat Treatment (MHT) conditions [4]. Initial work has been completed on FCGR in AM IN718[13] but full investigation of the three chosen build orientations compounded with various heat treatments remains to be completed. This research aims to add to the knowledge base on LPBF IN718 in the areas of FT and FCGR.

1.2 Problem

Materials produced by AM show great promise in engineering applications, but in many cases AM material behavior differs from conventionally produced material making direct implementation of AM parts impractical. IN718 manufactured by LPBF forms very small grains with columnar behavior in the direction of the build[20]. This induces an undesirable degree of directional dependence on strength. Due to the cooling dynamics of the LPBF method AM parts also retain significant residual stresses which can deform parts and further detriment the material performance[21]. This leads to a degree of unpredictability in material behavior which is unacceptable in the design of critical flight components. IN718 gains much of its strength from the growth of γ precipitates. These precipitates are composed of Ni_3Nb and prevent grain boundary sliding and dislocation motion. These precipitates are not present in the as-built microstructure and their absence leads to degraded material properties. In the case of tensile strength as-built materials will fail at a value nearly 40% lower than wrought material[22]. The lack of data available to engineers prevents AM techniques from being used to their full capability in the aerospace industry. For the Air Force the ability to rapidly produce replacement components for aging aircraft whose supply lines were shut down long ago provides a great incentive to characterize the behavior of AM material and certify it for use. The potential to have on site fabrication of critical parts especially in a deployed environment could increase the mission availability and decrease costs. However, without a better understanding of the material behavior, none of these benefits can be leveraged.

1.3 Research Questions and Objectives

The purpose of this research is to characterize the FT and FCGR rate as influenced by specimen build orientation and heat treatment for IN718 manufactured by LPBF. Three specific orientations and heat treatments will be considered in this research. The results of these test conditions will provide insight that will be used to answer the following questions:

- How does specimen build orientation affect FT and FCGR?
- Does the MHT remove the specimen build orientation dependence of FT and FCGR?
- Does the MHT provide improvements to FT and FCGR in all specimen build orientations?

1.4 Justification for Research

The United States Air Force has a vested and growing interest in the use of additive manufacturing. AM parts are already being used in operational aircraft, but these parts remain in non-flight-critical roles such as seat covers and other cosmetic functions due to a lack of understanding of how AM parts compare to traditionally manufactured parts. In the future the Air Force hopes to utilize AM to manufacture innovative designs and structural components that require no post production machining. The flexibility of AM allows for rapid on-site fixes to unexpected problems. Another benefit of AM is the ability to produce small production runs that traditionally would have inflated costs due to machining set up and tooling costs, while AM parts can be produced on an as needed basis without the need to restart a production line. With a rapidly aging fleet of aircraft the Air Force often faces difficulties sourcing spare parts that rely on production lines and tooling that were destroyed years ago. The ability to manufacture new parts with nothing but a Computer-Aided Design (CAD) drawing and availability of a printer allows for aircraft to have higher operational rates for an extended lifetime at reasonable costs. However until AM material can be effectively characterized and behavior reliably predicted the full capability of this technology will remain constrained. This research aims to close knowledge gaps in the area of FT and FCGR for IN718 manufactured by LPBF.

Characterization of the FT and FCGR of IN718 manufactured by IN718 is one of the necessary steps to prove out its capability for use in applications associated with cyclic loading conditions. Study of the as-built and heat treated conditions provides data for use with and without post-production processing. The results of this research will be used to increase the body of understanding of AM IN718 for both military and civilian applications.

1.5 Scope

This research will focus on the characterization of the FT and FCGR IN718 manufactured by LPBF in three specimen build orientations and three heat treatments at room temperature. Most IN718 production is largely consumed by the aerospace, nuclear, and oil drilling industries due to its strength and corrosion resistance over a wide range of temperatures (-217°C to 650°C)[23]. Determination of the FT and FCGR at room temperature can provide a baseline for AM parts to meet some performance requirements and to pave the way for future high temperature testing. Experimental measurement of the FT and FCGR rate will lead to a better understanding of the material behavior of IN718. Testing in both the as-built and two heat treated forms will allow for optimization of processing techniques based on design requirements. Testing of all three specimen build orientations will identify FT and FCGR differences between specimen build orientations and whether the heat treatment processes effectively remove anisotropy in these material performance measures.

1.6 Assumptions

The primary assumption associated with this research is that specimen build orientation will affect the FT and FCGR of IN718. This assumption is based on the microstructural directionality in AM parts. It is predicted that specimens with the columnar grains aligned along the crack direction will display lower FT and higher FCGR. The alignment of the crack and the long direction of the grains should allow cracks to propagate along grain boundaries at reduced stress levels. A second assumption of the project is that the CHT will not equiax the grain structure in such a way as to make the specimens behave in an isotropic manner. Both the CHT and MHT will promote the growth of γ" precipitates. As a result specimens with these two heat treatments will display higher FT and decreased FCGR when compared to the AB specimens. It is assumed that the CHT specimens will be stronger than both AB and MHT specimens in the directions where the crack grows perpendicular to the build direction but weaker than the MHT condition as the crack grows along the build direction. Heat treatment and specimen build orientation will be the only independent variables in the test to keep the scope of the project limited.

1.7 Approach

Two main experiments will be conducted in this thesis. The first of which is FT testing of the AM IN718 material. The second test will measure the FCGR of the same material with the goal of creating a power law equation to model material behavior as demonstrated by Paris[24]. The purpose for conducting FT testing first is to ensure that the FCGR tests are performed at the appropriate loading levels. FT values are used to calculate the upper load applied during fatigue testing and must be determined prior to beginning the second phase of testing. FT testing is modeled on the the procedures outlined in American Society for Testing and Materials E1820-17a (ASTM E1820-17a)[11] using Compact Tension (C(T)) specimens. FCGR testing was modeled on the procedures outlined in American Society for Testing and Materials E647-15 (ASTM E647-15)[12] using C(T) specimens. Several deviations from these standards were required to meet the needs of this research and are detailed in Chapter III. Heat treatment of the CHT and MHT specimens was conducted as specified in American Society for Testing and Materials B637 (ASTM B637) and by a heat treatment profile modified to optimizes material behavior for AM IN718 parts[4]. These experiments should ideally produce data usable by engineering to optimize the performance of IN718 manufactured by LPBF.

II. BACKGROUND

2.1 Chapter 2 Overview

In this chapter, the background of project will be discussed. A review of Inconel 718 (IN718) as an aerospace alloy will be reviewed along with a summary of its known material behavior. A brief discussion of Additive Manufacturing (AM) will be conducted focusing on Laser Powder Bed Fusion (LPBF) methods. The field of elastic plastic fracture mechanics is particularly relevant to this thesis specifically involving fracture and fatigue as methods of failure and will be discussed in detail. Common trends can be seen in many materials relating the morphology of the microstructure to anticipated mechanical properties, discussion on instances of these trends will be discussed in AM materials and conventionally produced materials. The mechanisms of their operation and suitability of conventionally produced IN718 will be covered.

2.2 Inconel 718

Developed in the 1940's, Inconel alloys are designed to operate in the corrosive high temperature environment of jet turbines. These alloys are composed primarily of nickel and chromium with various alloying elements added to tailor specific material behavior. Since their creation various changes have been made to optimize the alloy for specific uses. Created in 1960 by Huntington Alloys[17], IN718 is a precipitation hardened variant of the Inconel family which is designed for higher strength and higher temperature operation. The alloy is named because of the aging process that creates these precipitates. When held at 718°C for 8 hrs precipitates of Ni_3Nb, commonly referred to as γ", will form[14]. Inconel alloys are well known for their survivability in a wide range of corrosive environments. Nickel provides corrosion resistance against organic and inorganic solutions throughout a wide range of acidic and basic environments and is resistant to chloride induced stress corrosion cracking. Chromium provides strong oxidation protection and resists attack by sulfur[25]. IN718 is a valuable aerospace alloy that fills a critical role in jet turbines and has the potential to expand its capabilities through AM.

2.2.1 Basic Properties

In many ways the mechanical properties of Inconel are similar to many high strength steel alloys. To meet the standards of American Society for Testing and Materials B637 (ASTM B637), annealed and aged IN718 should meet or exceed the standards in Table 2.2. Compared to 4340 steel it is approximately 7% denser, has a 6% greater modulus of elasticity, and has lower yield strength and ultimate tensile strength compared with quenched and tempered steel.These properties put IN718 in the same range as many Ti alloys and high strength steels. IN718 stands out due to its high temperature capabilities. The ceiling for Ti-6Al-4V is 450 °C, for 316L stainless steel 566 °C[26], and for 7075 Al 149 °C[27]. As stated previously, IN718 retains much of its material strength up to 650 °C. Even at these elevated temperatures IN718 retains excellent corrosion resistance and mechanical strength. IN718 responds well to welding and can be roll formed or cast. IN718 is a precipitation hardened alloy and requires and aging heat treatment to achieve the desired mechanical properties. More on precipitation hardening will be discussed in Section 2.3.2. The recommended heat treatment procedures are listed in Table 2.3. Due to the high hardness of the alloy after precipitation hardening, manufacturers recommend machining to near final conditions in the annealed state with final machining after aging[25]. The chemical composition of IN718 can be seen in Table 2.1. The material properties of IN718 allow for a broad range of engineering applications and drive the desire to use it in the AM form.

Table 2.1. Chemical Composition of IN718 [14]

Element	**C**	**Mn**	**Si**	**P**	**S**	**Cr**	**Co**	**Ni**
Composition Percent	0.08 max	0.035 max	0.035 max	0.015 max	0.015 max	17.0-21.0	1.0 max	50.0-55.0
Element	**Mo**	**Nb**	**Ti**	**Al**	**B**	**Fe**	**Cu**	
Composition Percent	2.80-3.30	4.75-5.50	0.65-1.15	0.20-0.80	0.006 max	Balance	0.30 max	

Table 2.2. Mechanical Property Requirements[14]

Alloy	Ultimate Tensile Strength (MPa)	Yield Strength (MPa)	Elongation (%)	Reduction of Area (%)	Brinell Hardness
NO7718	1275	1034	6	8	331

Table 2.3. Heat Treatment Standards[14]

Alloy	NO7718
Recommended Solution Treatment	924 to 1010°C, hold 1/2 hr, cool at a rate equivalent to air cool or faster
Precipitation Hardening Treatment	718 +- 14 °C hold at temperature 8 hr, furnace cool to 621 +- 14°C, hold until total precipitation time reaches 18 hr, air cool

2.2.2 IN718 Microstructure

Materials generally fall into two different categories, amorphous materials and crystalline materials. Amorphous materials do not display a repeated ordered structure and their atoms are randomly scattered throughout the material's volume. Amorphous materials are typically represented by glasses, some polymers, and in some extreme cases metals can be cooled rapidly enough to form these dis-ordered structures. Crystalline materials display varying degrees of ordered structure. At the high end of ordered structure are materials which are formed of a single crystal lattice and less ordered materials may display several different crystal structures throughout the bulk of the material. Metals and ceramics are the dominant type of materials in this category. Under normal conditions, metals will solidify into ordered crystal structures. Ceramic materials will also form crystalline structures and are often vastly more complex than metal structures because of the varying sizes of the constituent atoms. Some polymers that display ordered structures are classified as crystalline as well but this definition refers to the ordering of molecular chains rather than ordered atomic structure. The majority of metallic materials form either Face-Centered Cubic (FCC), Body-Centered Cubic (BCC), or Hexagonal Close-Packed (HCP) repeating crystal structures as shown in Figure 2.1. These structures differ in the density of their atomic packing and in strong and weak directions. Metals are often considered isotropic materials because of the distribution of microstructural grains of these crystal structures in different orientations[1]. Exceptions to this are carefully processed parts such as single crystal turbine blades or parts manufactured by AM which often exhibit columnar grains in the build direction[28].

As a primarily nickel based alloy, IN718 retains the FCC crystal structure of pure nickel. As shown in the phase diagram in Figure 2.2, IN718 with Nb content between 4.75-5.50 % the γ phase and the laves phase are expected to form[29]. These are the primary phases seen in the micro-structure of wrought IN718 prior to aging. The laves phase is not often seen in IN718 as it requires higher concentrations of Nb than are present in IN718. Growth of this phase has been observed during casting where the local concentration of Nb is higher than in the bulk. The formation of this phase is detrimental to the growth of γ" as it reduces the availability of Nb for precipitate formation. The laves phase typically forms a HCP structure of Fe_2Nb, Fe_2Ti, or Fe_2Mo. Critical to the strength of this alloy is the growth γ" precipitates composed of Ni_3Nb. These precipitates have disk shaped Body-Centered Tetragonal (BCT) geometries and remain coherent with the primary γ lattice. Typically they will replace Ni or Fe atoms within the lattice and induce residual strain which provides a desired strengthening mechanism. A secondary strengthening mechanism is produced

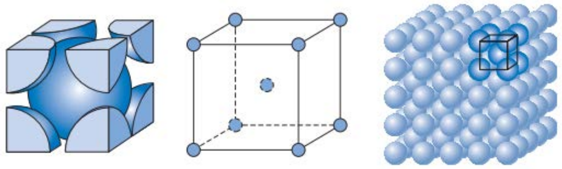

(a) Body Centered Cubic

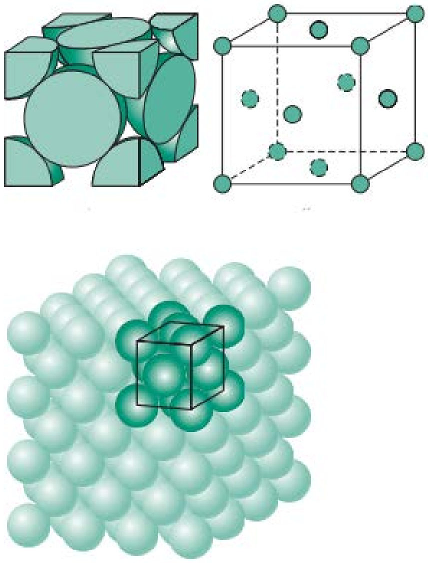

(b) Face Centered Cubic

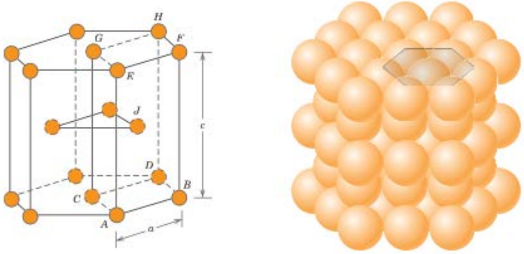

(c) Hexagonal Close Packed

Figure 2.1. Most Common Crystal Structures in Metals[1]

by the growth of γ' precipitates. Composed of Ni_3Al and Ni_3Ti these precipitates were the primary method of strengthening prior generations of Inconel alloys. Also coherent with the primary γ matrix they provide strengthening by inducing lattice strain in a similar fashion to the γ” precipitates. The increased Nb content of IN718 preferentially forms the γ” precipitates in a 3 to 1 ratio over γ'[29]. IN718 that is formed directly by AM processes does not posses these strengthening precipitates. Post-production aging at 718°C is required to grow γ" and γ' precipitates. This is usually accomplished with a solution anneal above 924°C followed by aging at 718°C but can also be accomplished by a direct aging process[14][30]. Additional phases that may be present in a solutionized and aged IN718 part include carbides of TiC and NbC. These carbides take up a very small portion of the volume of the material and have little effect on the mechanical properties of the material. A final phase that will form in IN718 is the orthorhombic, δ, phase. This phase possesses the same chemical stoichiometry as the γ" precipitates but does not provide the same strengthening effect. δ phase preferentially forms at grain boundaries which prevents sliding and corresponds to an increase in tensile strength. This however induces a degree of brittleness to the material that is undesirable. Additionally similar to the effect of the laves phase δ reduces the amount of Nb available to form γ". These two phases are referred to as allotropes. This means that they have the same chemical compositions but different crystal structures. δ is the more stable phase of the two and will form if the material is over aged. Growth of this phase can be avoided by ensuring that the aging treatment does not exceed 750 °C[31]. IN718 is highly dependent on microstructural features to meet desired material properties. Careful control of processing times and temperatures is key to developing a useful product.

The microstructure of IN718 manufactured by AM differs significantly from traditionally produced wrought material. One difference is the directionality of AM microstructure. Wrought material will produce relatively uniform grains of American Society for Testing and Materials (ASTM) grain size of 5 (63.5 μm) after solutionizing and aging[29]. This produces isotropic material behavior with grains oriented with no particular direction. AM material produces columnar grains in the build direction with very fine diameters generally ASTM 11 (7.9 μm)[29]. This results in

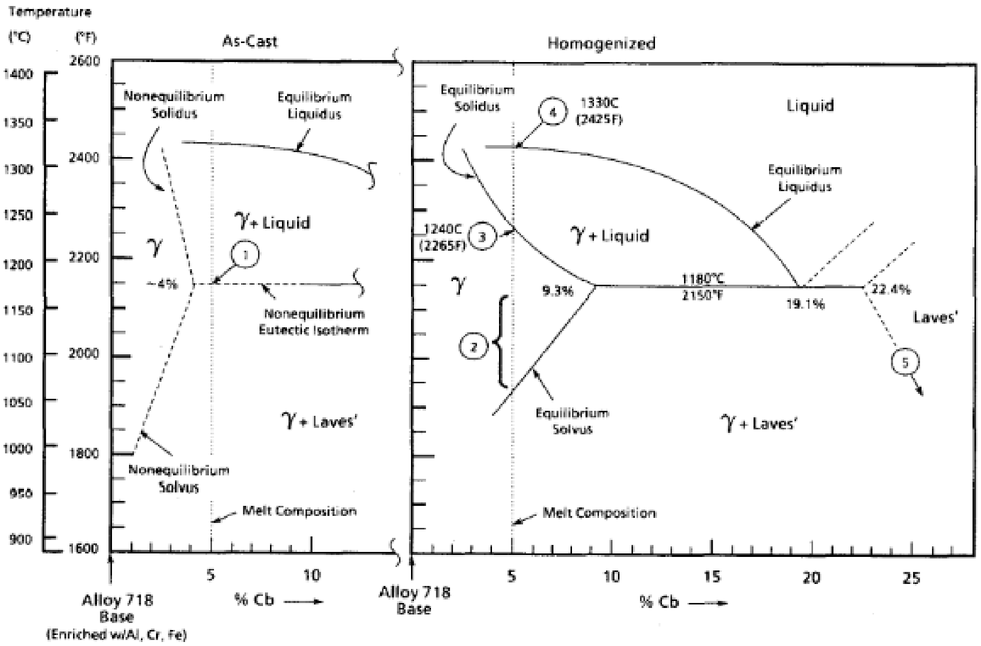

Figure 2.2. IN718 Phase Diagram [2]

anisotropic material behavior which varies widely parallel and perpendicular to the build direction. The specific details of AM microstructure are highly dependent on build parameters such as laser power, scan pattern, and layer height.

2.3 Heat Treatment

2.3.1 Annealing

The first step in many heat treatment processes is referred to as annealing. This process involves raising a material above its re-crystallization temperature, holding for a period of time, and cooling to room temperature[1]. One effect of this process is that any induced stress in the material is relieved. Dislocation motion at these elevated temperatures is rapid and sufficient energy is present in the atomic matrix for atoms to realign and correct flaws in the crystal structure. These stress relief anneals are usually be conducted at lower temperatures to avoid changing a desired microstructure within a part. In the case of stress relaxation the ductility of the material increases but the yield strength and ultimate tensile strength both decrease[4]. In some cases the change of microstructure is the desired effect of the annealing process. In the case of wrought IN718 the purpose of the annealing process is to allow for even distribution of the various alloying elements, especially Nb, throughout the material. This process is usually conducted at 1010°C for 1 hour for wrought IN718[14]. At this temperature the material is above the solvus temperature for the various secondary phases found in IN718 including, the laves, δ phase, γ', and γ" phases. This allows these phases to dissolve and their constituent elements to disperse evenly in the γ phase matrix. After this process the material is cooled to room temperature and is ready for the two stage aging process to form the desired γ" phase. In LPBF IN718 the re-crystallization phase is particularly important. The Modified Heat Treatment (MHT) used in this research utilizes a higher annealing temperature of 1160°C for 4 hours and is described in detail in 2.3. In addition to producing a dispersed field of alloying elements the MHT focuses on increasing the overall grain size of the material. By increasing the grain size the columnar nature common to LPBF materials can be reduced and with it a corresponding reduction in anisotropic material behavior[4]. Grain growth requires longer annealing times as it only occurs after recovery and re-crystallization are complete and no other path for reduction of energy is present. The effects of annealing are critical to promoting the desired mechanical properties in IN718.

2.3.2 Precipitation Hardening

Material strengthening by precipitation hardening is a common process to increase the performance capabilities of many metal alloys. Iron, aluminum, and nickel based alloys are commonly subjected to this procedure. Precipitation hardening is the process of growing second phase particles within the primary material phase to prevent dislocation glide, this process is also known as age hardening. One of the most common precipitation hardened materials is the family of Al-Cu alloys which can see a 400-500% increase in yield strength after growth of precipitates[32]. IN718 is a precipitation hardened material in the nickel family of alloys. Precipitation hardening is accomplished by a two step heat treatment process. This process is described in detail for IN718 in Table 2.3[14]. First, the material is heated up to a temperature where the solid solubility of the alloying components is much higher than at room temperature. This is referred to as a solution anneal and it increases diffusion rates enough to disperse alloying elements evenly in the matrix. The material is then quenched or rapidly cooled to trap the alloying elements in the matrix while keeping the concentration constant throughout the material volume. The rapid cooling results in tiny precipitate formation but no appreciable material strengthening. The material is then reheated to a temperature below the solvus temperature of the second phase but high enough to speed the kinetics of the precipitation process. This is referred to as the aging process. The increased temperature allows for alloying elements to diffuse through the material lattice and group together to form second phase precipitates. This process may take hours or days depending on the specific alloy in question and the desired final precipitate size. Certain aluminum alloys will age at room temperature over the course of several weeks and must be kept cold until ready for final application[1]. In an over-aging condition, precipitates are kept too long at the elevated temperature and material strength begins to decrease as precipitates grow beyond their critical strengthening dimensions. In IN718 over aging will result in the formation of undesirable δ precipitates which form preferentially on the grain boundaries resulting in a loss of ductility. Additionally δ precipitates consume Nb leaving less for the formation of the desirable γ" precipitates[33]. Over-aging can result as a consequence of operating a material at high temperatures and as a result many precipitation hardened alloys have operating temperature limits above which significant loss of strength would be observed. Precipitation hardening is the key strengthening aspect in IN718 alloy.

2.4 Additive Manufacturing

Traditionally manufacturing of components has been by removing material to reach the final product dimensions or by combining many sub-parts to create a final component. AM by contrast creates a component by adding layers of material on top of each other and fusing them together. This process allows for the creation of unique structures not previously possible and the reduction of material loss. This process is often automated and can reduce manufacturing costs as well. Modern AM procedures operate with a Computer-Aided Design (CAD) drawing that software slices into thin layers that are then produced one at a time. The first examples of modern AM were created in 1992 by 3D Systems[34]. These early printers pioneered a process known as fused filament fabrication in which a solid coil of polymer is heated and extruded through a nozzle. This filament is then applied selectively to a build plate as directed by the CAD model as the print head moves in two dimensions. After one layer is produced, either the print head rises by one layer thickness or the build plate drops by one layer thickness and then the second layer is produced. The field of AM took another step forward into the field of metal AM structures. Rather than extruding a filament through a nozzle, metal AM systems use high powered lasers to melt metallic powder together. Two common metal AM procedures are LPBF and Direct Laser Deposition (DLD). In DLD, a nozzle sprays metal power in the desired part location and a laser is timed to melt it at the precise location the solid portion is desired. LPBF lays a pre-set depth of powder across the entire build plate, usually in thicknesses between 20-150 μm[10]. The laser then rasters across the surface melting the desired pattern. Once finished, the build plate drops by one layer thickness and another layer of powder is laid down and the process repeats itself. A diagram of this process is shown in Figure 2.3 After the build is completed, the un-melted powder can be removed and sorted for reuse. These unique characteristics allow AM processes to introduce efficiency improvements in many manufacturing fields.

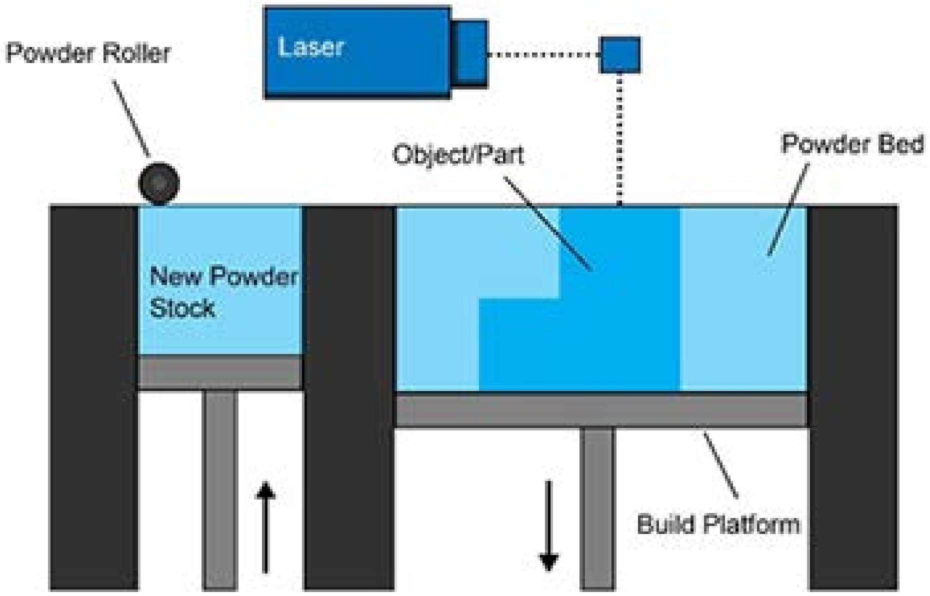

Figure 2.3. Laser Powder Bed Fusion Process[3]

2.4.1 Surface Finish

The surface finish of AM parts is fairly coarse as a result of the laser melting process. Studies of the surface roughness of AM parts indicated that a part generated by LPBF result in surface roughness values of, R_a = 6.7 - 42 μm, depending relation of the measured surface to the build direction[35]. Parts made by conventional processes with milled surface finishes display values between R_a = 0.8 - 6.3 μm[36].

This increase in roughness can cause serious problems in certain applications. For example, the design of curved fuel flow nozzles for rocket and turbine engines is a unique capability presented by AM but roughness in these nozzles can cause undesirable flow characteristics, especially at supersonic speeds. Surface finish is also a key determining feature when predicting fatigue resistance. A study of LPBF IN718 conducted by NASA concluded that parts in the As-Built (AB) configuration required an approximately 30% decrease in the applied stress to attain the same fatigue life as AM parts subjected to a low stress grinding procedure in post-production[37]. As a result of this undesirable surface finish LPBF materials may require some degree of post processing before use.

2.4.2 AM Microstructure

The microstructure of AM parts differs from traditionally produced wrought material. The microstructure of wrought material is described in Section 2.2.2. Due to the layer-by-layer construction of AM and the small regions of melting, a columnar microstructure forms in the direction of melting when viewed parallel to build direction as seen in Figure 2.4a. A comparison image of wrought IN718 can be seen in Figure 2.4b. The small laser spot size and corresponding melt region form a very fine grained microstructure when viewed in the build direction. This effect leads to anisotropy in the material properties and potential part design difficulties.

2.4.3 Residual Stress

One complication of AM is the retention of thermal stresses in finished parts. This is referred to as residual stress and can result in undesirable and unpredictable material behavior under stress. Residual stress is not a unique phenomena with AM material but is often present in conventionally produced material. However, this is

(a) LPFB IN718 microstructure viewed perpendicular the build direction

(b) Wrought IN718 microstructure

Figure 2.4. LPFB and Wrought IN718 Microstructures[4] Images by G. Cobb

not always a negative material condition. Tempered glass is a common utilization of residual stresses. Compressive residual stress at the surface of glass can cause crack closure and restrict potentially critical length cracks from propagating. In the example of smart phone screens, large dopant atoms are added to the surface of the glass to place compressive stresses on the lattice[38]. In glass cookware, residual stresses are imposed by quickly cooling the outer layer of glass while allowing the interior to contract while cooling slowly thus inducing a tensile stress on the interior and a compressive stress on the exterior[39]. In AM parts, residual stresses are a consequence of the same process as the glass cookware where uneven cooling rates leave some areas of material in tensile stress and some areas in compression. However, unlike the previous example residual stresses in AM materials are not currently able to be carefully controlled and can result in cracking of certain part geometries.

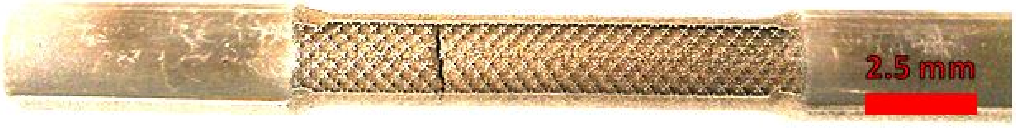

Figure 2.5. Cracking From Residual Stresses

Residual stress in LPBF material is the result of many different variables including layer height, build orientation, part geometry, and build time[40]. An example of this is shown in Figure 2.5. This tensile bar was built horizontally, but warped and cracked as a result of the residual stresses. Bars of the same configuration built in the vertical and 45°orientations did not experience the same failure. Removal of residual stresses is possible with appropriate heat treatment strategies. In wrought IN718, stress relief is accomplished through the standard heat treatment profile detailed in ASTM B637. The first step of the heat treatment raises the temperature to 1010 °C. This process has not proved to be effective in LPBF IN718 and the MHT studied in this research raises the annealing temperature to 1160°C in an effort to remove these stresses. At elevated temperatures the yield strength of IN718 will decreased below the magnitude of the residual stress allowing the stress to relieve. Following this, the parts can then be aged to grow the desired γ" precipitates. Reduction of residual stresses in AM materials is key to attaining the maximum material performance.

2.5 Fracture Mechanics

Fracture mechanics is the study of a growing crack in a material with the goal of quantifying how crack size and shape, loading conditions, and material properties affect the growth of the crack and under what conditions structural failure will occur[41]. The study of fracture mechanics is critical to the design of structures to ensure operational performance and predicted lifetimes. This field works on the premise that all structures have existing flaws that may eventually lead to material failure. The effective application of fracture mechanics can predict rates of crack extension, part lifetime, and safe life replacement schedules.

2.5.1 Linear Elastic Fracture Mechanics

The field of Linear Elastic Fracture Mechanics (LEFM) was first pioneered by Alan Griffith in the early 1900's. After observing that the theoretical tensile strength of glass fibers was 100 times greater than experimental values, he developed a theory that small flaws present in the material reduced the materials strength to the levels observed in experiment. After testing this theory, he developed a relation between flaw size and fracture strength as exhibited in Equation 2.1. This relationship established the term, C, which Griffith would express in terms of surface energy created by crack extension. Griffith's expression for "C" in terms of surface energy is shown in Equation 2.2[42]. These expressions hold very well for materials that display little to no plasticity.

$$C = \sigma_f \sqrt{a} \tag{2.1}$$

$$C = \sqrt{\frac{2E\gamma}{\pi}} \tag{2.2}$$

The next significant addition to the study of LEFM was conducted by G.R Irwin in 1957[43]. He realized that for ductile materials, Griffith's theory did not accurately predict the surface energy created by new crack surfaces in materials displaying plasticity. This is due to the growth of a plastic zone around the crack tip before the crack propagates further. Irwin and his team and the Naval Research Laboratory devised a way to quantify a materials resistance to fracture in the presence of a crack. They called this term the stress intensity factor and labeled it "K". The expression for "K" is given in Equation 2.3. Stress intensity is measured in three modes of stress as seen in Figure 2.6[10]. The stress intensity factor for a known flaw can be determined by the radius of the crack tip. In the case of a nearly infinitely sharp crack tip, the maximum stress intensity factor can be labeled as K_{IC}, K_{IIC}, or K_{IIIC} corresponding to the mode of loading, for plane strain conditions. LEFM provides useful capability to predict crack growth behavior leading to catastrophic failure in brittle materials.

$$K = \sigma_f Y \sqrt{(\pi a)} \quad (2.3)$$

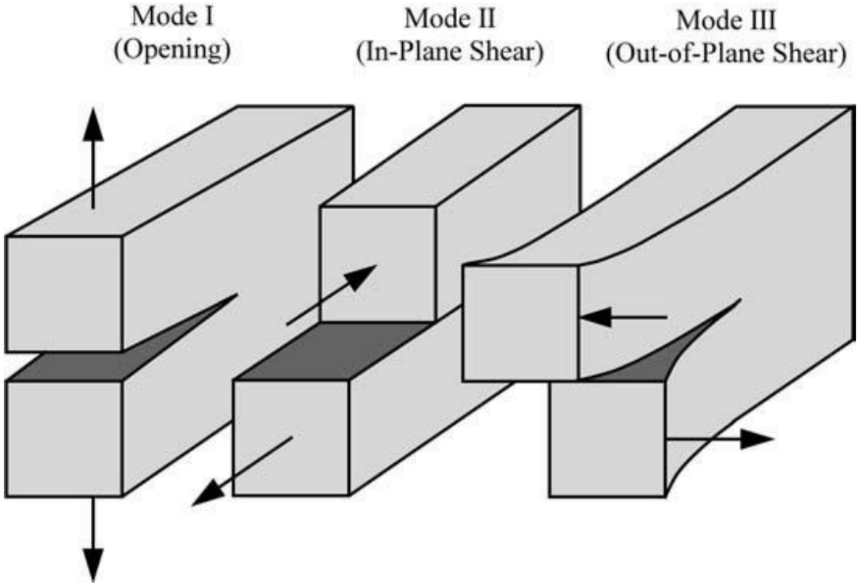

Figure 2.6. Modes of Fracture [5]

2.5.2 Elastic Plastic Fracture Mechanics

While LEFM is a useful tool for examining fracture mechanics it can no longer be reliably applied when material plasticity extends beyond the crack tip region. In these instances examination of material behavior must rely on the field of elastic plastic fracture mechanics. Several methods of measuring the fracture toughness for elastic plastic materials were developed including crack tip opening displacement, crack extension resistance curves, and J-integrals. The J-integral method of measurement is by far the most common. This method was developed by James Rice in 1968. The J-integral treats elastic plastic materials as non-linear elastic to extend the capability of LEFM[44]. Elastic plastic materials behave in much the same way as non-linear elastic materials. This behavior is shown in Figure 2.7. Both non-linear elastic and elastic plastic materials follow the same loading curve but differ at unloading. Non-linear elastic materials will relax along the path of loading back to their original undeformed unstressed state. Elastic plastic materials in contrast do not unload along the same non-linear path but rather unload in a linear manner where the slope of the unloading line is equal to the elastic modulus[5]. This process leaves permanent deformation in the material due to dislocation motion and affects future material response. Rice's J-integral theory relies on treating elastic plastic materials as non-linear elastic and this assumption holds as long as no unloading occurs. His characterization of the J-integral as a path independent line integral relies on similar principles to Griffith's strain energy release rate but for non-linear elastic materials[44]. It is still defined as the change in potential energy with the change in crack area and is described in Equation 2.4. This allowed Rice to construct a path independent integral around a growing crack tip and using the applied stresses and strains, to equate this integral to the energy release rate[5]. Further work conducted in tandem by Hutchinson, Rosengren, and Rice determined that the stresses and strains near a crack tip could be represented by a power law that included the calculation of J. These relations are show in Equations 2.5 and 2.6[19][45]. The value of the J-integral can be measured by manipulations on a trace of force and crack extension for a specimen with known dimensions. This process is described in 3.5. Elastic Plastic Fracture Mechanics (EPFM) greatly expands the applicability of fracture mechanics and allows material behavior prediction in high toughness engineering materials.

$$J = \frac{d\Pi}{dA} \tag{2.4}$$

$$\sigma_{ij} = k_1 (\frac{J}{r})^{\frac{1}{n+1}} \tag{2.5}$$

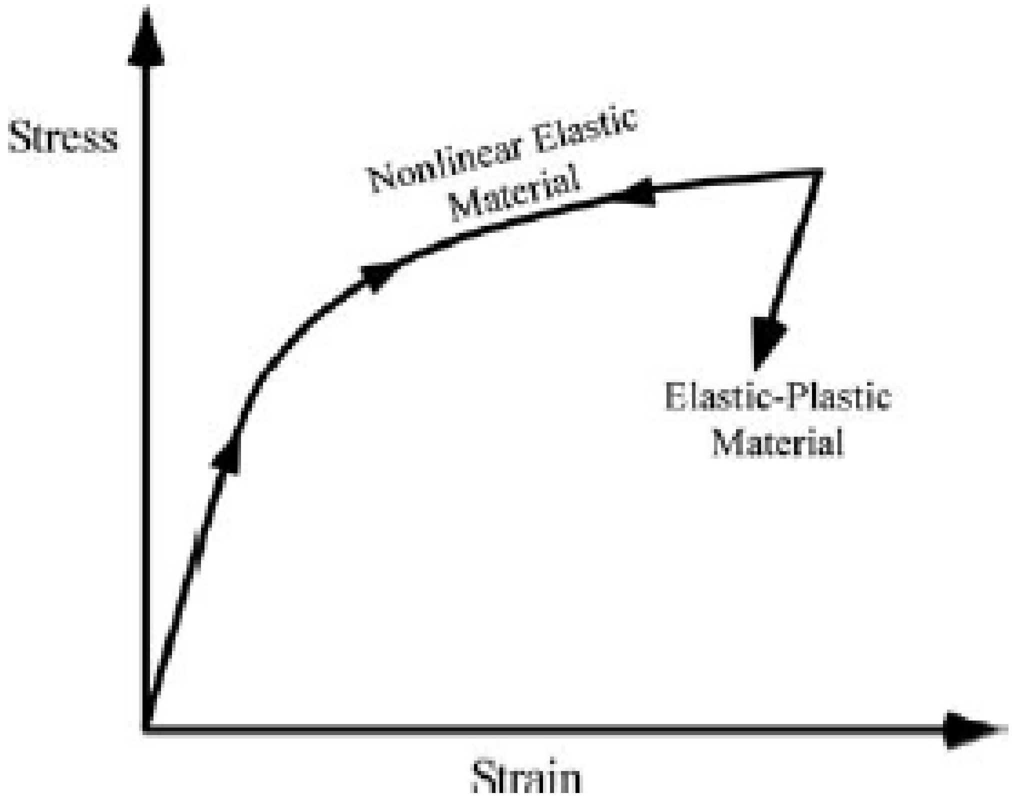

Figure 2.7. Schematic comparison of the stress-strain behavior of elastic-plastic and non-linear elastic materials[5].

$$\varepsilon_{ij} = k_2(\frac{J}{r})^{\frac{n}{n+1}} \tag{2.6}$$

2.5.3 Fracture Toughness

Fracture Toughness (FT) is a parameter that can be used to determine a materials ability to resist failure by taking into account "material, temperature, strain rate, environment, and thickness"[6]. FT is closely related to the stress intensity factor. An analogous comparison for these two terms would be strength and stress. Stress represents the current material loading conditions quantifying the applied force and the area the force is applied over and strength, yield or ultimate, represents the maximum stress a material can withstand before permanent deformation or failure. In a similar way stress intensity factor represents the concentrated stress at a crack tip and fracture toughness represents the maximum stress concentration a material can withstand before crack propagation[46]. In LEFM plane strain FT is quantified by the term K_{IC} for mode 1 failure and is usually reported in units of $MPa\sqrt{m}$ and is referred to as the plane strain fracture toughness. This mirrors the stress intensity factor equation with the replacement of crack length, a, with the critical crack length, "a_c", this is shown in Equation 2.7. This value decreases to an asymptotic limit as thickness increases to a minimum value known as K_{IC} which is the design independent value of fracture toughness for a given material for mode one fracture. This thickness is determined to be valid when the condition in Equation 2.8 is met. For EPFM FT is quantified by J_{IC}. This term is similar to K_{IC} in that it marks the point of fracture instability in a material. J_{IC} is reported in terms of energy per area usually in $\frac{kJ}{m^2}$. It is measured from a J vs crack extension curve and is calculated in a similar manner to the 0.2% offset stress that characterizes a materials yield strength. For J_{IC} this offset is measured by constructing a line parallel with the linear section of the J curve that intersects the x-axis at 0.2mm and calculating the intersection of the construction line and the J curve. A standard J vs crack extension curve is shown in Figure 2.8. Once a value for J_{IC} has been determined it can then be used to calculate K_{JIC} with the expression in Equation 2.9[11]. This quantity is representative of the plain strain fracture toughness for elastic plastic materials. The study of fracture toughness is a key component to understanding material capability and the ability of structures to continue to function after sustaining damage.

$$K_{IC} = \sigma_f Y \sqrt{(\pi a_c)} \tag{2.7}$$

$$B \geq 2.5(\frac{K_{IC}}{\sigma_y}) \tag{2.8}$$

$$K_{JIC} = \sqrt{(E/(1-v^2) * J_{IC})} \tag{2.9}$$

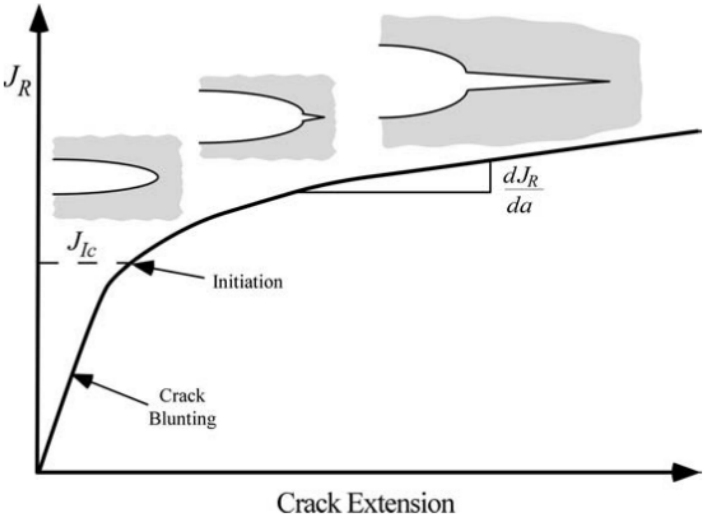

Figure 2.8. Standard J vs Crack Extension Curve for a Plastic Material[5]

2.5.4 Fatigue Crack Growth

When materials undergo repeated loading below their yield limit, they become susceptible to a form of material damage known as fatigue. It is estimated that fatigue is the cause of approximately 90% of failures of metallic components[1]. Because failure can occur well below the static stress limits of parts, simply designing parts with a large factor of safety does not guarantee that fatigue will not eventually lead to a failure. Fatigue Crack Growth Rate (FCGR) testing can provide a geometry independent method of characterizing a materials resistance to failure by fatigue. A typical FCGR curve is shown in Figure 2.9. This curve is composed of three regions and displays the effect of changing stress intensity factor resulting from crack growth on the amount of crack extension per cycle. The first region of this plot shows the initiation behavior of the fatigue crack and characterizes a value called $K_{Threshold}$ below which existing cracks in the material will not propagate. The second region is typically linear and is known as the Paris region. In 1961, Paul C. Paris published a paper titled “A Rational Theory of Fatigue” in which he proposed a power law relationship between the crack extension per cycle and the stress intensity factor as seen in Equation 2.10[24]. Because of the predictable nature of crack growth in this region, parts with known or suspected crack sizes can be given a predicted lifetime of use before needing to be removed from service or replaced. Region three involves rapid crack growth and unstable behavior before fracture. Fracture critical parts require damage tolerance evaluations to ensure safe operation. Characterizing FCGR in region 2 can give designers a predictable model to predict part lifetimes and requirements for retirement or replacements prior to catastrophic failure. Fatigue loading is a key cause of structural failure and is a critical area of study for new materials and processes.

$$\frac{da}{dN} = A(\Delta K)^n \tag{2.10}$$

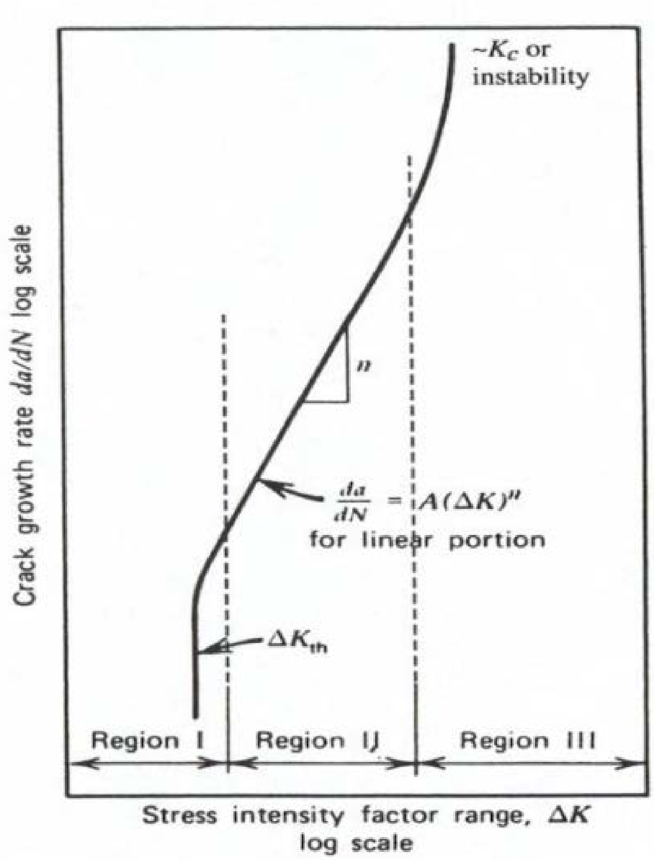

Figure 2.9. Regions of Fatigue[6]

2.6 Micro-Structural Effects on Material Properties

A significant driving factor in the material properties of metals is the microstructure. As discussed in section 2.3.2 formation of precipitates can significantly improve the mechanical strength of certain metals. Grain size is a relatively easy microstructural feature to control and increases and decreases in grain size can positively or negatively affect the material behavior under different stress conditions. For example, tensile strength is commonly seen to rise in IN718 as grain size decreases[47] whereas creep strength sees marked increase as grain size increases[48]. These conflicting responses often result in design to function solutions based on the most likely mode of failure of an end use part. An example of this disparity would be the construction of jet turbine blades as single crystals to improve the creep strength while sacrificing tensile strength. Beyond mechanical properties, electrical and thermal properties are also highly dependent on the effects of micro-structure. As a result of the heat treatments selected for this research there will be broad differences in the microstructure of the different test conditions.

2.6.1 Effects on Fracture Toughness

Yield strength is typically seen to increase with decreasing grain size. Fracture toughness responds to changes in grain size with the opposite effect. Larger grained materials show increasing values of FT[49]. This corresponds to a decrease in yield strength and an increase in ductility. Toughness can be seen as the area under the curve of a standard stress vs. strain plot during a tensile test. As seen in Figure 2.10, an increase in modulus often corresponds to a decrease in ductility and a corresponding decrease in toughness. Grain size is not the only microstructural feature that affects FT. In IN718, the growth of precipitate phases is a key driving factor in most mechanical properties, FT is no exception. In a study by W.J.Mills FT in IN718 was seen to decrease as the growth of δ particles increased. In contrast, as the fraction of γ" precipitates increases the fracture toughness of the material increases[50]. This same study also indicated that increasing amounts of the laves phase lead to a decrease in the overall FT. Degradation of fracture toughness can also be caused by excessive carbide formation, especially along grain boundaries. The effect microstructural changes on fracture toughness will be examined as a product of this research.

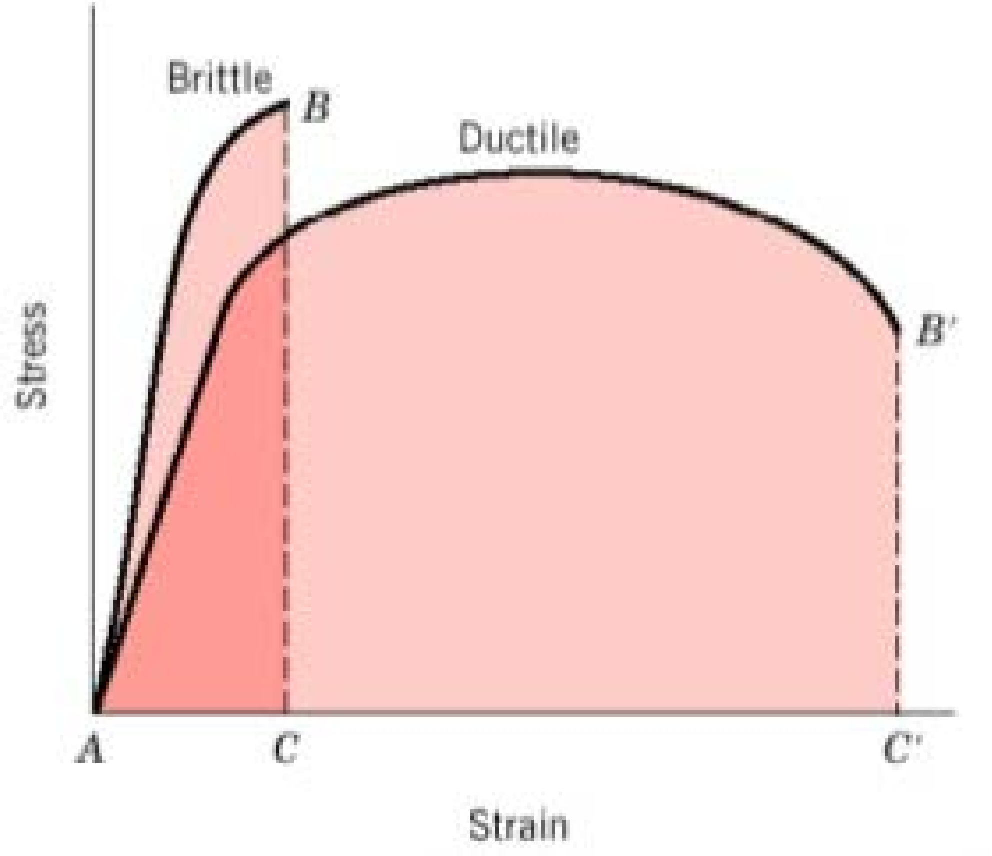

Figure 2.10. Toughness Related to the Stress Strain Curve[7]

2.6.2 Effects on Fatigue Crack Growth

Studies on IN718 have shown that that both grain size and γ" precipitate size have noticeable effects on FCGR in IN718[51]. This research studied four different microstructural conditions. Coarse and fine grained microstructures were produced with either small or large γ" precipitates. For small precipitates increasing the grain size increased the value of $K_{Threshold}$ but also increased the FCGR. Large precipitates saw no change in the FCGR as grain size increased but $K_{Threshold}$ was lower for fine grained microstructures. Coarse grained microstructures showed a lower FCGR for both sizes of precipitates. However, coarse grained microstructure with large γ" precipitates showed a lower value of $K_{Threshold}$ than for small precipitates[51]. These results will factor strongly into the result of this research. AB specimens will possess a small grain size and minimal amounts of γ" precipitates. Conventional Heat Treatment (CHT) specimens will possess a small grain size as well but will posses the γ" precipitates. MHT specimens will possess larger grains and the γ" precipitates. If the above conclusions reached by Krueger hold consistent in AM IN718 the MHT specimens should produce the lowest rates of FCGR. $K_{Threshold}$ should remain fairly consistent between the CHT and MHT specimens as the two heat treatments utilize the same aging parameters. $K_{Threshold}$ for the AB specimens is expected to be lower due to the lack of γ" precipitates. This research will explore the effects of grain size and production of γ" precipitation as a result of the selected heat treatments on fatigue crack growth in the Paris regime.

2.7 Chapter 2 Summary

IN718 is a commonly used alloy in jet turbines, nuclear power production, and other high temperature, highly corrosive environments. Recent developments have made production of this alloy by LPBF feasible for use in these fields. Production by this method results in unique microstructural characteristics and retention of residual stresses. Because IN718 is a precipitation hardened alloy, small changes to its microstructure can have profound effects on its final mechanical properties. No part is completely free of internal cracks or defects. The fracture toughness of a material is a key consideration during design to ensure proper part performance and prevention of premature failure. Fatigue crack growth is a common failure mode for parts in service and can present suddenly and catastrophically. The study of these two failure modes is critical prior to end use of new manufacturing methods and materials. Additionally, research contributions that allow AM parts to meet or exceed their wrought material equivalents in these performance categories would be a significant contribution to this research field. The methodology used to determine both FT and FCGR in AM IN718 will be discussed in detail in Chapter 3.

III. RESEARCH METHODOLOGY

3.1 Chapter 3 Overview

The goal of this research was to identify the directional dependence of Fracture Toughness (FT) and Fatigue Crack Growth Rate (FCGR) of Inconel 718 (IN718) manufactured by Laser Powder Bed Fusion (LPBF). In addition, this work serves to identify whether a modified heat treatment can remove this directional dependence. The primary experimental plan for this work was derived from American Society for Testing and Materials E1820-17a (ASTM E1820-17a) and American Society for Testing and Materials E647-15 (ASTM E647-15). These two standards lay out accepted procedures for testing FT and FCGR specimens. Some deviations from these standards were made to meet the unique needs and characteristics of IN718 for the requirements of this research. The major components of this research include FT testing, FCGR testing, and fracture surface evaluation. Numerous important factors must be accounted for in order for these hypothesis tests to be conducted. This chapter will focus on the development and documentation of the methods that were considered to perform the necessary evaluations of these material characteristics. A key part of the experimental setup was the specimen processing, which includes printing, machining, and polishing. The specific effects of specimen build orientation and heat treatment were examined for each of these components. The following sections detail the experimental methods employed to accomplish this research and to process the data into usable results.

3.2 Materials and Equipment

The material and mechanical properties of the specimens were characterized using a wide variety of equipment available at Air Force Institute of Technology (AFIT).

Mechanical tests performed for this research was conducted on a Material Testing Systems (MTS) 810 hydraulic uniaxial testing machine with a maximum loading capability of 100 kN. This machine possessed upper and lower axial displacement capability. Only the lower axial hydraulic head was utilized for this research. Clevis and pin grips were produced from American Iron and Steel Institute (AISI) 4340 steel which was quenched and tempered to "provide adequate strength and resistance to galling and fatigue"[12]. These grips were constructed to the design specified in Figure A2.2 of American Society for Testing and Materials E399-17 (ASTM E399-17). Crack mouth opening was measured using an MTS Model 632.02F-20 clip gauge as shown in Figure 3.1. This gauge was calibrated prior to testing to ensure a linear response was recorded across the entire range of measurement. Optical crack size measurements were performed using a digital camera with a high resolution lens. These measurements were used as a secondary crack length measurement technique and consequently images were not taken on both sides of the specimen as recommended in ASTM E647-15 and ASTM E1820-17a. The entire experimental setup can be seen in Figure 3.2. To ensure that optical measurements were taken consistently, a fixed camera mount was designed, and affixed to the support pillars of the MTS machine. This process benefited from the rapid prototyping capabilities of a FORTUS polymer 3D printer at AFIT in constructing the grips to hold the camera. Fracture surface investigation was performed using a Keyence VR-3200 3D Measurement Macroscope and a Zeiss Axio Observer.Z1 Laser Scanning Microscope. These techniques allowed the characterization the area roughness average in the fracture region. These investigations were performed on the experimental area of interest and are discussed in detail in Section 3.7.

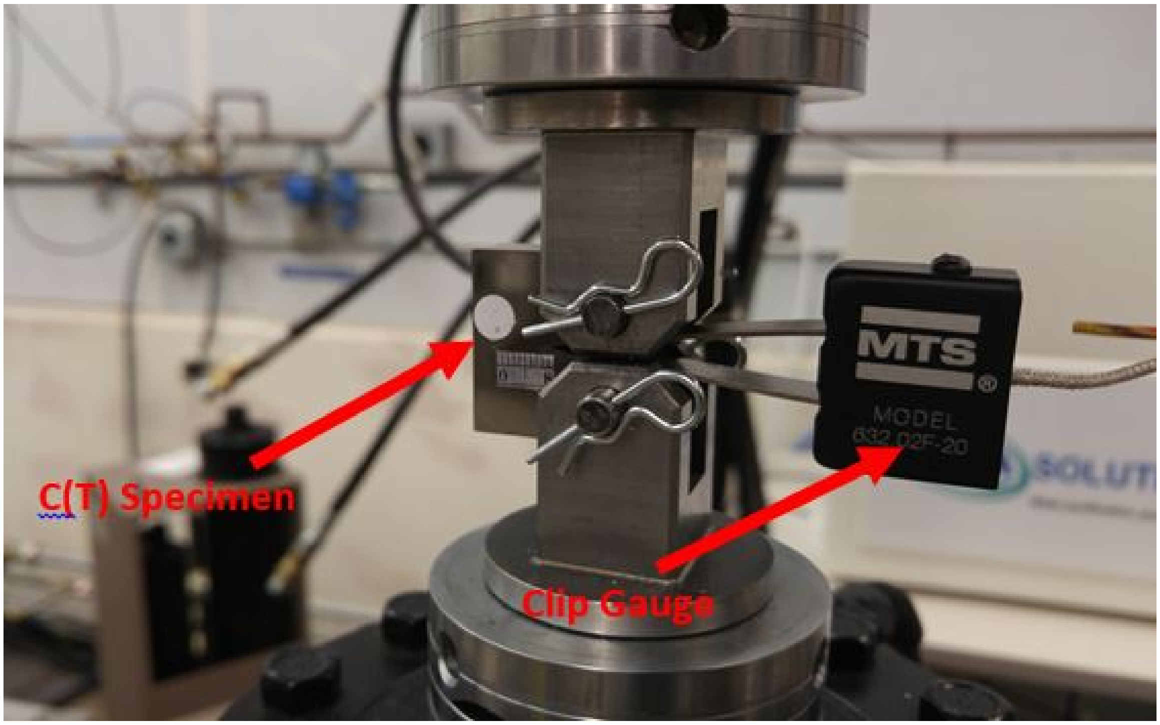

Figure 3.1. MTS Model 632.02F-20 Clip Gauge

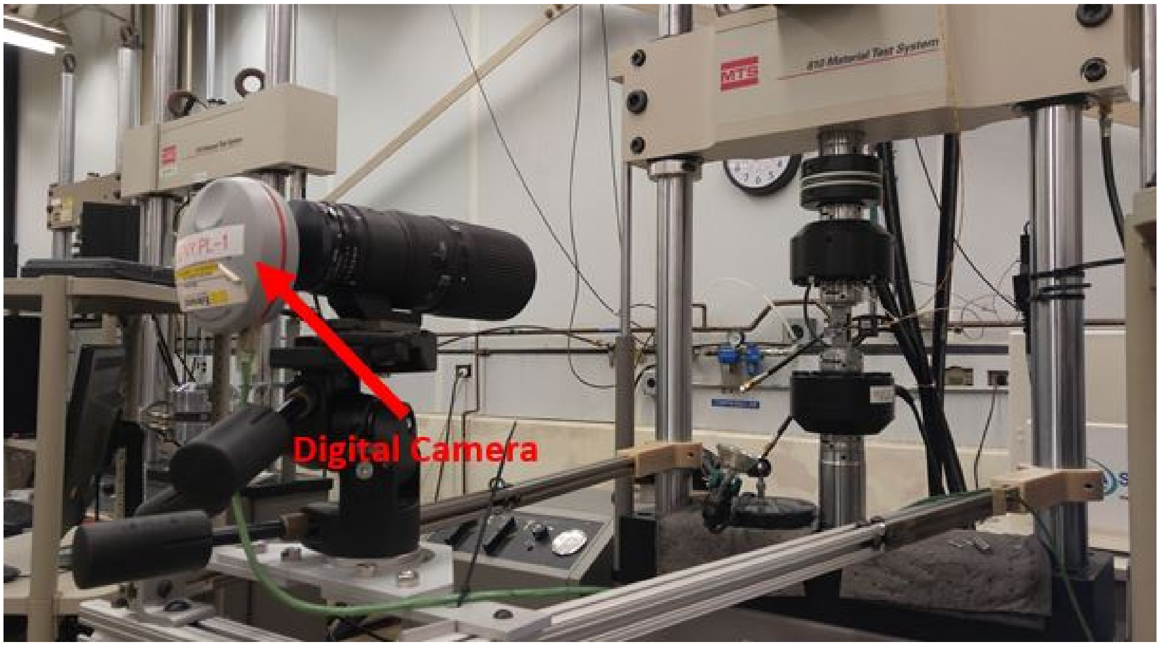

Figure 3.2. MTS 810 Hydraulic Uniaxial Testing Machine with Fixed, High Resolution Digital Camera

3.3 Specimen Fabrication

All Compact Tension (C(T)) specimens were produced using IN718 powder on the M2 Cusing Laser Printer located at the AFIT as seen in Figure 3.4. Fifteen specimens were produced per build plate, with five specimens in each specimen build orientation, (Flat(X), Edge(Y), Vertical(Z) Figure 3.10). Multiple builds were required to produce the necessary number of specimens for testing. Figure 3.3 shows a completed build. Inconel powder was purchased from the Powder Alloy Corporation of Cincinnati, Ohio. The average powder diameter was 40 μm, and chemical composition is provided in Table 3.1. Post processing machining was accomplished by the AFIT model shop, and heat treatments were performed at Winston Heat Treatment Inc in Dayton, Ohio. The processes used to create and prepare specimens provided test specimens meeting the requirements of ASTM E399-17.

3.3.1 M2 Cusing Laser Printer

Several different machines are commercially available for production via LPBF. They offer a range of power capability and build plate sizes. C(T) specimens for this research were manufactured on a M2 Cusing Selective Laser Melter. This 3D printer utilizes LPBF to manufacture parts from a Computer-Aided Design (CAD) model with a high degree of precision. Multiple different settings are possible to optimize printing parameters for individual parts. Powder layer height can be varied between 20 μm and 80 μm. Laser power is programmable up to 400 W. Laser spot size can be as large as 500 μm or as small as 50 μm. The rate the laser moves across the surface is

Table 3.1. Chemical Composition of IN718 Powder, Less than 0.1% C, Mn, Si, S, P, B, Cu, Ca, Mg, O, N

Element	**Mo**	**Nb**	**Ti**	**Al**	**Fe**	**Cr**	**Co**	**Ni**
Composition Percent	2.93	5.32	0.97	0.45	17.69	18.08	0.2	54.05

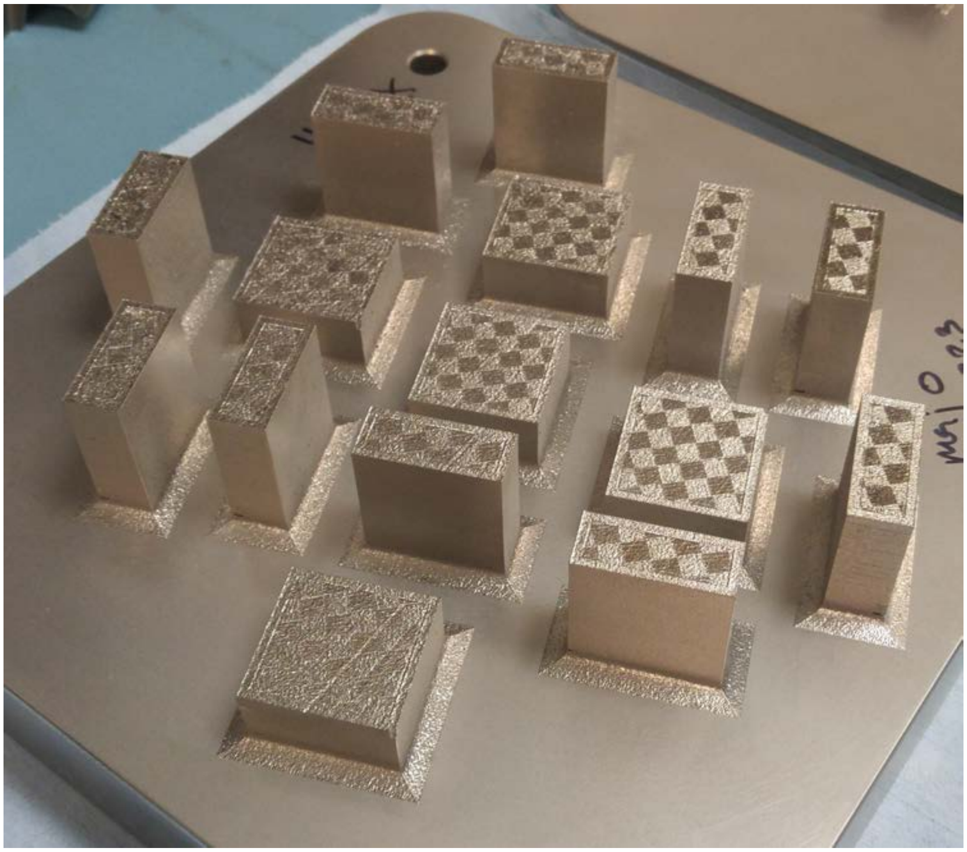

Figure 3.3. CT Specimen Build Plate

referred to as scan speed and ranges from 4 m/s to 7 m/s. These parameters affect the final micro-structure and density of the parts being produced. The C(T) specimens produced in this research were produced using an island scan strategy. This involves three distinct sections of the part surface called: core, skin, and advanced contours. A diagram of the laser path is shown in Figure 3.5. The laser welds small 5x5 mm sections across the center of the design and uses a continuous laser path to trace the outer dimensions of the part. This outer portion is referred to as the skin of the material. The parameters for each section are in Table 3.2. Previous work utilizing these printing parameters produced parts with 0.996% porosity[8]. Specimens were produced 15 at a time, with 5 specimens of each specimen build orientation randomly positioned on the build plate. Ninety total specimens were produced for testing. One

Figure 3.4. M2 Cusing Laser Printer

completed build experienced unexpected amounts of part shrinkage resulting in those parts no longer meeting the dimensional tolerance called for in ASTM E1820-17a. The printer utilized for this research successfully produced 75 C(T) specimens acceptable for testing.

Table 3.2. Printer Parameters for Island Scan Strategy

Section	**Laser Power (W)**	**Layer Height (μm)**	**Spot Size (μm)**	**Scan Speed (mm/s)**
Core	240	40	180	700
Skin	180	40	130	800
Contours	120	40	50	280

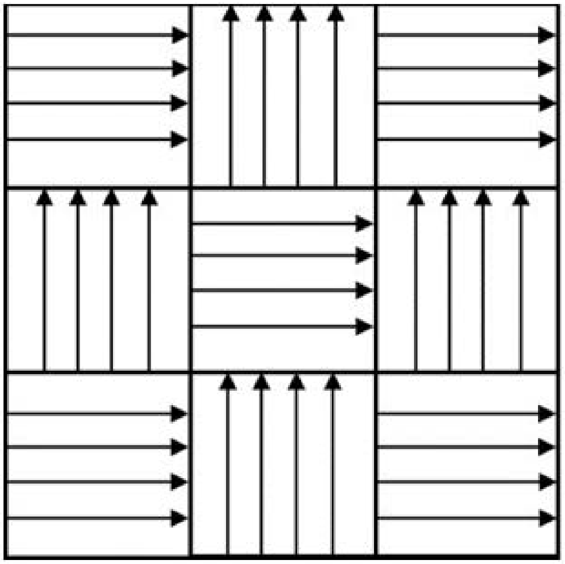

Figure 3.5. Island scan strategy printing pattern, arrows show laser path[8]

3.3.2 Specimen Preparation

Following production by the LPBF process discussed above, the un-processed C(T) specimens required additional steps to meet the dimensional tolerances specified in ASTM E647-15 and ASTM E1820-17a. The first step of post processing was removal from the build plate. This was accomplished via wire Electrical Discharge Machining (EDM). Wire EDM is a cutting process that utilizes a high electrical current passed through a thin wire to produce an electrical arc that removes the desired portion of material . This process is an efficient means of cutting hard materials with high precision without inducing excessive residual stresses to the part[52]. Following removal from the build plate, the next step in the process was to mill the surface to a uniform finish to allow for tight dimensional control to achieve the desired outer specimen dimensions. After the desired dimensions were achieved, two pilot holes were drilled into the specimens to aid in the machining of the pin holes. After drilling, the C(T) specimens take one of two routes. Parts that were tested in the As-Built (AB) condition were directly sent to be processed by wire EDM, while Conventional Heat

Treatment (CHT) and Modified Heat Treatment (MHT) parts underwent a solution anneal followed by an aging process. The specific heat treatment parameters for this project were dictated by ongoing research at AFIT by Maj David Newell[4]. The profile investigated is detailed in Section 3.4. Following this process the heat treated parts were sent to the wire EDM to be cut the required shape and dimensions. After the specimens were cut to final dimensions the final preparation step was polishing. This was accomplished using AFIT's Buehler Automet Eco300 and AFRL's Buehler Automet Eco250 automatic polisher, see Figure 3.6. A series of unique polishing jigs (Figure 3.7) were designed to fit shape of the C(T) specimens and tailored to fit the different dimensions of the two polishers allowing for simultaneous polishing of 5 C(T) specimens at a time. The polishing method used is detailed in Table 3.3. This polishing process produced a mirror-like finish on the C(T) specimens which allowed for accurate optical tracking of crack progression. These procedures allowed specimens meeting the required dimensions and tolerances to be produced reliably for testing.

Figure 3.6. Specimen Polishing Lab at AFIT[4]

Figure 3.7. CT Specimen Polishing Jig

Table 3.3. Polishing Parameters

Step	Surface	Grit Size	Time	Spin Type	Base Speed	Head Speed	Pressure
1	SiC Paper	240	10 min	Complimentary	300 rpm	50 rpm	5 lbs
2	SiC Paper	320	4 min	Complimentary	300 rpm	50 rpm	5 lbs
3	SiC Paper	400	4 min	Complimentary	150 rpm	50 rpm	5 lbs
4	SiC Paper	600	3 min	Complimentary	150 rpm	50 rpm	5 lbs
5	Apex DGG	9	3 min	Counter	150 rpm	50 rpm	4 lbs

3.4 Experimental Heat Treatment

FT and FCGR specimens were tested in the AB condition and after a MHT profile being developed in concurrent research by David Newell[4]. FCGR tests were additionally performed on specimens that had undergone the CHT detailed in American Society for Testing and Materials B637 (ASTM B637). Details of the heat treatment are provided in Table 3.4. The MHT process utilizes a higher annealing temperature than the 1010 °C outlined in ASTM B637. The purpose of annealing at 1160°C for 4 hours vs 1 hour is to encourage the columnar micro-structure to form equiaxed grains and ideally remove the anisotropy produced during the Additive Manufacturing (AM) process[4]. Re-crystallization is accomplished at the higher annealing temperature along with grain growth. The resulting microstructure is equiaxed and anisotropy in the microstructure is removed. The desired effect is that the equiaxed microstructure will produce isotropic material behavior[53]. Figure 3.8 illustrates the effect of the CHT and MHT on the AB microstructure. These different heat treatments provide a broad set of conditions for examination.

Table 3.4. Three Stage Heat Treatment Process for CHT and MHT

Conventional Heat Treatment (CHT)	
Solution Anneal	1010°C for 1 hr, quenched in nitrogen gas
Aging	718°C for 8 hrs, cooled in furnace to 621°C
Aging	621°C for a total aging time of 18 hrs, cooled in air to room temperature
Modified Heat Treatment (MHT)	
Solution Anneal	1160°C for 4 hrs, quenched in nitrogen gas
Aging	718°C for 8 hrs, cooled in furnace to 621°C
Aging	621°C for a total aging time of 18 hrs, cooled in air to room temperature

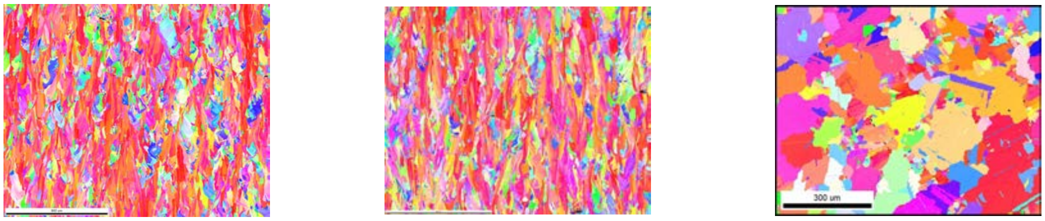

(a) AB Microstructure **(b)** CHT Microstructure **(c)** MHT Microstructure

Figure 3.8. Effect of Heat Treatment[4] Images by G. Cobb

3.5 Fracture Toughness Testing

Initial attempts at FT testing were conducted in accordance with the procedures in ASTM E399-17. This standard details the process to obtain K_{IC} values for plane strain fracture toughness under linear elastic conditions. A total of seven specimens were run through this procedure. All of these specimens were in the AB configuration. Three were Flat(X) builds, two were Edge(Y) builds, and two were Vertical(Z) builds. The data from these tests was analyzed using the methods prescribed in ASTM E399-17. None of these tests passed the validity requirements of ASTM E399-17 section

9.1.3 as shown in Equation 3.1 where P_max is the maximum applied force during the test and P_Q is the force where a secant line with 95% of the slope of the linear region intersects the Force vs Crack Mouth Opening Displacement (CMOD) line. Failing this validity test indicated that the material undergoes too much plastic deformation to be evaluated with Linear Elastic Fracture Mechanics. In this instance FT testing is redirected to ASTM E1820-17a for J Integral testing via Elastic Plastic Fracture Mechanics. ASTM E1820-17a provides the means to account for plastic deformation in the material and produce J_{IC} values for fracture toughness.

$$\frac{P_{max}}{P_Q} \leq 1.10 \tag{3.1}$$

3.5.1 Fracture Toughness Specimen Configuration

Because of the initial experiment design C(T) specimens were designed to meet the requirements of ASTM E399-17 with the straight through starter notch Figure 3.9. Specimen production was completed before initial testing and the discovery of invalid test results. For this reason existing specimens were adopted for use in further testing. For wrought products ASTM E399-17 details a labeling method designed to ensure the effects of rolling direction and crack direction are captured. This two letter labeling system is not used for non-wrought products and in the case of LPBF would produce duplicate results. The labeling convention for the parts produced for this research is shown in Figure 3.10 and is adapted from similar research performed on titanium manufactured by LPBF[10]. Further mathematical adaptations were required to utilize data from these specimens for further testing. This design produced undesirable results due to extensive crack curvature. Side grooving of specimens with a overall reduction in thickness of 0.25B should mitigate this effect in future work.

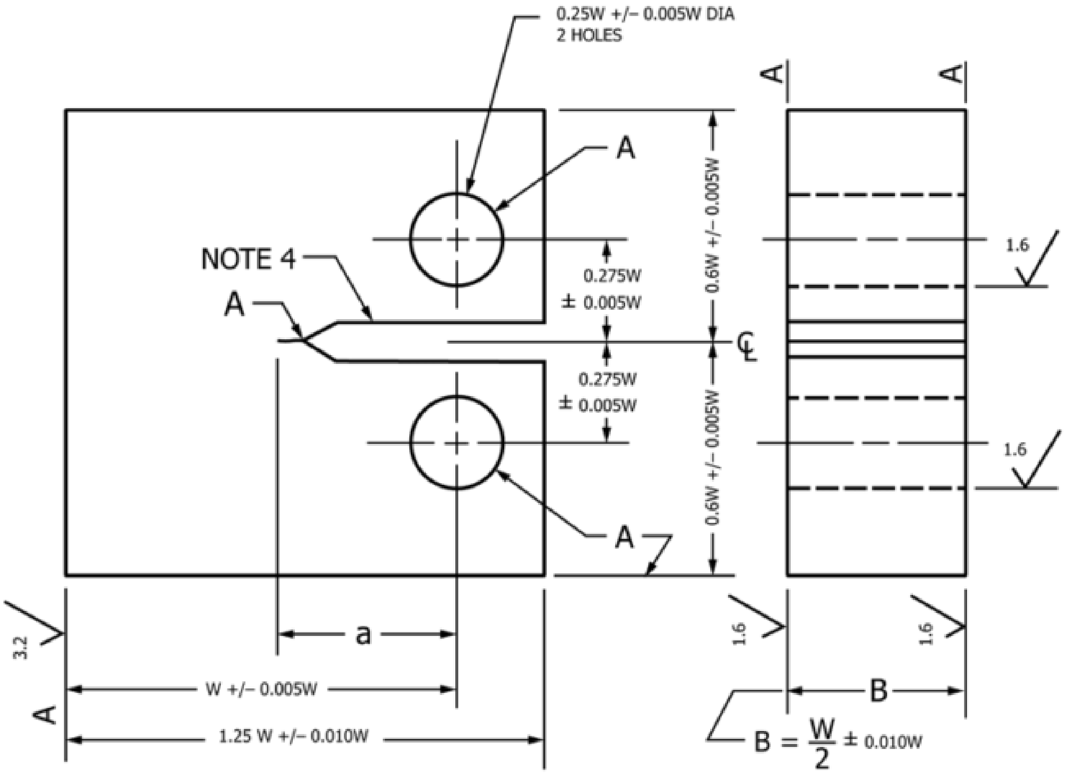

Figure 3.9. CT Specimen Design[9]

3.5.2 Fracture Toughness Precracking

For both FT and FCGR testing a key requirement is that the specimens being tested develop a small fatigue precrack prior to testing. This is because "even the narrowest practical machined notch cannot simulate a natural crack well enough to provide a satisfactory measurement of K_{IC}" or FCGR[9]. This process is dictated in section 7.4.5 of ASTM E1820-17a for FT testing and in section 8.3 of ASTM E647-15 for FCGR testing. ASTM E1820-17a dictates that a fatigue precrack shall be grown such that it "shall not be less than 0.5N where N is the notch height or 0.25 mm"[11]. Specimens used in this research have a nominal value for N of 2.03 mm which results in a calculated precrack length of 1.015 mm. The first seven specimens tested via ASTM E399-17 had fatigue precracks grown to a minimum length of 1.3 mm. To

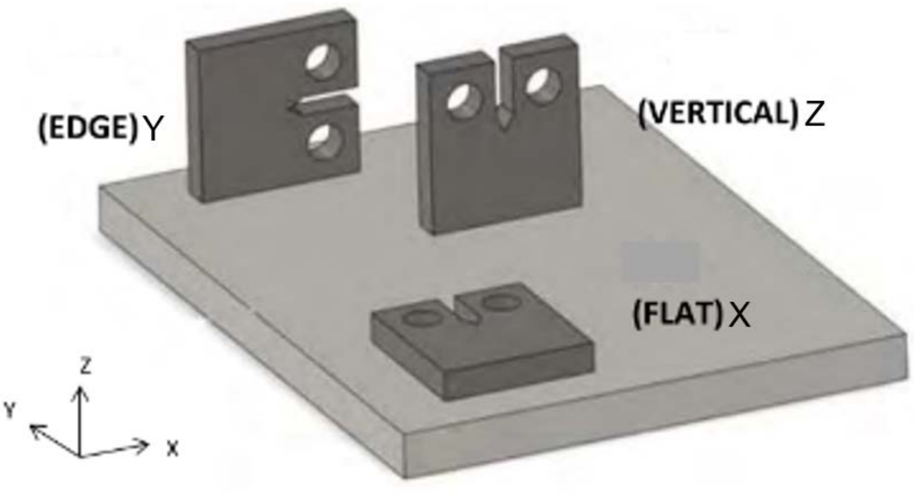

Figure 3.10. Labeling Method for AM Specimens[10]

keep consistency among the tests, specimens tested against ASTM E1820-17a had precracks grown to 1.3 mm or slightly longer. The total length of the machined notch and the precrack for the same nominal specimen size was between 0.45W and 0.7W (11.43 mm - 17.78 mm). Final dimensions for each FT specimen can be found in Table A.1 average measurements for each condition can be found in Table 3.5. Precracking is prescribed in two stages in ASTM E1820-17a. The initial stage is conducted so that the maximum value of the stress intensity factor meet the criteria in Equation 3.2. This criteria applies to the first 50% of the precrack length. The second stage of precracking applies to the final 50% of crack growth and follows Equation 3.3. The lower value at the second stage is to ensure that the stress intensity factor stays below the desired start point of the test. To avoid complication all precracking was conducted at or below 60% of the initial K_{MAX} for this experiment. This precracking process met the requirements of ASTM E1820-17a to create a sharp crack tip to create the desired stress intensity.

$$K_{MAX} = 0.063\sigma_y \tag{3.2}$$

$$K_{MAX} = 0.6K_P \tag{3.3}$$

3.5.3 Fracture Toughness Procedure

Testing was conducted using the basic procedure outlined in ASTM E1820-17a Section 8.4. This procedure requries loading the C(T) specimen in displacement control to a pre-determined maximum displacement followed by fatigue cracking to preserve the fracture surface for later investigation. Optical crack length measurements were taken every 0.5 seconds for the duration of the test. In this research specimens were loaded at a rate of 0.015 mm/s to a maximum displacement of 1.5 mm. Several early specimens were run at different maximum displacements until a satisfactory end point was determined. Crack length measurements and force were then used to calculate the J integral. Crack length was determined by measuring crack mouth opening displacement with a clip gauge extensometer. The initial experiment design included testing FT via ASTM E399-17 and the specimens were designed according to Figure 3.9 from ASTM E399-17. ASTM E1820-17a calls for a slightly different design for the CT specimen as shown in Figure 3.11. The primary difference between these two designs is the location of knife edges for clip gauge

Table 3.5. Fracture Toughness Specimen Dimensions

Specimen	**W (mm)**	**B (mm)**	**notch (mm)**	**precrack (mm)**	**ao (mm)**
AB Flat(X) Avg	25.44	12.31	11.35	1.53	12.90
AB Edge(Y) Avg	25.53	12.49	11.36	1.59	12.95
AB Vertical(Z) Avg	25.50	12.38	11.35	1.52	12.87
MHT Flat(X) Avg	25.42	12.37	11.33	1.33	12.66
MHT Edge(Y) Avg	25.42	12.66	11.35	1.29	12.64
MHT Vertical(Z) Avg	25.34	12.67	11.36	1.32	12.67

attachment. ASTM E1820-17a calls for measurement of crack mouth opening displacement along the load line, ASTM E399-17 calls for measurement at the front face of the specimen. Subsequent calculations for J and crack length in ASTM E1820-17a require measurement at the load line to be valid. Studies performed by Shi[54] and Sharma[55] provide corrections to accommodate measurement of crack mouth opening at the front face. Sharma's corrections utilize existing corrections for the location of a clip gauge that can be found in Figure 3.12 from ASTM E647-15 and utilized Equations 3.6 and 3.5. The coefficients for crack length calculations at the load line in ASTM E647-15 are a direct match to those found in ASTM E1820-17a Section A2.4.3. Sharma's research compared optical crack length measurements to calculated crack length values that utilized CMOD at the front face of the specimen. This method was tested and compared to the results of measurement at the load line in several steel alloys and Ti-6Al-4V and the generated results for J_{IC} and K_{JIC} were within 5% of each other. This method was specifically developed to accommodate the case where ASTM E399-17 tests do not meet the plasticity limitations and require testing by ASTM E1820-17a. MATLAB code used to process FT data can be found in Appendix B Section B.1. The required data was successfully collected but the crack curvature detailed in Section 3.5.1 resulted in invalid data.

Table 3.6. Testing Procedure for Fracture Toughness Testing

MTS Procedure for Fracture Toughness Testing	
1	Initiate dwell command in displacement control for upper axial head
2	Initiate data collection at start of test
3	Load specimen in displacement control at a rate of 0.015 mm/s to a max displacement of 1.5 mm
4	End data collection
5	Initiate dwell command in displacement control for lower axial head for 5 second.
6	Begin cycling at 12.0 kN and 1.2 kN (R=0.1) at 20 Hz to until fracture
7	MTS machine automatically shuts down when displacement exceeds 25.4 mm

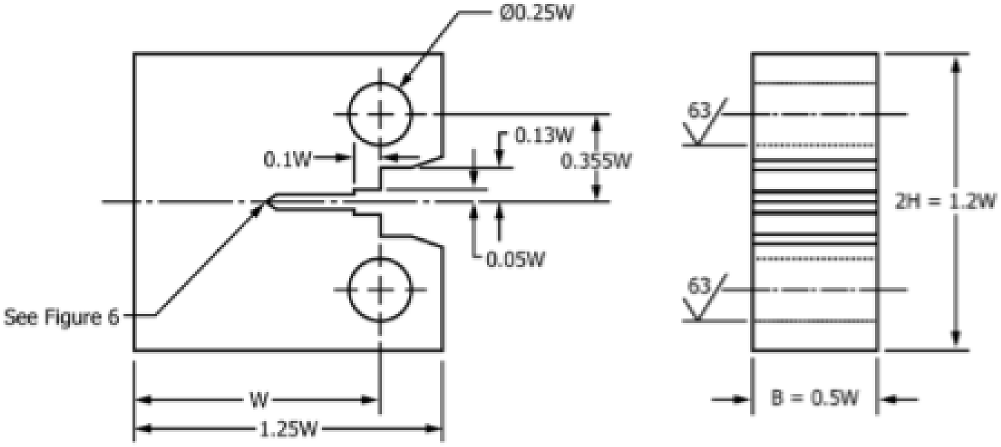

Notes:
1. Tolerance on all dimensions ±0.013W
2. Pin shall be sized so that maximum
clearance with hole is 0.02W

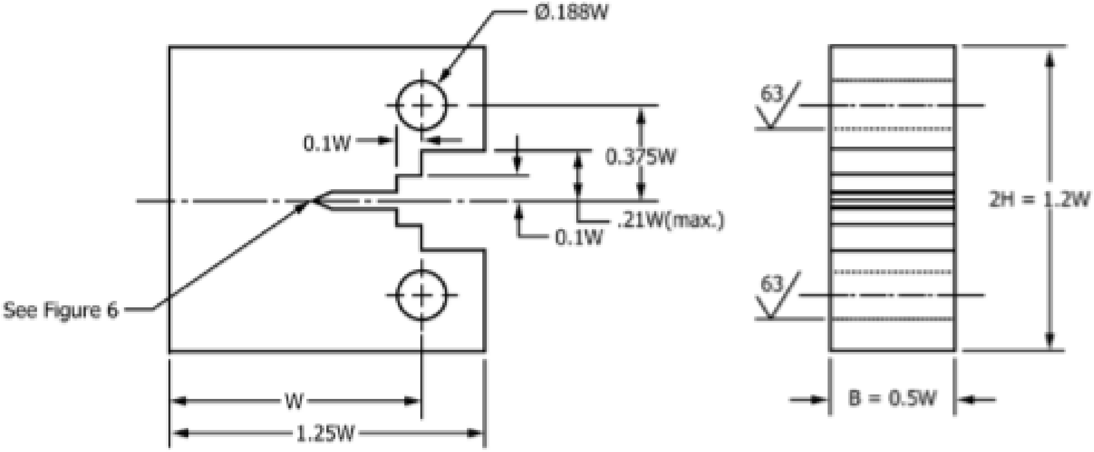

Figure 3.11. CT Specimen Design from ASTM E1820-17a[11]

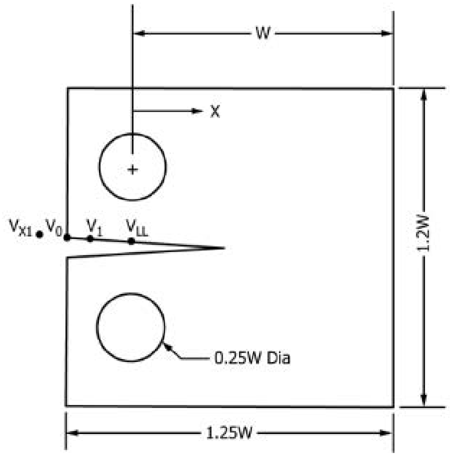

Meas. Location	X/W	C_0	C_1	C_2	C_3	C_4	C_5
C(T) Specimen							
V_{X1}	−0.345	1.0012	−4.9165	23.057	−323.91	1798.3	−3513.2
V_0	−0.250	1.0010	−4.6695	18.460	−236.82	1214.9	−2143.6
V_1	−0.1576	1.0008	−4.4473	15.400	−180.55	870.92	−1411.3
V_{LL}	0	1.0002	−4.0632	11.242	−106.04	464.33	−650.68

Figure 3.12. Different Clip Gauge Locations and Associated Coefficients for Using CMOD to Calculate Crack Length[11]

3.6 Fatigue Crack Growth Rate Testing

3.6.1 FCGR Specimen Configuration

C(T) specimens designed for FCGR testing were identical to that used for FT taken from ASTM E399-17. The only difference in design called for in ASTM E647-15 is that the specimen thickness "B" for FCGR specimens is set at 0.05W to 0.25W and rather than 0.5W. However Section A1.2.2.1 in ASTM E647-15 allows for specimen thicknesses up to 0.5W provided a crack curvature correction is applied. Crack curvature corrections were applied to the final crack length measurement and the crack curvature requirements of the standard were not violated. Creating specimens with the same design allowed for testing of both FT and FCGR without having to create a second set of gripping clevises and allowed for more rapid production of parts.

3.6.2 Fatigue Crack Growth Rate Precracking

ASTM E647-15 dictates that a fatigue precrack shall be grown to “not be less than 0.10B, h, or 1.0 mm (0.040 in.), whichever is greater” , where B is the specimen thickness and “h” is the machined notch height in Figure 3.13[12]. The specimens used in this study have a nominal value for B of 12.7mm which would result in a calculated precrack length of 1.27mm. This is less than the machined notch height of 2.03mm, thus the precrack length must be 2.03mm or larger. Testing of a C(T) specimen requires an un-cracked length that meets the conditions presented in Equation 3.4. This corresponds to a minimum ligament length of 0.6 mm for this design and material. Values used to calculate this ligament size were $K_{max} = 20$ MPa$\sqrt{m}$ and $\sigma_{ys} = 919$ MPa based on prior research by Newell and other research conducted at AFIT[4][22]. Final dimensions for each FCGR specimen can be found in Table 3.8. Differences in projected fatigue life between the different heat treatments were noticed immediately during precracking. AB specimens took between 226,000 and 492,000 cycles to grow a precrack of the appropriate length. CHT specimens took between 287,000 and 842,000 cycles to grow the same length crack. MHT specimens took significantly more cycles, between 1,018,000 and 1,717,000 cycles, to grow appropriately sized precracks.

$$(W - a) \geq (4/\pi) * (K_{max}/\sigma_{ys})^2 \tag{3.4}$$

Similar to FT tests, the fatigue cracking process must be carefully controlled in FCGR testing to ensure the validity of the data obtained. ASTM E647-15 recommends that precracking be conducted at the same stress ratio as the final test, in this case R = 0.1. FCGR precracking is to be conducted such that the K_{max} value during precracking does not exceed the initial K_{max} value during testing. The precracking conditions outlined in Table 3.7 ensured that these requirements were met. Values

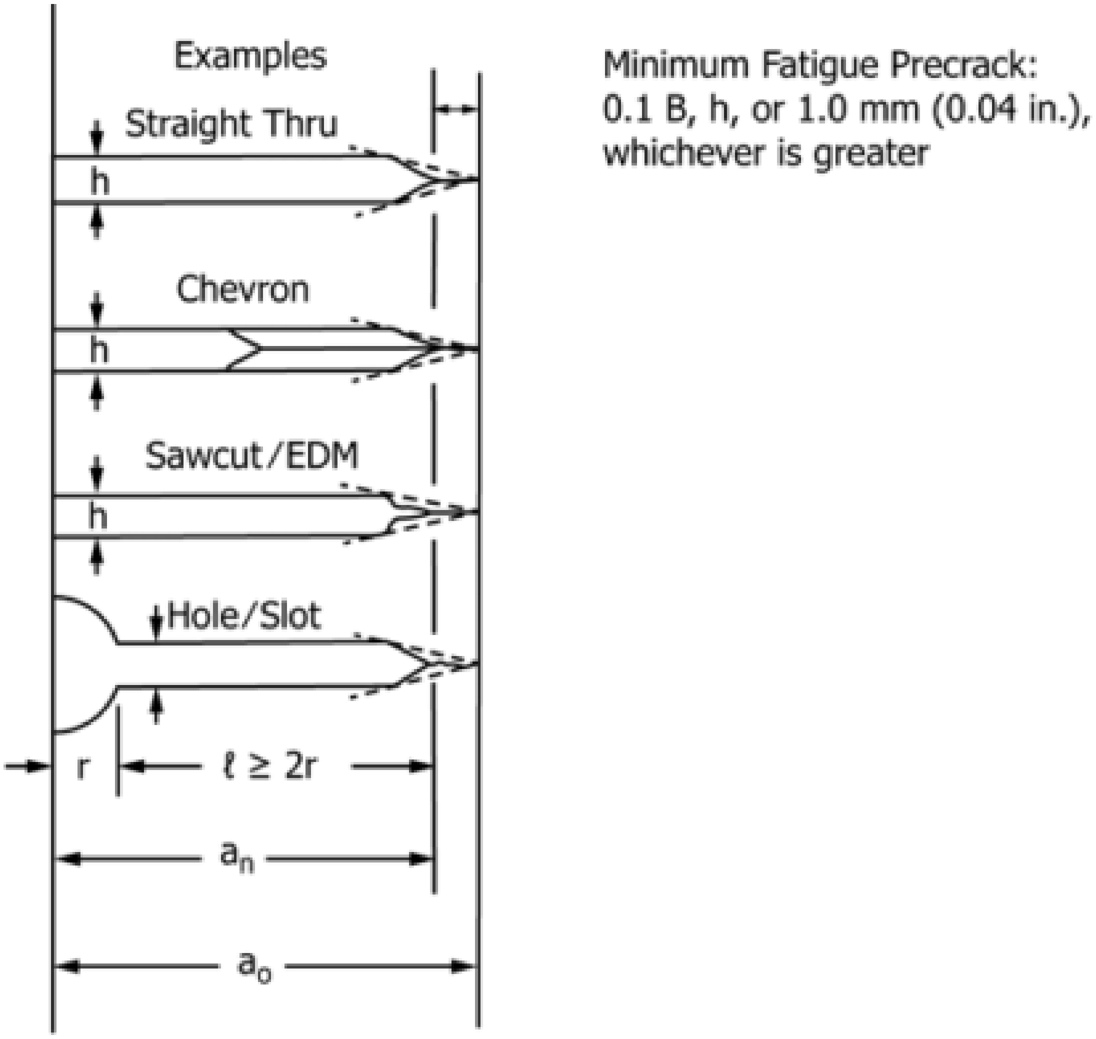

Figure 3.13. CT Notch Design[12]

for initial K_{max} are based on data from research which indicated the beginning of the Paris region is around 20 MPa$\sqrt{m}$ for wrought IN718 [51]. This precracking process resulted in the desired sharp crack tip require for stress concentration and removal of previous loading history effects.

3.6.3 Fatigue Crack Growth Rate Procedure

To accomplish the goal of comparing heat treatments and anisotropic effects in FCGR the following procedure was utilized. Testing was conducted using the constant

Table 3.7. Fatigue Crack Growth Rate Precracking Conditions

Max Load (kN)	Min Load (kN)	Stress Ratio	Frequency (Hz)
3.0	0.3	0.1	50

Table 3.8. Fatigue Crack Growth Rate Specimen Dimensions

Specimen	W (mm)	B (mm)	notch (mm)	precrack (mm)	ao (mm)
AB Flat(X) Avg	25.49	12.58	11.35	1.93	13.28
AB Edge(Y) Avg	25.47	12.64	11.33	2.14	13.47
AB Vertical(Z) Avg	25.47	12.61	11.32	2.13	13.45
MHT Flat(X) Avg	25.43	12.63	11.36	2.08	13.44
MHT Edge(Y) Avg	25.43	12.63	11.35	2.23	13.57
MHT Vertical(Z) Avg	25.46	12.63	11.33	2.23	13.56
CHT Flat(X) Avg	25.43	12.65	11.43	2.16	13.59
CHT Edge(Y) Avg	25.34	12.66	11.32	2.53	13.85
CHT Vertical(Z) Avg	25.39	12.66	11.33	2.54	13.86

force amplitude procedure outlined in ASTM E647-15 Section 8.5. A load was applied to the C(T) specimens in force control mode, with a set stress ratio of R=0.1 chosen for this research. AB specimens were cycled at a rate of 10 Hz with corresponding peak and minimum force values of 3.0 kN and 0.3 kN for the entire duration of the test. Several MHT specimens were initially run with peak and minimum force values of 3.0 kN and 0.3 kN at 50 Hz until the equipment was unable to accurately produce the required force levels. This occurred nominally between 300,000 and 400,000 cycles. The remainder of the tests of the MHT and CHT specimens were tested start to finish at 10 Hz. A total of 45 specimens were tested for FCGR: 15 in the AB condition, 15 in the CHT condition, and 15 in the MHT condition. For each of these conditions there were 5 specimens tested for each of the specimen build orientations.

Optical measurements of the surface crack were taken to complement the data recorded by the clip gauge. Optical measurements were taken in an automated process every 500 cycles during testing. Using the software built into the MTS controller a digital signal could be sent to trigger the digital camera based on the number of

Table 3.9. **Testing Procedure for Fatigue Crack Growth Rate Testing**

MTS Procedure for Fatigue Crack Growth Rate Testing	
1	Initiate dwell command in displacement control for upper axial head
2	Begin force ramp up to 2.5 kN
3	Initiate dwell command in force control for lower axial head for 5 seconds
4	Send digital out signal to take initial crack image
5	Begin cycling at 3.0 kN and 0.3 kN at 10 Hz. (Data collection only occurs during cycling)
6	When cycles count reaches 500, ramp force to 0.5 P_{Max} (1.5 kN)
7	Initiate dwell command in force control for lower axial hydraulic head for 5 seconds
8	Send digital out signal to take crack image
9	Return to Step 5 and repeat Steps 5-9 until specimen fails
10	MTS machine automatically shuts down when displacement exceeds 25.4mm

cycles run. This signal was passed through a National Instruments Digital In/Out 6229 Universal Serial Bus before being received by a MATLAB script developed in house to trigger the Pixel Link digital camera. Equipment limitations allowed for imaging of only the front side of the specimen. Images were assigned file names relating to the number of cycles when the image was taken and were stored for later analysis. Due to the volume of data taken in this process the script required resets at periodic points in the test to allow sufficient available memory. Optical crack length measurements of the precrack and of the final fracture surface were used to correct for crack lengths calculated from CMOD data. This data was used to provide a linear correction to the CMOD based crack length readings. This process provided satisfactory results and was used to confirm the accuracy of calculated crack length readings.

3.6.4 Fatigue Crack Growth Calculations

CMOD, force, and number of cycles were recorded and used to calculate the crack length and the stress intensity factor. The crack length was determined by measuring CMOD with a clip gauge extensometer and performing calculations as laid out in Equations 3.6 and 3.5. Stress intensity factor range is calculated via Equation 3.7[12]. Code developed by James Larsen, Jay Jira, and Kakkaveri Ravichandran was used to determine crack growth rate ($\frac{da}{dN}$) vs stress intensity factor range (ΔK)[56]. This code was developed based on the incremental polynomial method listed in ASTM E647-15 (Appendix X1.2) and uses a seven point system to create the data for $\frac{da}{dN}$ and ΔK. Following this process, plots of $\frac{da}{dN}$ vs ΔK were created for each specimen and for the various conditions tested. MATLAB code used to generate crack length values and cycle count can be found in Appendix B Section B.2.

$$u_x = \sqrt{\frac{E * CMOD * B}{P}} + 1 \tag{3.5}$$

$$\begin{aligned} \alpha = a/W =& 1.0010 - 4.6695 * u_x + 18.460 * u_x^2 \\ & - 236.82 * u_x^3 + 1214.9 * u_x^4 - 2143.6 * u_x^5 \end{aligned} \tag{3.6}$$

$$\Delta K = \frac{\Delta P}{B * \sqrt{W}} * \frac{2+\alpha}{(1-\alpha)^{\frac{3}{2}}} * (0.866 + 4.64 * \alpha - 13.32 * (\alpha)^2 + 14.72 * (\alpha)^3 - 5.6 * (\alpha)^4) \tag{3.7}$$

For each of the nine experimental conditions a power law fit was computed to represent Region 2 behavior. This was accomplished for ΔK between 30 and 50 MPa$\sqrt{m}$. Power law fits take the form of Equation 3.8 as developed by Paris [24]. This power law can be used to compute a fatigue crack growth life (N_f), given an applied stress range ($\Delta\sigma$), initial crack length (a_o), and final crack length (a_f). This derivation is shown in Equations 3.8- 3.11[57]. In this derivation $\Delta K = Y\Delta\sigma\sqrt{\pi a}$ where a is the crack length and Y is a geometry correction factor. Equation 3.6 is valid for $m \neq 2$ and $Y = constant$. In this study, $Y = 1.122$, corresponding to an edge crack in an infinite medium. Equation 3.6 was used to demonstrate the differences in damage tolerance due to the differences in orientations and heat treatments, as discussed later in Section 4.4.1.

$$\frac{da}{dN} = C\Delta K^m \tag{3.8}$$

$$\frac{da}{dN} = C(Y\Delta\sigma\sqrt{\pi a})^m \tag{3.9}$$

$$CY^m(\Delta\sigma)^m\pi^{m/2}\int_0^{N_f} dN = \int_{a_o}^{a_f}\frac{da}{a^{m/2}} \tag{3.10}$$

$$N_f = \frac{2}{(m-2)CY^m(\Delta\sigma)^m\pi^{m/2}}\left(\frac{1}{(a_o)^{(m-2)/2}} - \frac{1}{(a_f)^{(m-2)/2}}\right) \quad for\ m \neq 2 \tag{3.11}$$

3.6.5 Exclusion of Data

Due to irregularities during testing four specimens were removed from consideration while generating results. An early test on specimen MHT Vertical(Z) 3 was run at 50Hz but was unable to keep the desired force range as the crack length increased. This led to a changing R ratio during the test and that sample was excluded from further calculations. Two of the MHT specimens, Edge(Y) 1 and Edge(Y) 2, were initially cycled at higher frequencies until the force range became unreliable but were then stepped down to 10 Hz for the remainder of testing. This caused an artificial drop in the crack growth rate, skewing the results of the average crack rate fit and required exclusion of these samples. The final excluded specimen was the first test in the AB heat treatment. The test profile for this specimen, AB Flat(X) 1, included periodic stops to allow for optical image collection. During these pauses data collection was not stopped and caused errant crack length readings which resulted in unusable data. The data from these four specimens was not used for calculation of $\frac{da}{dN}$ or ΔK. The exclusion of data from these specimens allowed for accurate measurement of FCGR without introducing undue bias to the experimental procedure.

3.7 Fracture Surface Analysis

Initial fatigue tests performed during experimental set up revealed evidence of the specimen build orientation in the fracture surface that was visible to the naked eye. Thus fracture surface analysis was used to quantify the results. This was accomplished by means of a white light macroscope and a laser scanning microscope capable of analyzing the fracture surfaces and producing surface roughness results. The specific devices used were a Keyence VR-3200 3D Measurement Macroscope and a Zeiss Axio Observer.Z1 Laser Scanning Microscope, respectively. Specimen imaging was conducted at 25X magnification on the macroscope. Multiple images of the surface were taken and stitched together by the device's software. For FT tests, roughness measurements were taken in the precrack region and in the fracture region. In the fracture region measurements were taken parallel and perpendicular to the crack front. Surface area roughness measurements were also taken in both the precrack and fracture regions. All FT specimens were measured using the macroscope. Prior to examination of the FCGR fracture surfaces the macroscope failed and evaluation was moved to the Zeiss Observer.Z1 for all FCGR specimens. This method of examination provided topographic maps of a small area of the fracture surface with corresponding surface roughness values. Optical images of the FCGR surfaces were taken using an Zeiss Discovery V.12 Stereo Microscope. These devices are shown in Figure 3.14. One representative image for each surface roughness evaluation technique is included in Figure 3.15. The results of fracture surface analysis are discussed in Sections 4.2.1 and 4.4.3.

(a) Zeiss Axio Observer.Z1 - Laser Scanning Microscope

(b) Keyence VR-3200 3D Measurement Macroscope[58]

(c) Zeiss Discovery V.12 Stereo Microscope

Figure 3.14. Fracture Surface Evaluation Equipment

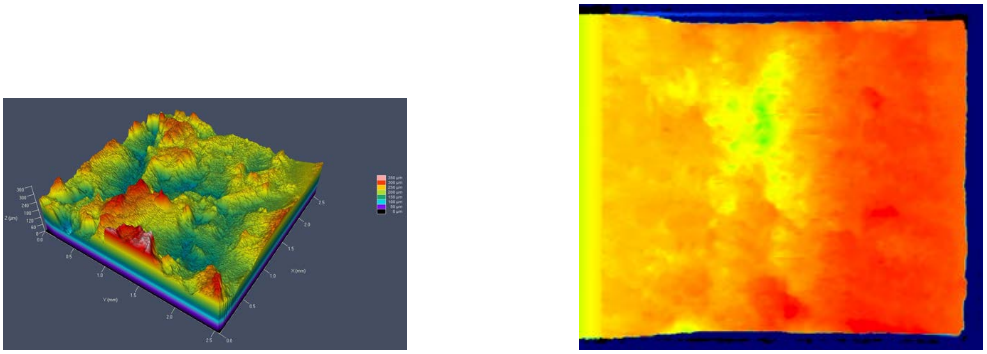

(a) Laser Scanning Microscope Image of a FCGR Surface in the MHT condition

(b) Keyence Macroscope Image of a FT Surface in the MHT condition

Figure 3.15. Fracture Surface Evaluation Outputs. Topographic maps and heat maps were used for reference only. Both devices calculated area surface roughness measurements in the area of interest for later evaluation.

3.8 Chapter 3 Summary

This chapter summarizes the methods used to conduct FT and FCGR testing of AM IN718. Several deviations were made from the standard practices laid out in the associated ASTM E1820-17a and ASTM E647-15 to meet the unique needs and complications presented before and during testing. The methods described were chosen to compare the results between build orientations and heat treatments of C(T) specimens. After the FT testing was completed, fracture surface evaluations were conducted to track trends in specimen build orientation and heat treatment effects. Testing was accomplished using hydraulic tension testing equipment, computational software, optical imaging equipment, and surface roughness measurement devices. The results of this research are discussed in the following chapter.

IV. Results

4.1 Chapter 4 Overview

The goal of this research was to characterize the fracture toughness and fatigue crack growth rate for Inconel 718 (IN718) manufactured by Laser Powder Bed Fusion (LPBF). Specimens were built in the Flat(X), Edge(Y), and Vertical(Z) directions, see Figure 3.10 and post-processed in the three separate heat treatments described in Section 2.3. The three heat treatments were: as-built (no post-production heat treatment), the standard IN718 heat treatment for wrought material as prescribed by American Society for Testing and Materials B637 (ASTM B637), and a modified heat treatment optimized to produce re-crystallization and isotropic material behavior for IN718 LPBF parts. The three build orientations allowed for measurements with crack front orientations parallel to the build direction, perpendicular to the the build directions, and through the build direction of the resulting additively manufactured material. Specimen fracture surfaces were evaluated for surface roughness measurements and characterized to examine trends between heat treatments and specimen build orientations. Examination of these variables allowed for a broad understanding of Fracture Toughness (FT) and Fatigue Crack Growth Rate (FCGR) and the production variables that may affect the final product and influence the suitability of LPBF IN718 for use in Air Force applications.

4.2 Fracture Toughness Results

FT testing was conducted to characterize how the material properties of LPBF IN718 are affected by the various heat treatments applied and the different specimen build orientations. This testing was accomplished using 30 Compact Tension (C(T)) specimens, providing 5 individual tests for each orientation in the As-Built (AB) condition and in the Modified Heat Treatment (MHT) condition. As noted earlier the experiment was initially designed to test via American Society for Testing and Materials E399-17 (ASTM E399-17) utilizing linear elastic fracture mechanics but extensive plasticity was encountered during initial tests which required diverting testing to the methods described in American Society for Testing and Materials E1820-17a (ASTM E1820-17a). Because specimen production had already been completed, the existing specimens designed to the standards of ASTM E399-17 were utilized for testing under the conditions of ASTM E1820-17a. This required adjustments to the calculation of crack length. This adjustment was made using corrections found in research by V.M.J. Sharma of the Vikram Sarabhai Space Center in India[55] and are detailed in Section 3.5.3. The process used is very similar to the crack length calculations that are presented in American Society for Testing and Materials E647-15 (ASTM E647-15) later in this research for FCGR. The crack length calculation process is described in detail in Section 3.5.3. FT results are shown in Table 4.1. Specimens marked with an asterisk were tested by ASTM E399-17. However, due to extensive plasticity and resulting crack front curvature none of the tested specimens met the validity requirements of ASTM E1820-17a Sections 9.1.4.1 and 9.1.4.2. These sections require nine crack measurements of the original and final crack size to be within 5% of the material thickness or approximately 0.6mm for specimens used in this research. An example of final crack size measurements can be found in Figure 4.1. Future FT testing of IN718 should include side grooving C(T) specimens as described in ASTM E1820-17a Section 7.5. This should reduce crack curvature and produce results that meet the validity requirements. Side grooving should be conducted after precracking and should not reduce the specimen thickness by more than 25%. Individual and average J_{IC} and K_{JIC} values for each orientation and heat treatment are included but do not represent data valid by the standards of ASTM E1820-17a. The large variation in the calculated values of J_{IC} and K_{JIC} reflect the lack of validity in these tests. Plots of the Crack Extension vs J and Crack Mouth Opening vs Force are included for each test condition in Figures 4.2-4.4. These plots show that specimens with the MHT required higher levels of loading than the AB specimens to reach the desired amount of displacement. Comparisons of J_{IC} and K_{JIC} of the various heat treatments and specimen build orientations are shown in Figure 4.5-4.10. These charts show wide variation between the calculated values of J_{IC} and K_{JIC} further illustrating the issues encountered during testing. The result of the extensive crack curvature is that crack length measurements calculated from CMOD or taken from optical measurements do not reflect the actual amount of crack growth in the specimen. This leads to a severe skewing of the J vs crack extension plot. Because J_{IC} is extracted from this curve by a series of construction lines the resulting value of J_{IC} and K_{JIC} cannot be relied on to be accurate.

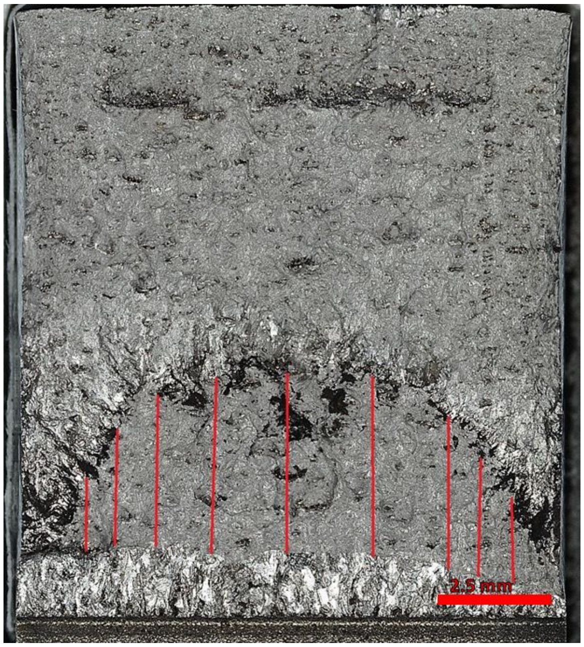

Figure 4.1. Final crack size measurements showing excessive crack front curvature. The maximum measured difference is 3.35 mm

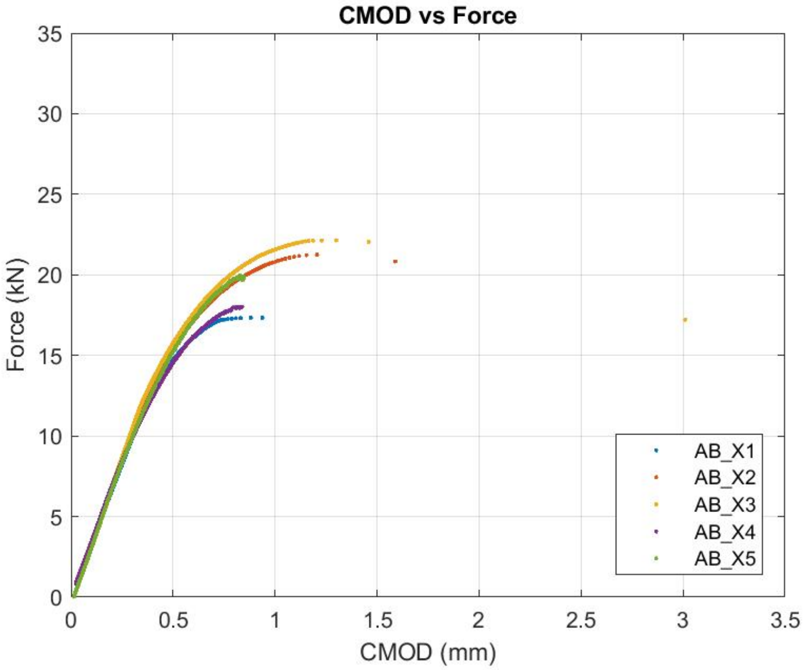

(a) AB

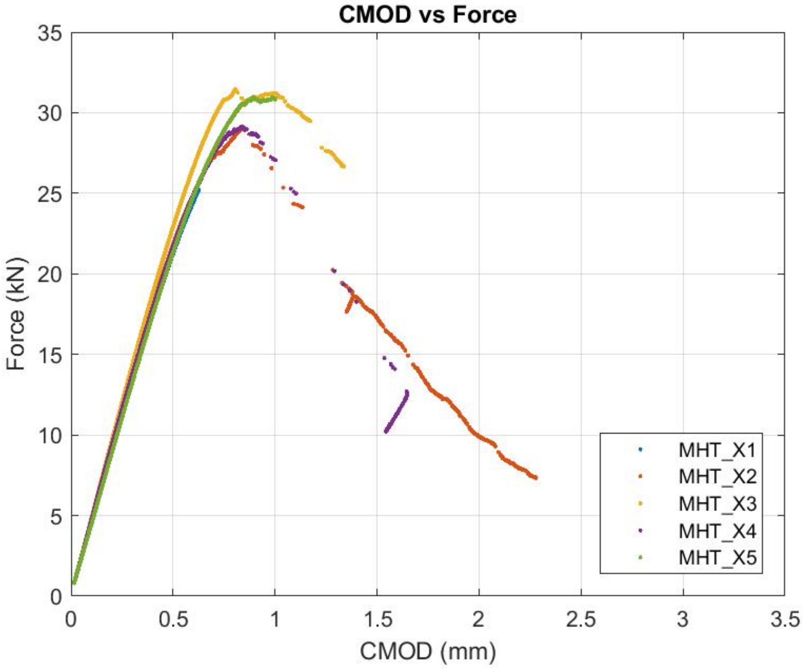

(b) MHT

Figure 4.2. Flat(X) Build Orientation Force vs CMOD, MHT specimens consistently show increased loads required to reach the desired displacement

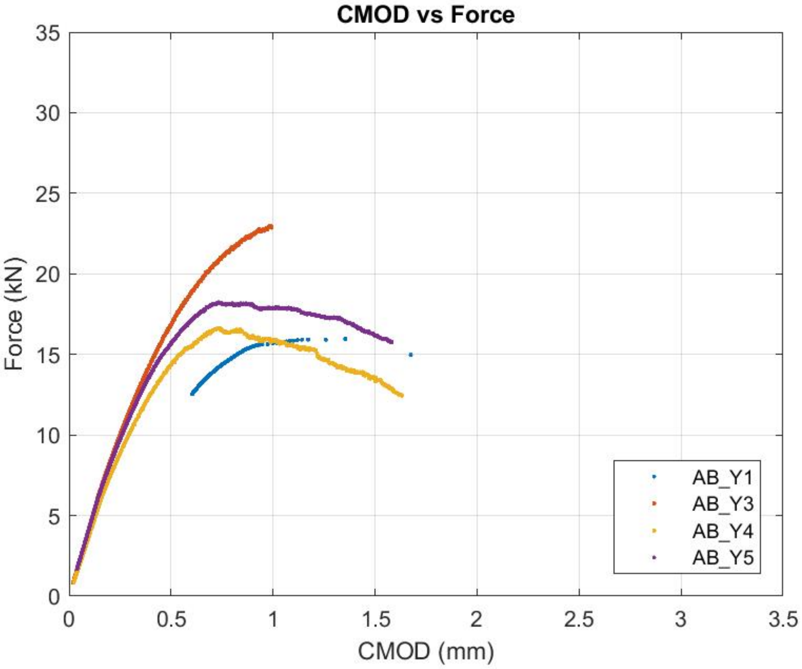

(a) AB

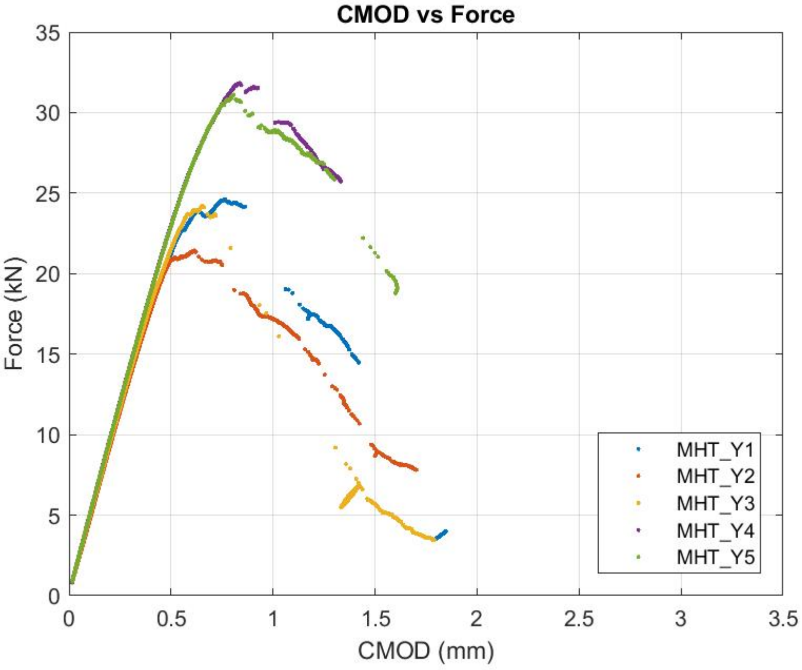

(b) MHT

Figure 4.3. Edge Build Orientation Force vs CMOD, MHT specimens consistently show increased loads required to reach the desired displacement

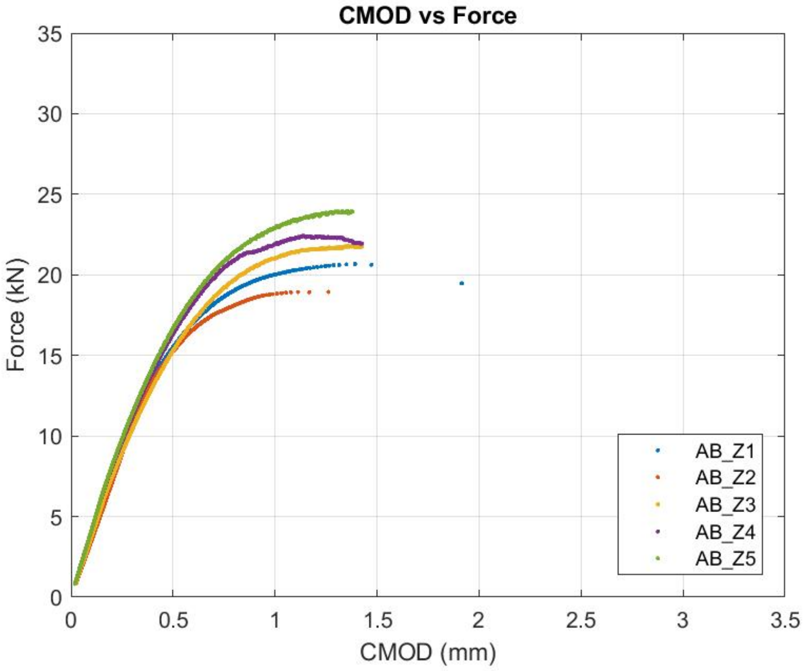

(a) AB

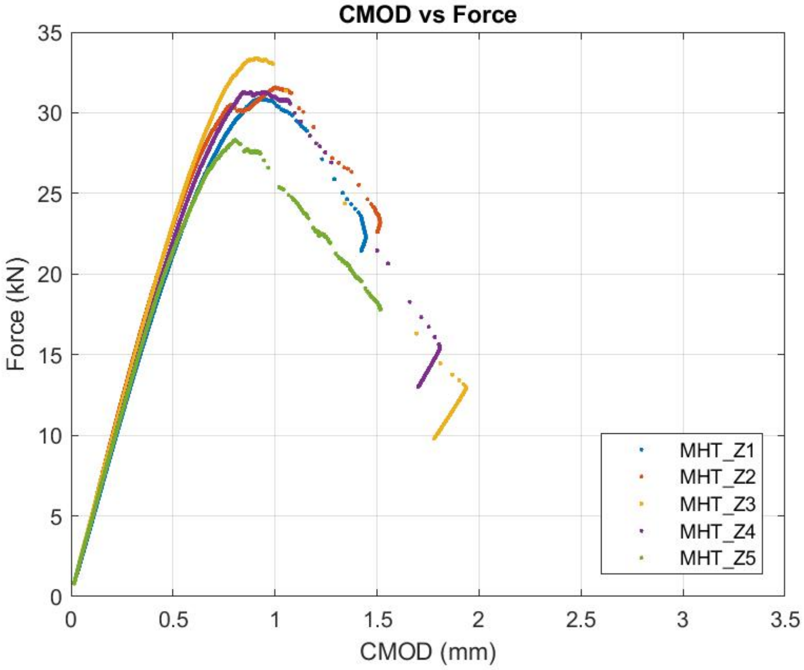

(b) MHT

Figure 4.4. Vertical(Z) Build Orientation Force vs CMOD, MHT specimens consistently show increased loads required to reach the desired displacement

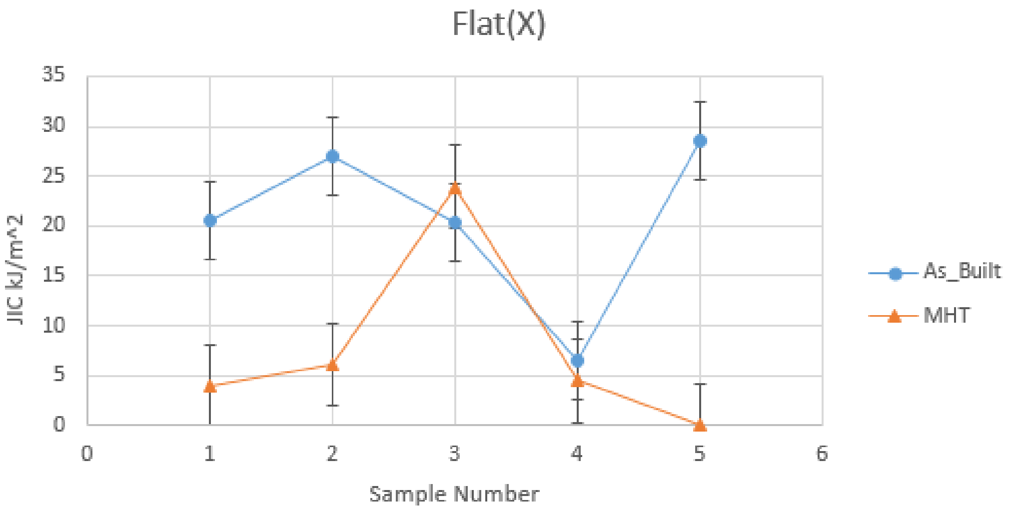

Figure 4.5. JIC Values for MHT and AB Specimens in the Flat(X) specimen build orientation, wide scatter of data points shows lack of correlation between test results, Invalid Data

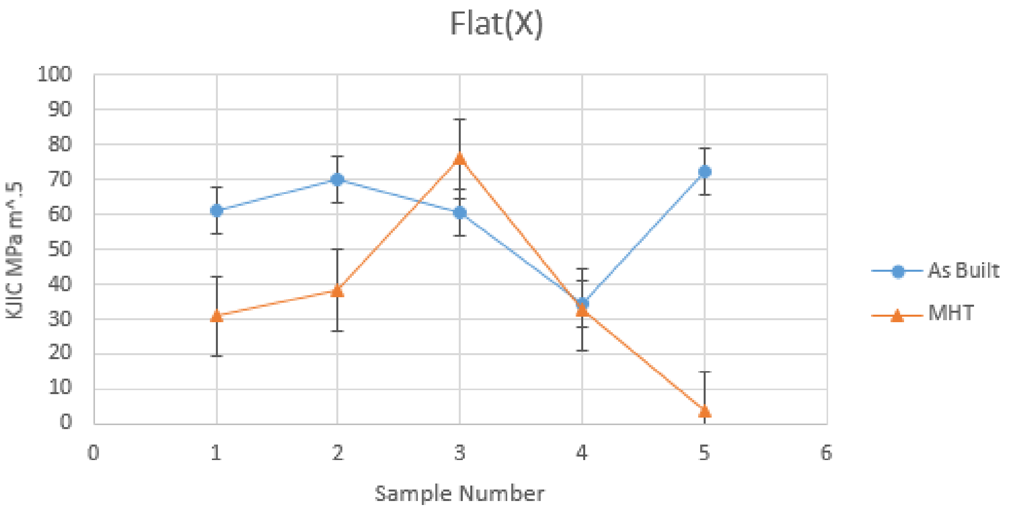

Figure 4.6. KIC Values for MHT and AB Specimens in the Flat(X) specimen build orientation, wide scatter of data points shows lack of correlation between test results, Invalid Data

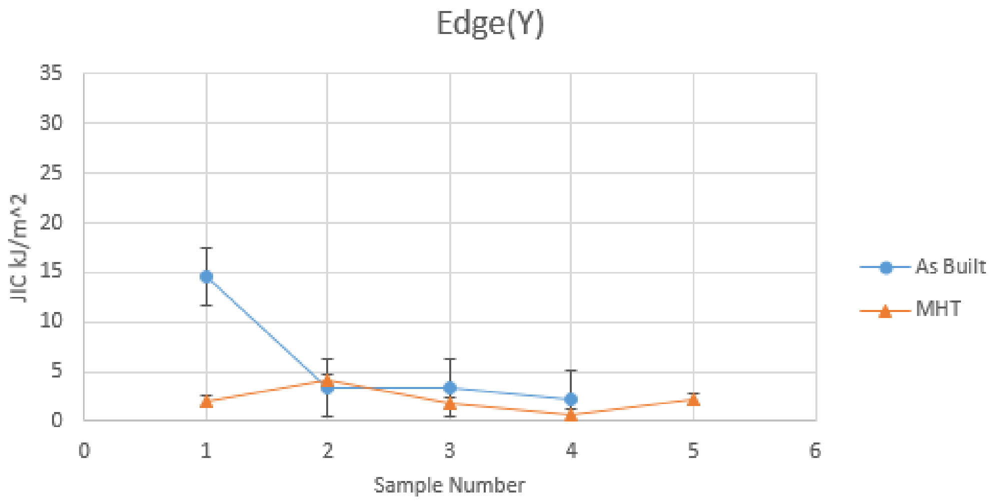

Figure 4.7. J_{IC} **Values for MHT and AB Specimens in the Edge(Y) specimen build orientation, Invalid Data**

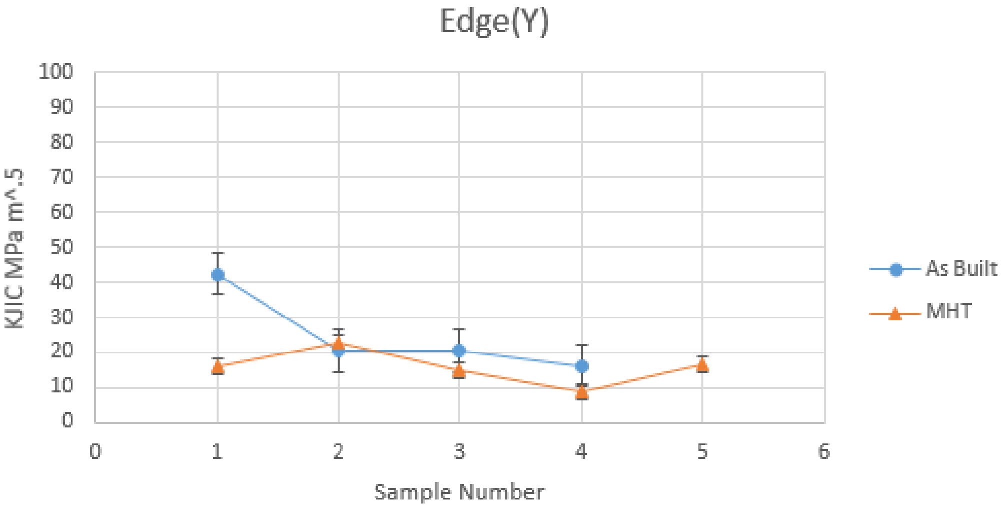

Figure 4.8. K_{JIC} **Values for MHT and AB Specimens in the Edge(Y) specimen build orientation, Invalid Data**

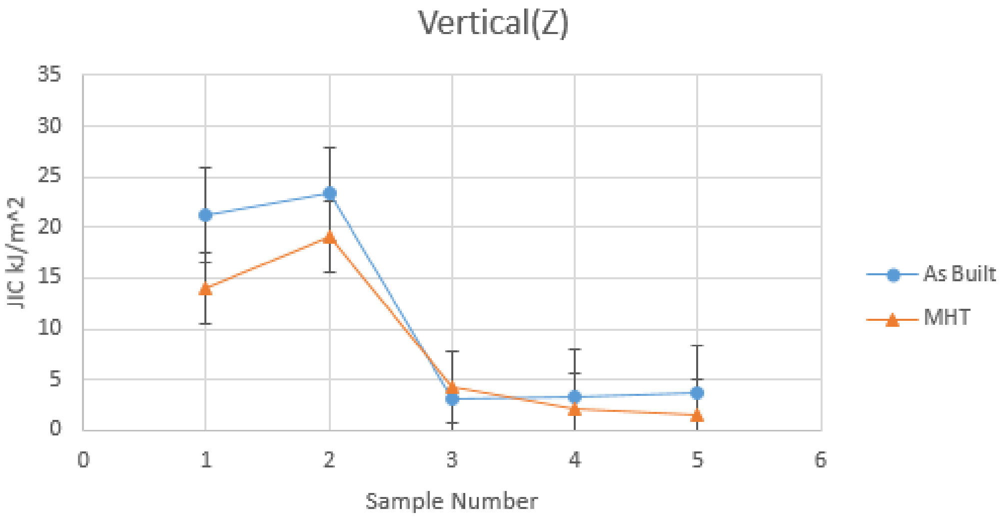

Figure 4.9. J_{IC} **Values for MHT and AB Specimens in the Vertical(Z) specimen build orientation, apparent trends between samples 1-2 and 3-5 do not represent material trends and are a product of the specimen naming scheme, Invalid Data**

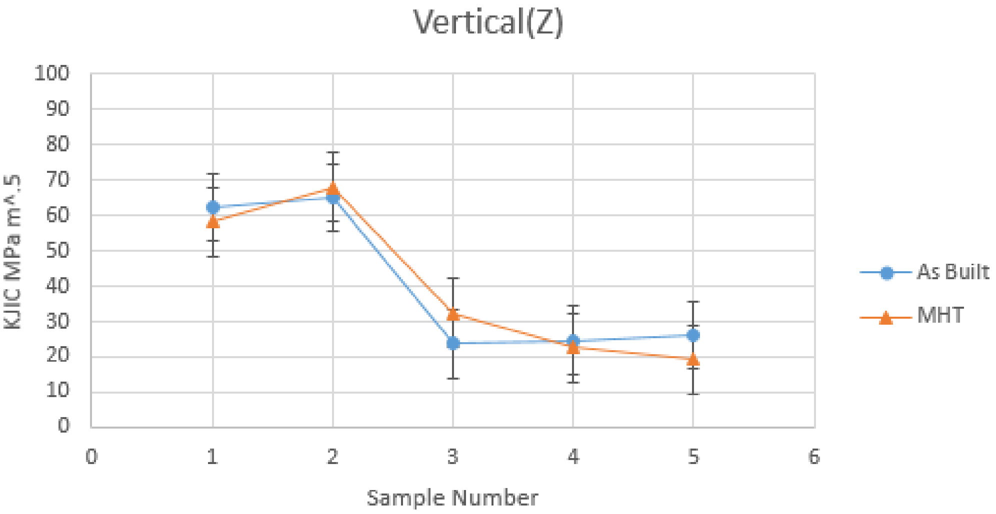

Figure 4.10. K_{JIC} **Values for MHT and AB Specimens in the Vertical(Z) specimen build orientation, apparent trends between samples 1-2 and 3-5 do not represent material trends and are a product of the specimen naming scheme, Invalid Data**

Table 4.1. Fracture Toughness Results (Invalid data due to crack front curvature)

Specimen	**JIC** (kJ/m^2)	**KJIC** ($MPa/\sqrt{m}$)
AB Flat(X) Avg	20.59	59.79
AB Edge(Y) Avg	8.81	31.92
AB Vertical(Z) Avg	10.92	40.33
HT Flat(X) Avg	7.70	36.37
HT Edge(Y) Avg	2.16	15.77
HT Vertical(Z) Avg	8.22	40.04
Wrought [59][60]	59-80	73-96.3

4.2.1 Fracture Toughness Surfaces

Fracture surface evaluation was conducted after unique surface features were identified corresponding to each specimen build orientation. FT specimen fracture surfaces were analyzed using a white light macroscope to characterize the surface roughness of the region of the fatigue precrack and the region of the crack growth during fracture toughness testing. FT specimens showed a high degree of plasticity and ductile tearing in the final fracture regions. Evidence of extensive porosity is also present. One key fracture surface feature noted was the presence of layered surfaces corresponding to the specimen build orientation as seen in Figures 4.11 and 4.12. In the Flat(X) specimen build orientation, alignment and elongation of pores can be seen perpendicular to the advancing crack front. These features correspond to the layer stacking in the build direction. A similar effect can be seen in the Vertical(Z) specimen build orientation but with the layers parallel to the crack front. In the Edge(Y) specimen build orientation the surface features are different. Pores appear more circular and are evenly distributed rather than aligned. Additionally bright spots in the final fracture regions correspond to the laser path during fabrication. All these features are present in both the MHT and AB specimens. This is an indication that there is incomplete fusion during the printing process and that the MHT does not fully remove the effects of layered production. Evidence of crack curvature is also readily apparent in the fracture surfaces. Table 4.2 shows surface roughness measurements taken from the FT specimens but no discernible pattern is noticeable. These unique effects were consistent across the range of specimens tested in all specimen build orientations and heat treatments.

(a) AB Flat(X) **(b)** AB Edge(Y) **(c)** AB Vertical(Z)

Figure 4.11. Comparison of AB fracture surfaces showing the influence of specimen build orientation.

(a) MHT Flat(X) **(b)** MHT Edge(Y) **(c)** MHT Vertical(Z)

Figure 4.12. Comparison of MHT fracture surfaces showing decreased influence of specimen build orientation compared the the AB condition.

Table 4.2. Fracture Toughness Roughness Averages

Specimen	**Fracture Region Sa μm**
AB Flat(X) Avg	214.528
AB Edge(Y) Avg	260.232
AB Vertical(Z) Avg	191.270
MHT Flat(X) Avg	246.606
MHT Edge(Y) Avg	231.666
MHT Vertical(Z) Avg	187.532

4.3 Fracture Toughness Results Summary

Fracture toughness testing revealed high levels of plasticity during testing. This rendered early test runs by ASTM E399-17 invalid. LPBF IN718 requires testing by ASTM E1820-17a due to this extensive plasticity. Furthermore due to the extensive plasticity, specimens tested by ASTM E1820-17a showed extensive crack curvature which invalidated the calculated values for J_{IC} and K_{JIC}. Observations of CMOD vs Force plots, Figures 4.2-4.4, shows that the MHT specimens required more force than AB specimens to reach the displacement maximum of 1.5mm. This corresponds with tensile data taken for these two conditions and may indicate an improvement in FT with the MHT but no conclusive statements can be made[22]. Future fracture toughness testing should incorporate side grooves into the design of C(T) specimens as described in ASTM E1820-17a Section 7.5.

4.4 Fatigue Crack Growth Testing Results

4.4.1 Fatigue Crack Growth Rate Results

FCGR testing was conducted to determine the effects of specimen build orientation and heat treatment on anisotropic fatigue crack growth behavior. This was facilitated using 45 C(T) specimens, providing 5 individual tests for each orientation in each of the heat treatment conditions. MHT specimens withstood 272,000 cycles to 721,000 cycles before failure across all directions. Conventional Heat Treatment (CHT) and AB specimens failed between 82,000 cycles to 281,000 cycles. Cycles to failure is not an exact correlation to FCGR, due to differences in the length of precracking, but it mirrors the trend seen in the FCGR results. Due to plasticity limitations data taken when the ratio of crack length to specimen width, $\frac{a}{W}$, exceeds 0.8 is considered to be invalid. These data points are included in Figures A.3 - A.8 for reference but were excluded in calculations. FCGR's were compared where ΔK was between 30 and 50 MPa$\sqrt{m}$ establishing a representative section of Region 2 crack growth. Table 4.3 shows a power law fit for each of the experimental conditions including different heat treatments and specimen build orientations for ΔK between 30 and 50 MPa$\sqrt{m}$. Figure 4.13 shows a comparison of these power laws for all nine experimental conditions. This plot shows decreased FCGR across all stress intensity values for the MHT specimens. Also included in this plot is a power law representation of data from a study by Konecna for AB IN718. The data from Konecna's study was only taken to ΔK = 20 MPa$\sqrt{m}$ and the power law given was extended to compare with the data from this research. Specimens subjected to the MHT showed greatly decreased FCGR's compared to both CHT and AB specimens. A plot of the power law for each specimen build orientation can be seen in Figure 4.14 again showing the lowest FCGR's for MHT specimens. CHT specimens show lower FCGR's in the Flat(X) and Vertical(Z) specimen build orientations compared to AB specimens but much higher growth rate in the Edge(Y) direction. Dashed lines in these plots represent a 95% confidence band around the mean of the respective heat treatments.

Fatigue crack growth lives were computed using Equation 3.6 with an initial crack length of 0.6 mm and a final crack length of 3.5 mm. Applied stress ranges included 500, 600, and 700 MPa which approximated the stress intensity factor range over which the power laws were generated. Figure 4.15 compares the fatigue crack growth life between the same specimen build orientations with different heat treatments for the stress range of 500 MPa. For this test condition MHT specimens show fatigue crack growth lifetimes that are approximately 2.5 - 3.5 times longer than for AB specimens and 1.3 - 6.0 times longer than for CHT specimens. Similar results were seen at the 600 and 700 MPa stress ranges and are shown in Appendix A. One reason that MHT specimens display lower FCGR is related to the increase in grain size.

This effect can be seen in Figure 2.4. After the MHT the effective distance the crack travels increases as the crack navigates around the larger grains. This effect is confirmed in examination of the fracture surfaces and is discussed in more detail in Section 4.4.3. The aging process of the MHT and CHT allows the critical growth of γ" precipitates. These precipitates are the key strengthening factor in IN718 and are not present in any significant quantity after the printing process[4]. Growth of these precipitates requires the fatigue crack to divert its direction or expend more energy to shear the particles before it can progress further in the bulk material. All these factors contribute to the large decrease in FCGR between the MHT and AB specimens. As seen in Figure 2.4 the microstructure of the AB and CHT conditions are very similar. Both display the typical columnar grain structure associated with LPBF in the build direction as well as associated small grain size. The similarity in microstructure mimics the similarity of change in growth rate between the AB and MHT and the CHT and MHT. While the CHT provides the same aging treatment and grows the characteristic γ" precipitates, the one hour anneal at 1010°C does not provide re-crystallization as seen with the MHT. This indicates that while the growth of γ" precipitates benefits the mechanical properties of IN718, the bulk of the decrease in FCGR in the MHT specimens is the result of grain growth. The effect of the CHT compared to the AB condition is less clear. In the Flat(X) and Vertical(Z) specimen build orientations the growth rate of CHT specimens is lower. The opposite effect is seen comparing AB and CHT growth rates in the Edge(Y) direction. These effects are also seen in Table A.4. Specimens tested in with the CHT in the Edge(Y) specimen build orientation show the highest FCGR in this research.

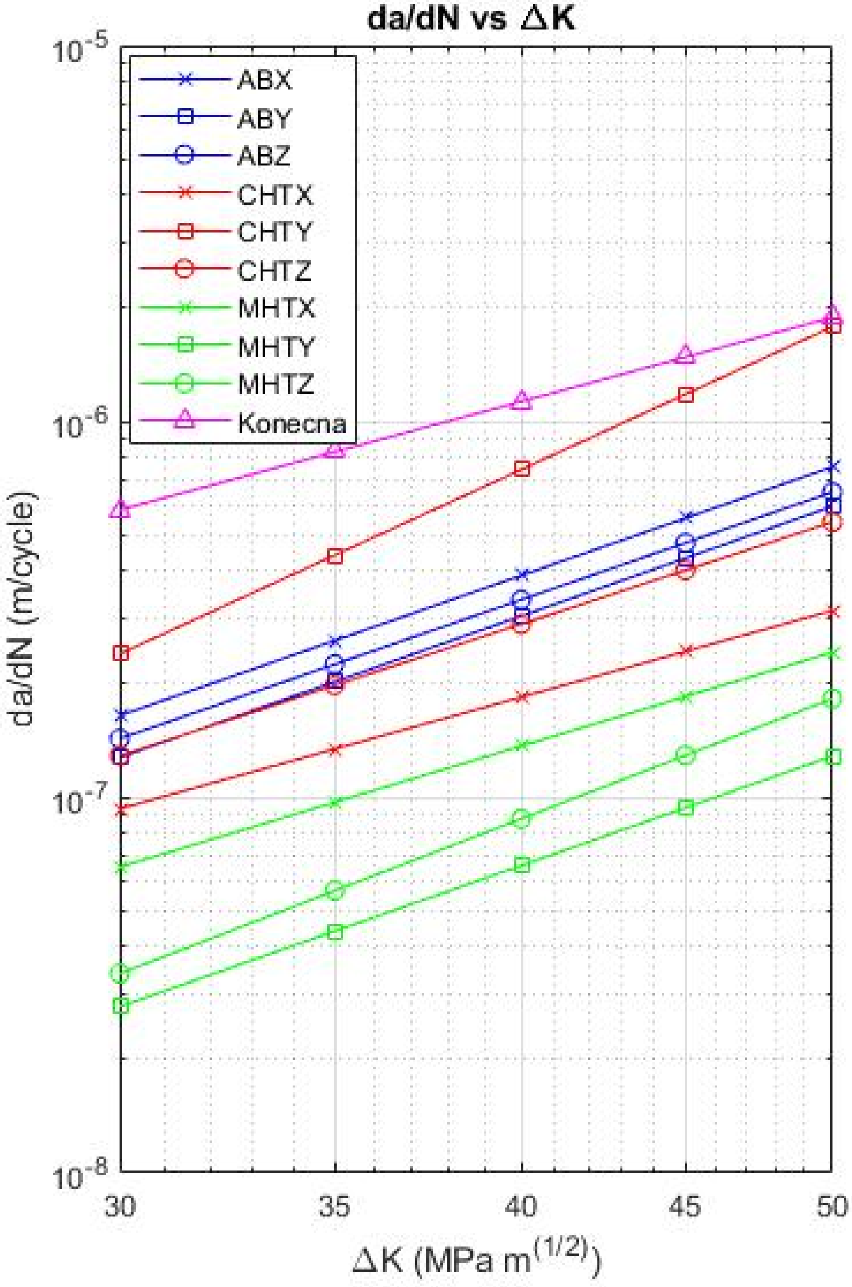

Figure 4.13. Power Law Fit Results in the range of ΔK between 30 and 50 MPa$\sqrt{m}$. MHT specimens show lower FCGR in all build orientations. Data published by Konecna on LPBF IN718 is included for reference [13]

Table 4.3. Power Law Equation for Region 2 FCGR Between ΔK = 30 - 50 MPa$\sqrt{m}$

	Power Law Fit
AB Flat(X)	$\frac{da}{dN} = 6.605 * 10^{-12} * \Delta K^{2.985}$
AB Edge(Y)	$\frac{da}{dN} = 4.539 * 10^{-12} * \Delta K^{3.012}$
AB Vertical(Z)	$\frac{da}{dN} = 6.113 * 10^{-12} * \Delta K^{2.958}$
CHT Flat(X)	$\frac{da}{dN} = 2.890 * 10^{-11} * \Delta K^{2.379}$
CHT Edge(Y)	$\frac{da}{dN} = 2.986 * 10^{-13} * \Delta K^{3.926}$
CHT Vertical(Z)	$\frac{da}{dN} = 8.977 * 10^{-12} * \Delta K^{2.805}$
MHT Flat(X)	$\frac{da}{dN} = 1.107 * 10^{-11} * \Delta K^{2.577}$
MHT Edge(Y)	$\frac{da}{dN} = 3.339 * 10^{-10} * \Delta K^{1.468}$
MHT Vertical(Z)	$\frac{da}{dN} = 6.958 * 10^{-11} * \Delta K^{1.968}$

4.4.2 Effects on Anisotropy

One desired effect of the MHT is the reduction of anisotropy between specimen build orientations. Anisotropic materials complicate the design process by requiring designers to predict how peak loads will be applied to a structure and in many cases require design to the worst case scenario requiring more material to be added increasing cost and weight while decreasing performance. In some cases this may make design of a part completely in-feasible with the chosen material. In materials manufactured by LPBF the anisotropy present is the result of a columnar microstructure that aligns in the build direction. The columnar grains create different material response when loaded in line with the columnar grains than when loaded across the grains. Flat(X) and Vertical(Z) build specimens are loaded across the columnar grains but oriented 90°from each other. Edge(Y) specimens are loaded in line with the columnar direction. Figure 4.16 compares the differences between each of the specimen build orientations for each of the heat treatments. Dashed lines in these plots represent a 95% confidence band around the mean of the respective specimen build orientations. CHT specimens show the greatest degree of anisotropy of the three heat treatments with fatigue crack growth life differences between 1.5 and 2.5 times different based on specimen build orientation. Significant difference is seen between all three of the specimen build orientations for CHT specimens. AB specimens also show significant difference between the three specimen build orientations but of much less magnitude than the CHT specimens, with fatigue crack growth lives only 1.1 - 1.3 times different. Tight confidence bands also indicate consistent performance between all specimens in a given specimen build orientation for AB specimens. This behavior is reflected in Table A.5 where AB specimens show the smallest difference between specimen build orientations. MHT specimens show some isotropic behavior between the Edge(Y) and Vertical(Z) specimen build orientations. These same directions display much wider confidence bands than the Flat(X) specimen build orientation allowing a significant difference to be noted between the Flat(X) and the other two specimen build orientations. The MHT is not entirely successful in removing anisotropic behavior between the different specimen build orientations and shows fatigue crack growth lives 1.3 - 1.9 times different between specimen build orientations.

Differences in the performance of the three specimen build orientations can possibly be linked to features of the building process. In Flat(X) and Vertical(Z) specimens the crack front must advance through the different layers in the build. Edge(Y) build specimens experience the crack front moving parallel with the build layers and potentially allowing crack propagation between these layers. Specimens subjected to the CHT have an increased degree of anisotropy, compared to AB specimens. This corresponds to the microstructural differences between the CHT condition and the MHT condition. The MHT creates a large grained microstructure that is consistent when examined from any angle. Additionally this heat treatment provides even dispersion of γ" precipitates in the microstructure. The columnar grains in the CHT specimens naturally correspond to a higher degree of anisotropy. Additionally the growth of γ" precipitates clustered on the long grain boundaries apply additional strain to the matrix driving further directional effects. The less predictable results associated with the MHT and CHT warrant further study.

4.4.3 Fatigue Crack Growth Rate Surfaces

FCGR specimen fracture surfaces displayed many similar characteristics to FT specimens. In the final fracture regions the same evidence of the layered building process exists as in the FT specimens. The most notable difference between the fracture surfaces of different heat treatments was the visible larger grain size in the MHT specimens, evidenced by the large bright regions. The difference between these two fracture surfaces can be seen in Figures 4.17-4.19. This grain size increase is one of the desired effects of the modification to the standard heat treatment for IN718. The MHT specimens have a much rougher fatigue surface than the AB and CHT specimens. This may be a result of intergranular fracture with a larger grain structure leading to higher peaks and lower valleys than in the small grained AB and CHT fatigue surfaces. CHT specimens show very similar fracture surfaces to the AB specimens. These specimens exhibit a very flat fatigue surface and layering effects corresponding with the specimen build orientation are visible as well. As can be seen in Table 4.4, the MHT specimens show a much higher degree of surface roughness than the AB and CHT specimens. These differences correlated directly with visual observations of the surface. This is another effect of the grain growth that is seen when the MHT is applied. In the fatigue growth region of the MHT specimens the evidence of specimen build orientation is absent and no distinction can be made between the specimen build orientations based on these regions. In the region of final fracture of the MHT specimens, some of the layering effects previously described are present. Specimens that underwent the CHT or remained in the AB condition show clear evidence of specimen build orientation in the fatigue region.

These specimens can easily be assigned by their specimen build orientation after a cursory visual inspection. This is more evidence that the MHT fulfills its purpose of removing the anisotropy associated with specimen build orientation. Topographic maps of the fatigue fracture surface can be seen in Figure 4.20. These images illustrate the smooth fracture surfaces associated with the AB and CHT specimens and the coarse surface seen in the MHT specimens. This effect corresponds to the increase in grain size seen in the MHT specimens and creates a much longer crack path for the same amount of linear travel. The layering effect, while not visible in the fracture region due to the large size of the surface features, is present in the final failure region even after MHT and warrants further study.

Table 4.4. Fatigue Crack Growth Roughness Averages, MHT specimens display the highest roughness values which correspond with visual observations

Specimen	**Fracture Sa μm**
AB Flat(X) Avg	19.794
AB Edge(Y) Avg	11.193
AB Vertical(Z) Avg	14.315
AB Avg	**15.101**
MHT Flat(X) Avg	38.427
MHT Edge(Y) Avg	38.117
MHT Vertical(Z) Avg	32.303
MHT Avg	**36.282**
CHT Flat(X) Avg	23.5124
CHT Edge(Y) Avg	11.1928
CHT Vertical(Z) Avg	13.1816
CHT Avg	**15.962**

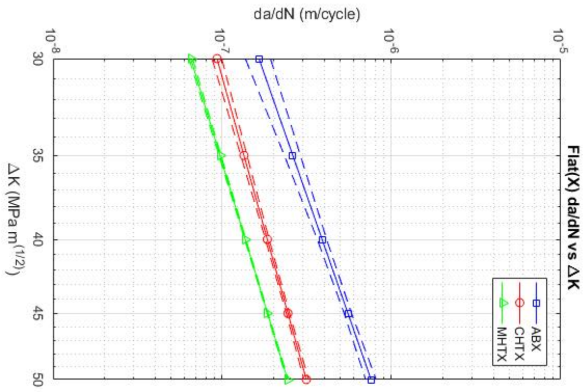

(a) Flat(X): AB specimens show the highest FCGR. The CHT shows slightly higher FCGR than the MHT.

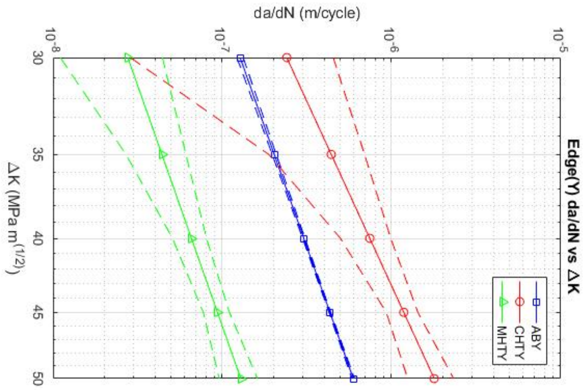

(b) Edge(Y): The CHT shows the highest overall FCGR in the Edge(Y) specimen build orientation. In this build orientation AB specimens show a lower growth rate than CHT specimens.

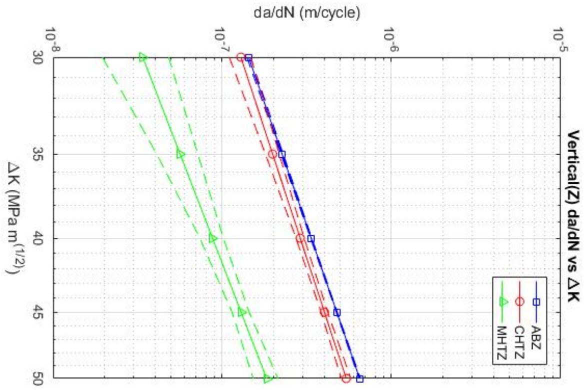

(c) Vertical(Z): AB specimens show the highest FCGR. CHT growth rates are slightly lower than AB rates.

Figure 4.14. Power Law Fit Results in the range of ΔK between 30 and 50 MPa$\sqrt{m}$. Comparisons between specimen build orientations show lower FCGR for MHT specimens in all cases. Dashed lines indicated a 95% confidence band around the power law fit.

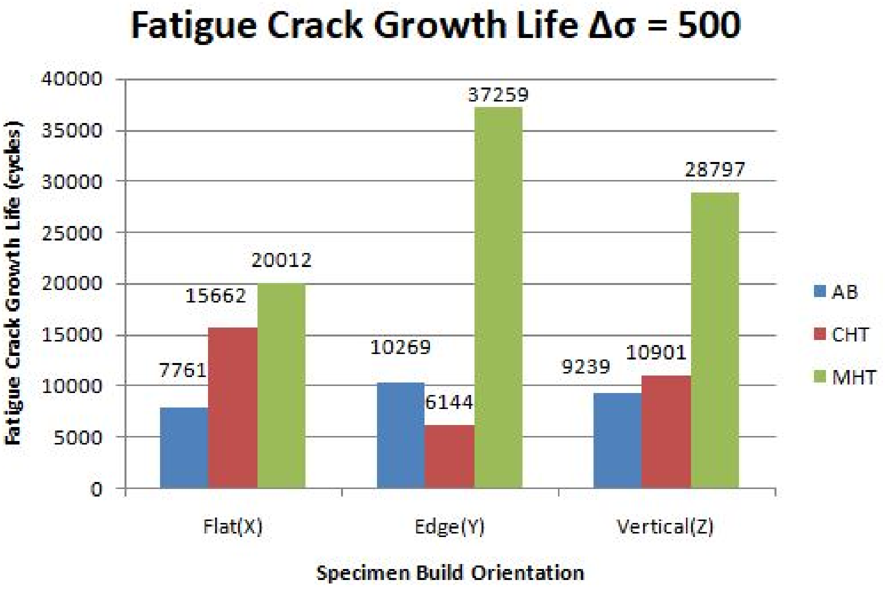

Figure 4.15. Fatigue Crack Growth Lives with an initial crack length of 0.6 mm, final crack length of 3.5 mm, and applied stress range of 500 MPa. MHT specimens show greatly increased crack growth life in all specimen build orientations.

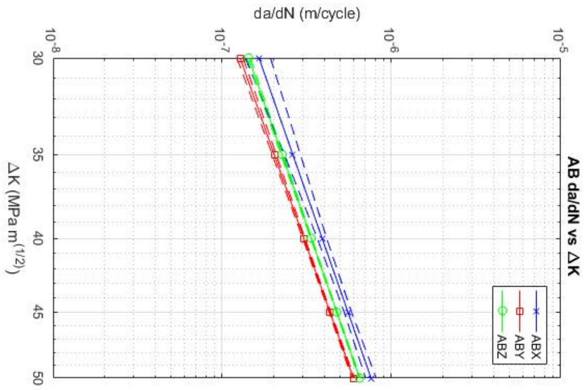

(a) AB: All specimen build orientations show similar FCGR's but remain significantly different

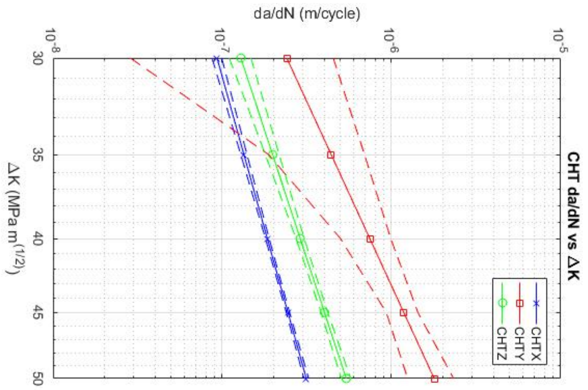

(b) CHT: Edge(Y) specimen build orientation show the highest growth rate with wide scatter at the lower end of the stress intensity range.

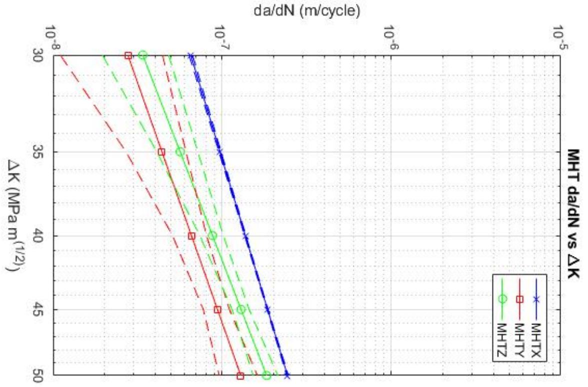

(c) MHT: Some removal of anisotropy is shown between the Edge(Y) and Vertical(Z) directions. Flat(X) builds show a tight confidence band and the highest growth rates for this heat treatment.

Figure 4.16. Power Law Fit Results in the range of ΔK between 30 and 50 MPa$\sqrt{m}$. Dashed lines indicated a 95% confidence band around the power law fit.

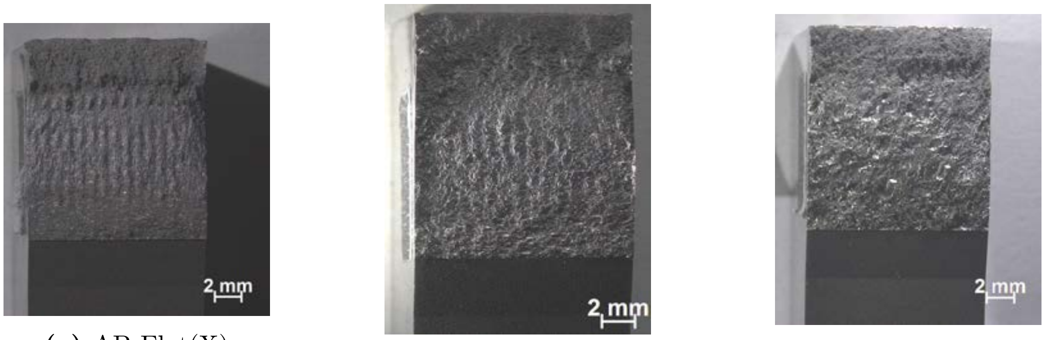

(a) AB Flat(X) **(b)** CHT Flat(X) **(c)** MHT Flat(X)

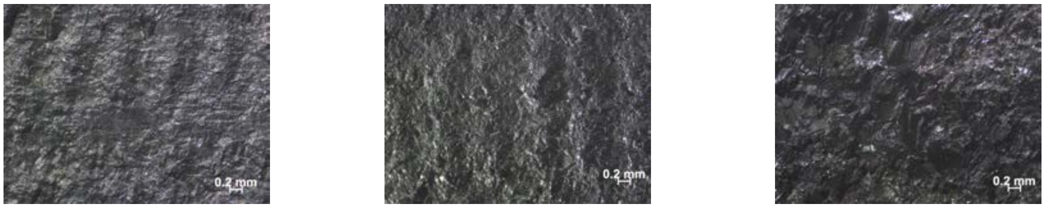

(d) AB Flat(X) **(e)** CHT Flat(X) **(f)** MHT Flat(X)

Figure 4.17. Comparison of Flat(X) build fatigue surfaces. Evidence of specimen build orientation is present in the AB and CHT specimens and absent in the MHT specimen.

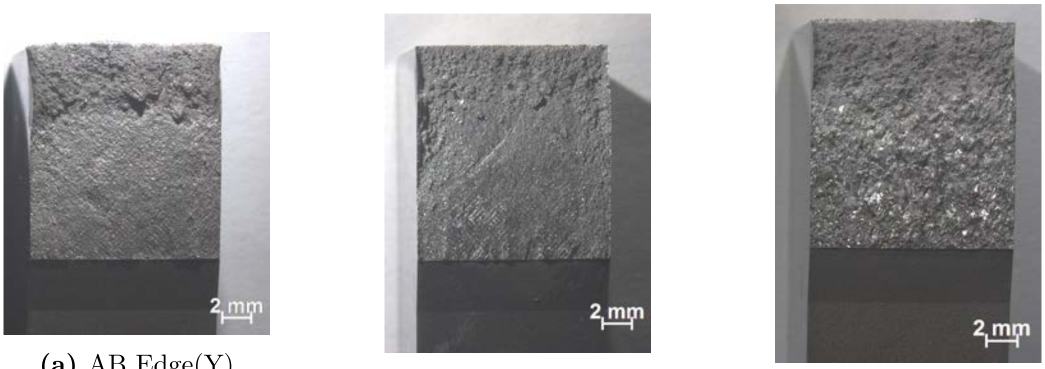

(a) AB Edge(Y) **(b)** CHT Edge(Y) **(c)** MHT Edge(Y)

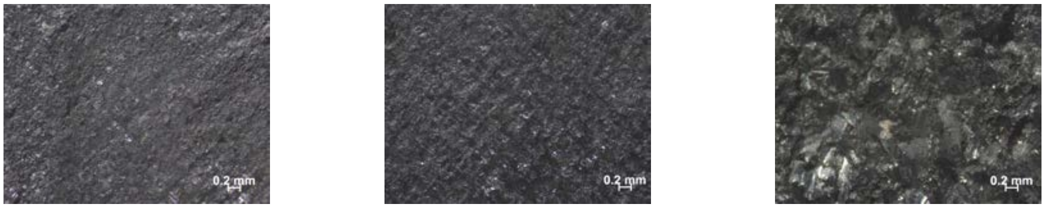

(d) AB Edge(Y) **(e)** CHT Edge(Y) **(f)** MHT Edge(Y)

Figure 4.18. Comparison of Edge(Y) build fatigue surfaces. Evidence of specimen build orientation is present in the AB and CHT specimens and absent in the MHT specimen.

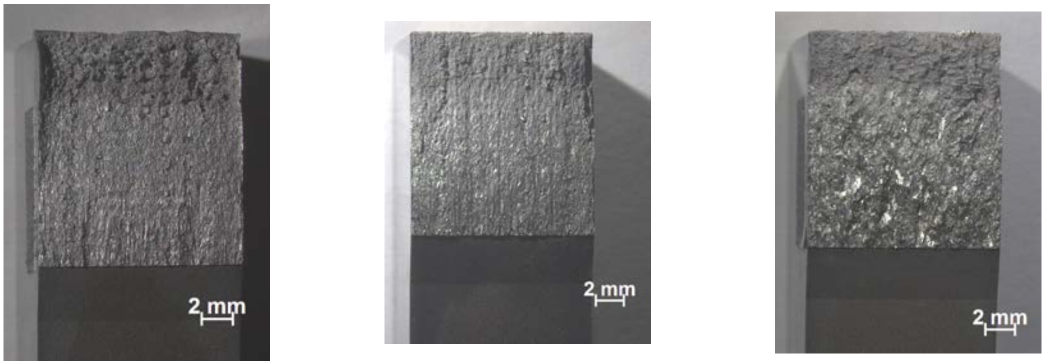

(a) AB Vertical(Z) **(b)** CHT Vertical(Z) **(c)** MHT Vertical(Z)

(d) AB Vertical(Z) **(e)** CHT Vertical(Z) **(f)** MHT Vertical(Z)

Figure 4.19. Comparison of Vertical(Z) build fatigue surfaces. Evidence of specimen build orientation is present in the AB and CHT specimens and absent in the MHT specimen.

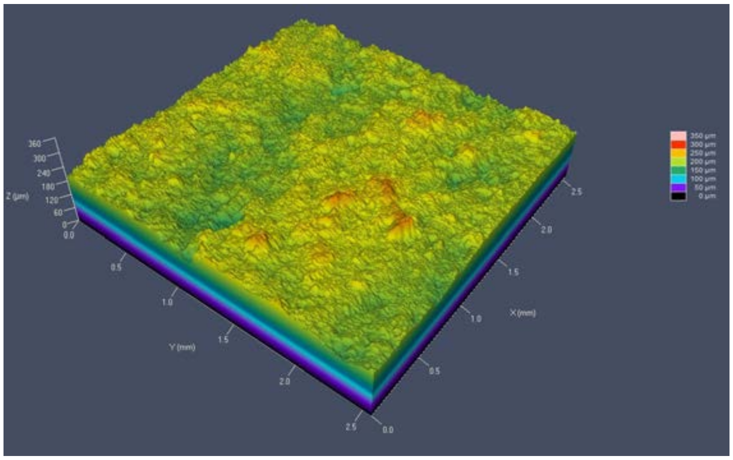

(a) AB fatigue surface showing small peaks and valleys.

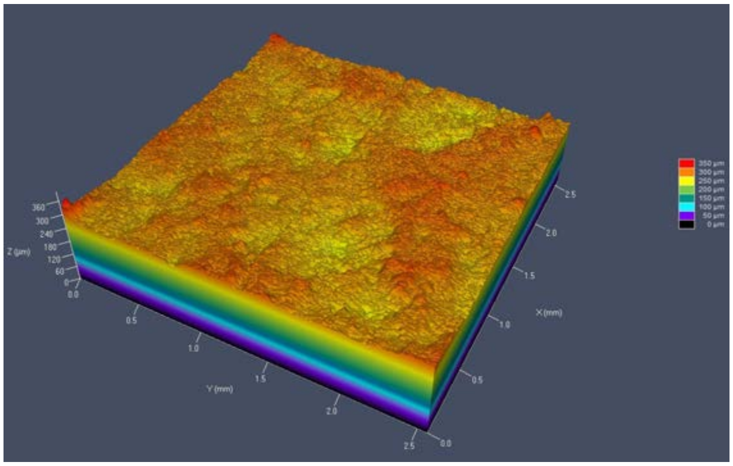

(b) CHT fatigue surface showing similar roughness to the AB surface.

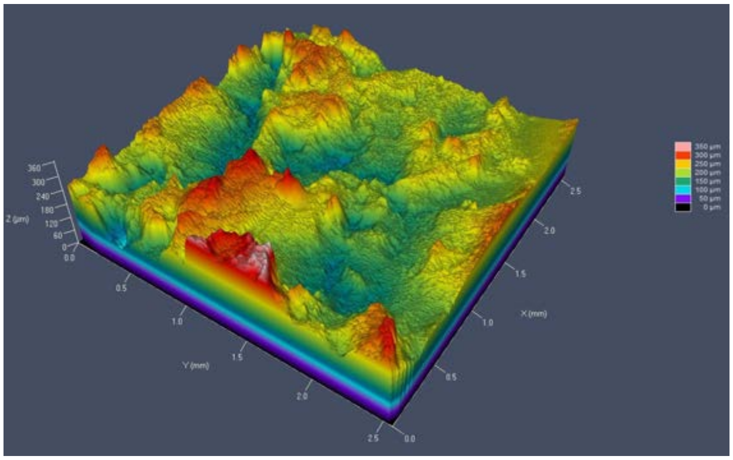

(c) MHT fatigue surface showing significantly increased peak and valley differences.

Figure 4.20. Surface roughness maps of FCGR fracture surfaces. Much greater surface roughness values were recorded for MHT specimens, corresponding to the increase in grain size.

4.5 Chapter 4 Summary

The data collected in this thesis indicates that a modification to the standard heat treatment for IN718 can reduce the FCGR in specimens manufactured by LPBF. A total of 45 C(T) specimens were tested in constant amplitude fatigue loading and 30 specimens were tested in tension under fracture toughness evaluation criteria. The data from fracture toughness tests was used to calculate J_{IC} and K_{JIC} values for the AB and MHT conditions but extensive plasticity and crack front curvature led to violations of the validity requirements in ASTM E1820-17a and meaningful conclusions were unable to be obtained. Further study of FT in this material should be conducted including production of specimens with sufficient thickness to achieve true K_{IC} values. Fatigue testing showed that application of the MHT reduced the FCGR for all specimen build orientations. Application of the CHT increased FCGR in the Edge(Y) specimen build orientation and lowered it for the Flat(X) and Vertical(Z) specimen build orientations compared to the AB condition and increased the degree of anisotropy related to specimen build orientation. MHT specimens were also much more resistant to initiating a fatigue crack requiring approximately 3 - 4 times more cycles than the AB and CHT specimens to grow the appropriate length precrack. Fatigue crack growth lives were 2.6 - 3.6 times greater in AB specimens than in MHT and 1.3 - 6.0 times greater in CHT specimens than in MHT.

Fracture surface evaluations were conducted on both FT and FCGR specimens. A key feature that was present after both experiments was visible evidence of the specimen build orientation. In the Flat(X) and Vertical(Z) specimen build orientations this manifested as a layered structure in the fracture surface that corresponded to layer stacking in the build direction. In the Edge(Y) direction the fracture surface showed evidence of the scan pattern of the laser. Both of these results may indicate that there is incomplete fusion between the layers during the manufacturing process and that neither the CHT or the MHT was effective in completely removing this effect. Porosity is also visible in the fracture surfaces and is a known defect associated with production by LPBF. The root cause of these features and how they affect material behavior is unknown and further study should be conducted.

The results of this study show that the MHT produces desired results for lowering FCGR and that CHT for wrought IN718 is not ideal for use with LPBF IN718. The CHT showed greater FCGR than the MHT condition and produced varying results compared to the AB condition. Fracture surface evaluations revealed that the effects of specimen build orientation remain in the material even following a successful MHT but the exact effect of these features remains unknown. Overall the MHT was successful lowering the FCGR and is a valuable addition to the knowledge base for LPBF IN718.

V. Conclusions and Recommendations

5.1 Summary

The results of this research were the characterization of Fatigue Crack Growth Rate (FCGR)'s for As-Built (AB), Conventional Heat Treatment (CHT), and Modified Heat Treatment (MHT) conditions of Inconel 718 (IN718) manufactured by Laser Powder Bed Fusion (LPBF) and the demonstration of anisotropy in the FCGR between specimen build orientation. Testing methodology was based on the methods laid out in American Society for Testing and Materials E647-15 (ASTM E647-15) and American Society for Testing and Materials E1820-17a (ASTM E1820-17a) and deviations were made to meet the unique needs of this research. Compact Tension (C(T)) specimens were manufactured by LPBF and tested in either constant amplitude fatigue or in tension to fracture. Both of these tests rely on measuring a growing crack and the associated force which was accomplished with a load cell on a hydraulic tension tester and by use of a clip gauge to measure the Crack Mouth Opening Displacement (CMOD). Due to observed peculiarities in the fracture surfaces, a brief examination of these surfaces was conducted utilizing surface roughness measurements. The examination indicates that fracture surfaces exhibited differences based on the specimen build orientation and that the MHT produced a much rougher surface due to grain growth.

The hypothesized questions for this research were:

- What degree of difference does specimen build orientation have on the Fracture Toughness (FT) and FCGR?
- Does a modified heat treatment remove the specimen build orientation dependence of FT and FCGR?

- Does the MHT provide improvements to FT and FCGR in all specimen build orientations?

Regarding the hypothesized questions in this research the following conclusions can be reached:

- specimen build orientation was seen to have effects on the FCGR of all heat treatments tested. AB specimens showed least deviation in fatigue crack growth life between specimen build orientations 1.1 - 1.3 times difference in fatigue crack growth life between specimen build orientations. Specimens subjected to the CHT showed showed the greatest differences of 1.4 - 2.5 times difference in fatigue crack growth life between specimen build orientations. MHT specimens showed a difference in fatigue crack growth life between specimen build orientations of 1.3 - 1.9 times.

- The MHT was not able to remove the anisotropic effects of specimen build orientation. MHT specimens showed anisotropic behavior between specimen build orientations despite the re-crystallization of the grain structure.

- The MHT showed a significant decrease in the FCGR of all specimen build orientations compared to the AB and CHT. The MHT decreases the FCGR of IN718 manufactured by LPBF and increases the number of cycles to initiate a crack. In the initial precracking procedure it was noted that the MHT specimens took approximately 3 - 4 times more cycles than the AB or CHT specimens to grow an appropriately sized precrack. The MHT specimens showed a FCGR that was significantly lower than the AB and CHT specimens. The MHT increased fatigue crack growth life between 1.3 - 6.0 times compared to the CHT. Comparison of the MHT to the AB condition showed an increase in fatigue crack growth life between 2.5 - 3.6 times, dependent on specimen build orientation.

The Flat(X) specimen build orientation was weakest for the MHT but provided a minimum 1.3 times increase in fatigue crack growth life over any of the other AB or CHT condition. This increase in fatigue crack growth life is attributed to the change in grain size and the growth of γ” precipitates during the MHT.

Fracture toughness testing revealed high levels of plasticity during testing requiring that FT tests should be run by the standards of ASTM E1820-17a. Due to extensive crack front curvature, future fracture toughness testing should incorporate side grooves into the design of C(T) specimens as described in ASTM E1820-17a Section 7.5. Fracture toughness values calculated in this research are invalid according to the requirements of ASTM E1820-17a. Observations of CMOD vs Force plots shows that the MHT specimens required more force to reach the displacement maximum of 1.5mm than did AB specimens. This corresponds with tensile data taken in these two conditions and may indicate an improvement in FT with the MHT but no conclusive statements can be made without further valid testing.

In both FT and FCGR, specimen fracture surfaces showed clear evidence of the specimen build orientation. Grain size increases were readily apparent in the MHT fatigue specimens as seen in Figures 4.17 - 4.19 when compared to AB and CHT samples. This corresponded to surface roughness measurements taken of the fracture surfaces where MHT specimens showed much higher values of surface roughness compared to the AB and CHT specimens. A layered texture was visible in the Flat(X) and Vertical(Z) specimens corresponding to the specimen build orientation. Edge(Y) built specimens do not show this feature but evidence of the laser scan pattern can be seen in these fracture surfaces as shown in Sections 4.2.1 and 4.4.3. In the case of the Edge(Y) specimens it appears that the crack propagated between the build layers of the specimen. This indicates that bonding between layers is weaker than the surrounding material. This closely matches the results of tensile tests performed on LPBF IN718[22]. These features seem to indicate that incomplete fusion of layers is present with the printing parameters used. This effect is seen in all three heat treatments.

5.2 Recommendations

As a result of this research several recommendations can be made regarding the use of LPBF IN718:

- Parts that are likely to be stressed in fatigue should be subjected to a heat treatment that encourages re-crystallization and grain growth similar to the MHT studied in this research.
- The CHT for IN718 should not be used for LPBF parts expected to experience fatigue loading due to the increase in anisotropy and increased FCGR compared to the MHT.

These recommendations are subject to further testing, especially at elevated temperatures, and individual design needs.

5.3 Future Work

Additional work is required on this research topic to exhaustively characterize the fracture toughness and fatigue crack growth rate behavior of LPBF IN718. FT results should be compared to the results of the conventional IN718 heat treatment in American Society for Testing and Materials B637 (ASTM B637). While these results set a baseline for the fatigue and fracture properties of Additive Manufacturing (AM) IN718, the real value of IN718 is in its high temperature capabilities. Utilizing the conclusions from this study with respect to the strongest combination of specimen build orientation and heat treatment, further testing should be conducted at elevated temperatures up to the alloy's service ceiling of 650°C. The findings of this research should be able to narrow the scope of high temperature research by removing the CHT from consideration. The MHT was not seen to remove as much anisotropy as had been desired. Further testing of this and similar re-crystallization heat treatments should be performed to determine if isotropy and more consistent results can be produced. Additional work in the fatigue field should be performed to establish a value for $K_{Threshold}$, the minimum stress intensity factor to generate crack growth. Observations of the $\frac{da}{dN}$ vs ΔK curves indicate that $K_{Threshold}$ is likely to occur below 10 MPa$\sqrt{m}$ for AB and CHT specimens and slightly above 10 MPa$\sqrt{m}$ for MHT specimens. Investigation of this parameter may shed more light on anisotropy between specimen build orientations. Further FCGR testing should also be conducted at different stress ratios (R = 0.05, 0.5, 0.75) to help in building an effective material model for use in predictive modeling software. Fracture toughness specimens with a minimum ligament of 76 mm should meet the requirements of Section 7.1.3 in American Society for Testing and Materials E399-17 (ASTM E399-17) to achieve true K_{IC} values. These tests should be conducted at room and elevated temperature to complement the K_{JIC} and J_{IC} values from this research. Also worthy of further investigation is a detailed fracture surface evaluation. The evidence of specimen build orientation in the fracture surfaces warrants investigation to determine what effect the layering causes. If this layering is determined to be detrimental then study of the effect of printing parameters and post processing should be conducted as well to determine methods to mitigate this effect. Implementation of the proposed research would form a more complete understanding of the fracture and fatigue response of IN718 manufactured by LPBF. Completing this body of work is necessary to allow for understanding and acceptability of LPBF as a manufacturing method of IN718.

Appendix A. Tables and Graphs

Table A.1. **Fracture Toughness Specimen Dimensions**

Specimen	W (mm)	B (mm)	notch (mm)	precrack (mm)	ao (mm)
AB Flat(X) 1	25.48	12.26	11.27	1.42	12.69
AB Flat(X) 2	25.32	12.21	11.41	1.44	12.85
AB Flat(X) 3	25.52	12.61	11.34	1.78	13.12
AB Flat(X) 4	25.45	12.21	11.32	1.59	12.91
AB Flat(X) 5	25.43	12.26	11.42	1.45	12.93
AB Flat(X) Avg	**25.44**	**12.31**	**11.35**	**1.53**	**12.90**
AB Edge(Y) 1	25.62	12.38	11.28	1.97	13.25
AB Edge(Y) 2	25.52	12.57	11.27	1.93	13.22
AB Edge(Y) 3	25.43	12.5	11.38	1.27	12.65
AB Edge(Y) 4	25.67	12.42	11.48	1.48	12.96
AB Edge(Y) 5	25.43	12.59	11.37	1.29	12.66
AB Edge(Y) Avg	**25.53**	**12.49**	**11.36**	**1.59**	**12.95**
AB Vertical(Z) 1	25.57	12.34	11.31	1.50	12.81
AB Vertical(Z) 2	25.5	12.33	11.26	1.69	12.95
AB Vertical(Z) 3	25.45	12.46	11.39	1.82	13.21
AB Vertical(Z) 4	25.55	12.39	11.49	1.32	12.81
AB Vertical(Z) 5	25.41	12.4	11.32	1.27	12.59
AB Vertical(Z) Avg	**25.50**	**12.38**	**11.35**	**1.52**	**12.87**
MHT Flat(X) 1	25.39	12.34	11.41	1.41	12.82
MHT Flat(X) 2	25.44	12.3	11.39	1.30	12.69
MHT Flat(X) 3	25.49	12.36	11.38	1.28	12.66
MHT Flat(X) 4	25.41	12.22	11.23	1.22	12.45
MHT Flat(X) 5	25.38	12.64	11.25	1.42	12.67
MHT Flat(X) Avg	**25.42**	**12.37**	**11.33**	**1.33**	**12.66**
MHT Edge(Y) 1	25.41	12.66	11.31	1.28	12.59
MHT Edge(Y) 2	25.45	12.66	11.32	1.46	12.78
MHT Edge(Y) 3	25.46	12.67	11.34	1.33	12.67
MHT Edge(Y) 4	25.38	12.64	11.4	1.17	12.57
MHT Edge(Y) 5	25.42	12.66	11.39	1.20	12.59
MHT Edge(Y) Avg	**25.42**	**12.66**	**11.35**	**1.29**	**12.64**
MHT Vertical(Z) 1	25.41	12.67	11.31	1.46	12.77
MHT Vertical(Z) 2	25.37	12.67	11.41	1.20	12.61
MHT Vertical(Z) 3	25.48	12.66	11.47	1.28	12.75
MHT Vertical(Z) 4	25.27	12.67	11.22	1.27	12.49
MHT Vertical(Z) 5	25.17	12.67	11.38	1.37	12.75
MHT Vertical(Z) Avg	**25.34**	**12.67**	**11.36**	**1.3162**	**12.67**

Table A.2. Specimens with Cycles to Failure *Force drop **Excessive precrack growth

Specimen	W (mm)	precrack (mm)	b_o (mm)	Cycles to Failure
AB Flat(X) 1	25.54	1.29	12.80	173463
AB Flat(X) 2	25.6	2.10	12.03	225488
AB Flat(X) 3	25.45	2.10	12.09	196890
AB Flat(X) 4	25.45	2.04	12.06	184421
AB Flat(X) 5	25.42	2.11	12.11	193572
AB Edge(Y) 1	25.55	2.13	11.95	124711
AB Edge(Y) 2	25.51	2.24	11.94	124542
AB Edge(Y) 3	25.43	2.20	11.91	111034
AB Edge(Y) 4	25.45	2.05	12.09	133210
AB Edge(Y) 5	25.39	2.09	12.06	123720
AB Vertical(Z) 1	25.48	2.05	12.09	124287
AB Vertical(Z) 2	25.48	2.17	12.02	130215
AB Vertical(Z) 3	25.44	2.09	12.08	122060
AB Vertical(Z) 4	25.49	2.08	12.06	146810
AB Vertical(Z) 5	25.47	2.24	11.88	114488
MHT Flat(X) 1	25.38	2.04	12.07	568393
MHT Flat(X) 2	25.37	2.20	11.90	477412
MHT Flat(X) 3	25.52	2.05	12.00	463549
MHT Flat(X) 4	25.45	2.05	12.00	593807
MHT Flat(X) 5	25.44	2.05	12.01	547136
MHT Edge(Y) 1	25.47	2.11	12.01	426621
MHT Edge(Y) 2	25.41	2.05	12.08	302568
MHT Edge(Y) 3	25.45	2.64	11.44	272487
MHT Edge(Y) 4	25.45	2.04	12.02	510400
MHT Edge(Y) 5	25.39	2.31	11.78	310659
MHT Vertical(Z) 1	25.37	2.05	12.12	660789
MHT Vertical(Z) 2	25.5	2.04	12.09	721668
MHT Vertical(Z) 3*	25.48	2.05	12.03	1030942
MHT Vertical(Z) 4	25.46	2.07	12.05	502896
MHT Vertical(Z) 5	25.47	2.96	11.17	321497
CHT Flat(X) 1	25.38	2.54	11.36	145722
CHT Flat(X) 2	25.5	2.05	11.98	243691
CHT Flat(X) 3	25.38	2.04	12.00	281316
CHT Flat(X) 4	25.51	2.12	11.94	189715
CHT Flat(X) 5	25.39	2.06	11.92	232723
CHT Edge(Y) 1	25.29	2.35	11.59	82657
CHT Edge(Y) 2**	25.36	4.14	9.86	45685
CHT Edge(Y) 3	25.37	2.04	12.03	102011
CHT Edge(Y) 4	25.4	2.06	12.01	92500
CHT Edge(Y) 5	25.3	2.05	11.97	86229
CHT Vertical(Z) 1	25.37	2.49	11.65	119600
CHT Vertical(Z) 2	25.31	3.27	10.69	94649
CHT Vertical(Z) 3	25.37	2.17	11.86	156201
CHT Vertical(Z) 4	25.37	2.09	11.97	160772
CHT Vertical(Z) 5	25.51	2.67	11.44	113229

Table A.3. Fatigue Crack Growth Rate Specimen Dimensions

Specimen	W (mm)	B (mm)	notch (mm)	precrack (mm)	ao (mm)
AB Flat(X) 1	25.54	12.35	11.45	1.29	12.74
AB Flat(X) 2	25.6	12.63	11.47	2.10	13.57
AB Flat(X) 3	25.45	12.61	11.27	2.10	13.37
AB Flat(X) 4	25.45	12.67	11.35	2.04	13.39
AB Flat(X) 5	25.42	12.64	11.20	2.11	13.31
AB Flat(X) Avg	**25.49**	**12.58**	**11.35**	**1.93**	**13.28**
AB Edge(Y) 1	25.55	12.64	11.47	2.13	13.60
AB Edge(Y) 2	25.51	12.65	11.33	2.24	13.57
AB Edge(Y) 3	25.43	12.65	11.32	2.20	13.52
AB Edge(Y) 4	25.45	12.66	11.31	2.05	13.36
AB Edge(Y) 5	25.39	12.62	11.24	2.09	13.33
AB Edge(Y) Avg	**25.47**	**12.64**	**11.33**	**2.14**	**13.47**
AB Vertical(Z) 1	25.48	12.63	11.34	2.05	13.39
AB Vertical(Z) 2	25.48	12.6	11.3	2.17	13.47
AB Vertical(Z) 3	25.44	12.63	11.27	2.09	13.36
AB Vertical(Z) 4	25.49	12.62	11.35	2.08	13.43
AB Vertical(Z) 5	25.47	12.58	11.35	2.24	13.59
AB Vertical(Z) Avg	**25.47**	**12.61**	**11.32**	**2.13**	**13.45**
MHT Flat(X) 1	25.38	12.63	11.27	2.04	13.31
MHT Flat(X) 2	25.37	12.63	11.28	2.20	13.48
MHT Flat(X) 3	25.52	12.63	11.47	2.05	13.52
MHT Flat(X) 4	25.45	12.63	11.40	2.05	13.45
MHT Flat(X) 5	25.44	12.63	11.38	2.05	13.43
MHT Flat(X) Avg	**25.43**	**12.63**	**11.36**	**2.08**	**13.44**
MHT Edge(Y) 1	25.47	12.64	11.44	2.11	13.46
MHT Edge(Y) 2	25.41	12.62	11.28	2.05	13.33
MHT Edge(Y) 3	25.45	12.64	11.37	2.64	14.01
MHT Edge(Y) 4	25.45	12.63	11.39	2.04	13.43
MHT Edge(Y) 5	25.39	12.62	11.30	2.31	13.61
MHT Edge(Y) Avg	**25.43**	**12.63**	**11.36**	**2.23**	**13.57**
MHT Vertical(Z) 1	25.37	12.63	11.20	2.05	13.25
MHT Vertical(Z) 2	25.5	12.63	11.37	2.04	13.41
MHT Vertical(Z) 3	25.48	12.63	11.40	2.05	13.45
MHT Vertical(Z) 4	25.46	12.63	11.34	2.07	13.41
MHT Vertical(Z) 5	25.47	12.62	11.34	2.96	14.30
MHT Vertical(Z) Avg	**25.46**	**12.63**	**11.33**	**2.23**	**13.56**
CHT Flat(X) 1	25.38	12.65	11.48	2.54	14.02
CHT Flat(X) 2	25.5	12.65	11.47	2.05	13.52
CHT Flat(X) 3	25.38	12.62	11.34	2.04	13.38
CHT Flat(X) 4	25.51	12.66	11.46	2.11	13.57
CHT Flat(X) 5	25.39	12.66	11.41	2.06	13.47
CHT Flat(X) Avg	**25.43**	**12.65**	**11.43**	**2.16**	**13.59**
CHT Edge(Y) 1	25.29	12.65	11.35	2.35	13.70
CHT Edge(Y) 2	25.36	12.65	11.36	4.14	15.50
CHT Edge(Y) 3	25.37	12.67	11.30	2.04	13.34
CHT Edge(Y) 4	25.4	12.67	11.33	2.06	13.39
CHT Edge(Y) 5	25.3	12.67	11.28	2.05	13.33
CHT Edge(Y) Avg	**25.34**	**12.66**	**11.32**	**2.53**	**13.85**
CHT Vertical(Z) 1	25.37	12.68	11.23	2.49	13.72
CHT Vertical(Z) 2	25.31	12.65	11.35	3.27	14.62
CHT Vertical(Z) 3	25.37	12.66	11.34	2.17	13.51
CHT Vertical(Z) 4	25.37	12.67	11.31	2.09	13.40
CHT Vertical(Z) 5	25.51	12.65	11.40	2.67	14.07
CHT Vertical(Z) Avg	**25.39**	**12.66**	**11.33**	**2.54**	**13.86**

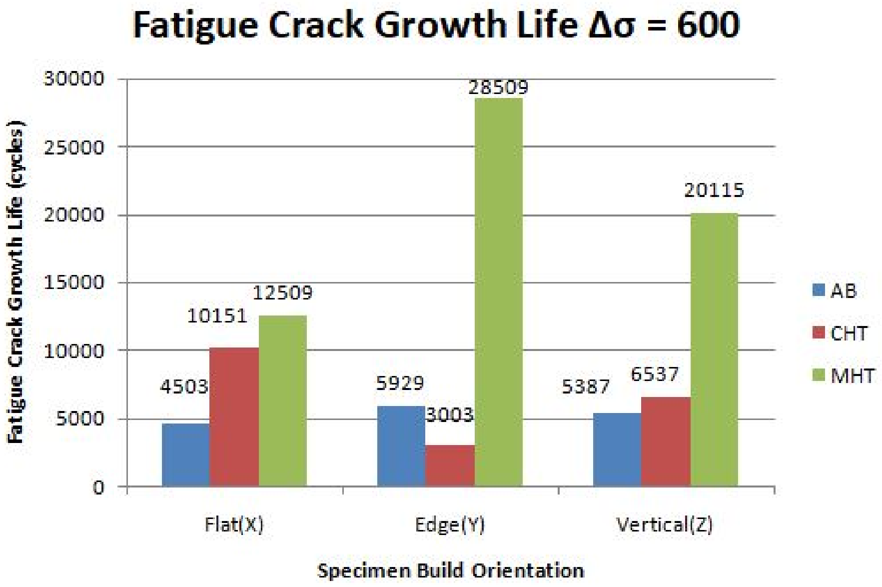

Figure A.1. Fatigue Crack Growth Lives with an initial crack length of 0.6 mm, final crack length of 3.5 mm, and applied stress range of 600 MPa. MHT specimens show greatly increased crack growth life in all build directions.

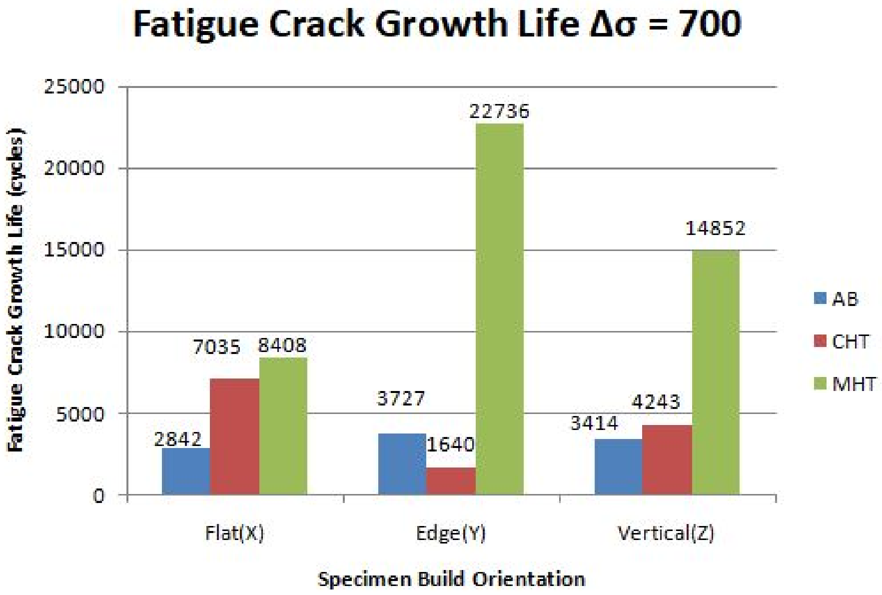

Figure A.2. Fatigue Crack Growth Lives with an initial crack length of 0.6 mm, final crack length of 3.5 mm, and applied stress range of 700 MPa. MHT specimens show greatly increased crack growth life in all build directions.

Table A.4. Comparison of heat treatment effect on fatigue crack growth life for varying stress levels with an initial crack length of 0.6 mm and a final crack length of 3.5 mm. MHT specimens show greater fatigue crack growth life in all build directions as evidenced by the ratios comparing crack growth lives.

	$\Delta\sigma$ (MPa)	ΔK (MPa $\sqrt{m}$)	Nf (cycles)		Ratio of FCGR Life
AB Flat(X)	500.00	24-58	7761	**MHT-Flat(X)/AB-Flat(X)**	2.58
AB Edge(Y)	500.00	24-58	10269	**MHT-Edge(Y)/AB-Edge(Y)**	3.63
AB Vertical(Z)	500.00	24-58	9239	**MHT-Vertical(Z)/AB-Vertical(Z)**	3.12
CHT Flat(X)	500.00	24-58	15662	**MHT-Flat(X)/CHT-Flat(X)**	1.28
CHT Edge(Y)	500.00	24-58	6144	**MHT-Edge(Y)]/CHT-Edge(Y)**	6.06
CHT Vertical(Z)	500.00	24-58	10901	**MHT-Vertical(Z)/CHT-Vertical(Z)**	2.64
MHT Flat(X)	500.00	24-58	20012	**AB-Flat(X)/CHT-Flat(X)**	0.50
MHT Edge(Y)	500.00	24-58	37259	**AB-Edge(Y)/CHT-Edge(Y)**	1.67
MHT Vertical(Z)	500.00	24-58	28797	**AB-Vertical(Z)/CHT-Vertical(Z)**	0.85
	$\Delta\sigma$ (MPa)	**ΔK (MPa $\sqrt{m}$)**	**Nf (cycles)**		**Ratio of FCGR Life**
AB Flat(X)	600.00	29-70	4503	**MHT-Flat(X)/AB-Flat(X)**	2.78
AB Edge(Y)	600.00	29-70	5929	**MHT-Edge(Y)/AB-Edge(Y)**	4.81
AB Vertical(Z)	600.00	29-70	5387	**MHT-Vertical(Z)/AB-Vertical(Z)**	3.73
CHT Flat(X)	600.00	29-70	10151	**MHT-Flat(X)/CHT-Flat(X)**	1.23
CHT Edge(Y)	600.00	29-70	3003	**MHT-Edge(Y)/CHT-Edge(Y)**	9.49
CHT Vertical(Z)	600.00	29-70	6537	**MHT-Vertical(Z)/CHT-Vertical(Z)**	3.08
MHT Flat(X)	600.00	29-70	12509	**AB-Flat(X)/CHT-Flat(X)**	0.44
MHT Edge(Y)	600.00	29-70	28509	**AB-Edge(Y)/CHT-Edge(Y)**	1.97
MHT Vertical(Z)	600.00	29-70	20115	**AB-Vertical(Z)/CHT-Vertical(Z)**	0.82
	$\Delta\sigma$ (MPa)	**ΔK (MPa $\sqrt{m}$)**	**Nf (cycles)**		**Ratio of FCGR Life**
AB Flat(X)	700.00	34-82	2842	**MHT-Flat(X)/AB-Flat(X)**	2.96
AB Edge(Y)	700.00	34-82	3727	**MHT-Edge(Y)/AB-Edge(Y)**	6.10
AB Vertical(Z)	700.00	34-82	3414	**MHT-Vertical(Z)/AB-Vertical(Z)**	4.35
CHT Flat(X)	700.00	34-82	7035	**MHT-Flat(X)/CHT-Flat(X)**	1.20
CHT Edge(Y)	700.00	34-82	1640	**MHT-Edge(Y)/CHT-Edge(Y)**	13.86
CHT Vertical(Z)	700.00	34-82	4243	**MHT-Vertical(Z)/CHT-Vertical(Z)**	3.50
MHT Flat(X)	700.00	34-82	8408	**AB-Flat(X)/CHT-Flat(X)**	0.40
MHT Edge(Y)	700.00	34-82	22736	**AB-Edge(Y)/CHT-Edge(Y)**	2.27
MHT Vertical(Z)	700.00	34-82	14852	**AB-Vertical(Z)/CHT-Vertical(Z)**	0.80

Table A.5. Comparison of build direction effect on fatigue crack growth life for varying stress levels with an initial crack length of 0.6 mm and a final crack length of 3.5 mm. Ratios of the crack growth lives for different build directions are presented.

	$\Delta\sigma$ (MPa)	ΔK (MPa $\sqrt{m}$)	Nf (cycles)		Ratio of FCGR Life
AB Flat(X)	500.00	24-58	7761	**AB-Flat(X)/AB-Edge(Y)**	0.76
AB Edge(Y)	500.00	24-58	10269	**AB-Flat(X)/AB-Vertical(Z)**	0.84
AB Vertical(Z)	500.00	24-58	9239	**AB-Edge(Y)/AB-Vertical(Z)**	1.11
CHT Flat(X)	500.00	24-58	15662	**CHT-Flat(X)/CHT-Edge(Y)**	2.55
CHT Edge(Y)	500.00	24-58	6144	**CHT-Flat(X)/CHT-Vertical(Z)**	1.44
CHT Vertical(Z)	500.00	24-58	10901	**CHT-Edge(Y)/CHT-Vertical(Z)**	0.56
MHT Flat(X)	500.00	24-58	20012	**MHT-Flat(X)/MHT-Edge(Y)**	0.54
MHT Edge(Y)	500.00	24-58	37259	**MHT-Flat(X)/MHT-Vertical(Z)**	0.69
MHT Vertical(Z)	500.00	24-58	28797	**MHT-Edge(Y)/MHT-Vertical(Z)**	1.29
	$\Delta\sigma$ (MPa)	ΔK (MPa $\sqrt{m}$)	Nf (cycles)		Ratio of FCGR Life
AB Flat(X)	600.00	29-70	4503	**AB-Flat(X)/AB-Edge(Y)**	0.76
AB Edge(Y)	600.00	29-70	5929	**AB-Flat(X)/AB-Vertical(Z)**	0.84
AB Vertical(Z)	600.00	29-70	5387	**AB-Edge(Y)/AB-Vertical(Z)**	1.10
CHT Flat(X)	600.00	29-70	10151	**CHT-Flat(X)/CHT-Edge(Y)**	3.38
CHT Edge(Y)	600.00	29-70	3003	**CHT-Flat(X)/CHT-Vertical(Z)**	1.55
CHT Vertical(Z)	600.00	29-70	6537	**CHT-Edge(Y)/CHT-Vertical(Z)**	0.46
MHT Flat(X)	600.00	29-70	12509	**MHT-Flat(X)/MHT-Edge(Y)**	0.44
MHT Edge(Y)	600.00	29-70	28509	**MHT-Flat(X)/MHT-Vertical(Z)**	0.62
MHT Vertical(Z)	600.00	29-70	20115	**MHT-Edge(Y)/MHT-Vertical(Z)**	1.42
	$\Delta\sigma$ (MPa)	ΔK (MPa $\sqrt{m}$)	Nf (cycles)		Ratio of FCGR Life
AB Flat(X)	700.00	34-82	2842	**AB-Flat(X)/AB-Edge(Y)**	0.76
AB Edge(Y)	700.00	34-82	3727	**AB-Flat(X)/AB-Vertical(Z)**	0.83
AB Vertical(Z)	700.00	34-82	3414	**AB-Edge(Y)/AB-Vertical(Z)**	1.09
CHT Flat(X)	700.00	34-82	7035	**CHT-Flat(X)/CHT-Edge(Y)**	4.29
CHT Edge(Y)	700.00	34-82	1640	**CHT-Flat(X)/CHT-Vertical(Z)**	1.66
CHT Vertical(Z)	700.00	34-82	4243	**CHT-Edge(Y)/CHT-Vertical(Z)**	0.39
MHT Flat(X)	700.00	34-82	8408	**MHT-Flat(X)/MHT-Edge(Y)**	0.40
MHT Edge(Y)	700.00	34-82	22736	**MHT-Flat(X)/MHT-Vertical(Z)**	2.27
MHT Vertical(Z)	700.00	34-82	14852	**MHT-Edge(Y)/MHT-Vertical(Z)**	0.80

Table A.6. Fracture Toughness Roughness Measurements

Specimen	Precrack Ra μm	Perpindicular Ra μm	Parallel Ra μm	Precrack Sa μm	Fracture Sa μm
AB Flat(X) 1				65.36	274.1
AB Flat(X) 2	60.45	207.84	475.48	34.22	418.82
AB Flat(X) 3	41.54	153.8	326.88	50.75	268.59
AB Flat(X) 4	92.65	315.15	355.57	84.69	102.14
AB Flat(X) 5	64.87	108.34	317.73	33.11	68.56
AB Flat(X) Avg	64.8775	196.2825	368.915	50.6925	214.5275
AB Edge(Y) 1	112.09	508.47	157.39	166.92	452.07
AB Edge(Y) 2	60.25	398.93	263.81	79.73	301.97
AB Edge(Y) 3	16.73	262.14	148.56	46.67	63.21
AB Edge(Y) 4	22.74	92	204.63	35.02	204.51
AB Edge(Y) 5	51.4	217.94	392.48	140.68	279.4
AB Edge(Y) Avg	52.642	295.896	233.374	93.804	260.232
AB Vertical(Z) 1	16.51	182.18	105.67	68.25	251.93
AB Vertical(Z) 2	47.48	427.87	277.9	90.8	461.45
AB Vertical(Z) 3	33.43	121.89	149.78	27.34	47.08
AB Vertical(Z) 4	10.99	148.04	147.87	53.18	140.36
AB Vertical(Z) 5	17.87	136.12	82.26	36.36	55.53
AB Vertical(Z) Avg	25.256	203.22	152.696	55.186	191.27
MHT Flat(X) 1	35.29	139.18	156.87	52.25	25.48
MHT Flat(X) 2	16.01	286.47	203.74	39.04	353.98
MHT Flat(X) 3	36.85	45.15	79.42	70.41	106.49
MHT Flat(X) 4	24	78.57	756	53.05	635.07
MHT Flat(X) 5	21.84	65.71	424.84	32.21	112.01
MHT Flat(X) Avg	26.798	123.016	324.174	49.392	246.606
MHT Edge(Y) 1	29.28	229.62	299.82	44.87	359.46
MHT Edge(Y) 2	23.26	128.08	220.87	109.05	215.34
MHT Edge(Y) 3	24	206.42	243.51	88.09	259.32
MHT Edge(Y) 4	35.96	202.35	86.97	28.39	154.54
MHT Edge(Y) 5	17.08	120.49	36.49	35.9	169.67
MHT Edge(Y) Avg	25.916	177.392	177.532	61.26	231.666
MHT Vertical(Z) 1	25.98	98.8	69.6	47.78	74.64
MHT Vertical(Z) 2	20.05	176.19	110.31	44.82	333.58
MHT Vertical(Z) 3	20.96	94.07	88.55	52.91	106.43
MHT Vertical(Z) 4	27.56	63.4	80.96	50.93	114.89
MHT Vertical(Z) 5	22.69	211.81	119.52	58.86	308.12
MHT Vertical(Z) Avg	23.448	128.854	93.788	51.06	187.532

Table A.7. Area Surface Roughness Measurments for FCGR Specimen Fracture Surfaces

Specimen	Sa (μm)
AB Flat(X) 1	19.62
AB Flat(X) 2	21.169
AB Flat(X) 3	20.696
AB Flat(X) 4	18.975
AB Flat(X) 5	18.51
AB Flat(X) Avg	19.794
AB Edge(Y) 1	11.674
AB Edge(Y) 2	11.484
AB Edge(Y) 3	14.273
AB Edge(Y) 4	10.882
AB Edge(Y) 5	11.383
AB Edge(Y) Avg	11.1928
AB Vertical(Z) 1	11.966
AB Vertical(Z) 2	15.81
AB Vertical(Z) 3	12.221
AB Vertical(Z) 4	17.449
AB Vertical(Z) 5	14.129
AB Vertical(Z) Avg	14.315
MHT Flat(X) 1	31.418
MHT Flat(X) 2	48.729
MHT Flat(X) 3	41.23
MHT Flat(X) 4	32.187
MHT Flat(X) 5	38.572
MHT Flat(X) Avg	38.4272
MHT Edge(Y) 1	46.236
MHT Edge(Y) 2	26.256
MHT Edge(Y) 3	35.84
MHT Edge(Y) 4	47.655
MHT Edge(Y) 5	34.599
MHT Edge(Y) Avg	38.1172
MHT Vertical(Z) 1	32.444
MHT Vertical(Z) 2	43.994
MHT Vertical(Z) 3	25.752
MHT Vertical(Z) 4	29.632
MHT Vertical(Z) 5	29.691
MHT Vertical(Z) Avg	32.3026
CHT Flat(X) 1	18.528
CHT Flat(X) 2	31.593
CHT Flat(X) 3	30.355
CHT Flat(X) 4	20.758
CHT Flat(X) 5	16.328
CHT Flat(X) Avg	23.5124
CHT Edge(Y) 1	16.766
CHT Edge(Y) 2	9.683
CHT Edge(Y) 3	11.652
CHT Edge(Y) 4	8.642
CHT Edge(Y) 5	9.221
CHT Edge(Y) Avg	11.1928
CHT Vertical(Z) 1	8.717
CHT Vertical(Z) 2	17.031
CHT Vertical(Z) 3	19.783
CHT Vertical(Z) 4	11.17
CHT Vertical(Z) 5	9.207
CHT Vertical(Z) Avg	13.1816

Table A.8. Fracture Toughness Results, *Tested by process in ASTM E399, **Equipment failure no data (Invalid data due to crack front curvature)

Specimen	**JIC** (kJ/m^2)	**KJIC** ($MPa/sqrtm$)
AB Flat(X) 1*	20.59	61.29
AB Flat(X) 2*	26.95	70.12
AB Flat(X) 3*	20.32	60.89
AB Flat(X) 4	6.51	34.46
AB Flat(X) 5	28.59	72.21
AB Flat(X) Avg	20.59	59.79
AB Edge(Y) 1*	14.57	42.53
AB Edge(Y) 2**	—-	—-
AB Edge(Y) 3	3.41	20.57
AB Edge(Y) 4*	3.37	20.45
AB Edge(Y) 5	2.13	16.27
AB Edge(Y) Avg	8.81	31.92
AB Vertical(Z) 1*	21.23	62.23
AB Vertical(Z) 2*	23.30	65.20
AB Vertical(Z) 3	3.05	23.60
AB Vertical(Z) 4	3.34	24.70
AB Vertical(Z) 5	3.68	25.91
AB Vertical(Z) Avg	10.92	40.33
HT Flat(X) 1	3.95	30.91
HT Flat(X) 2	6.13	38.49
HT Flat(X) 3	23.92	76.04
HT Flat(X) 4	4.46	32.84
HT Flat(X) 5	0.05	3.57
HT Flat(X) Avg	7.70	36.37
HT Edge(Y) 1	2.04	15.93
HT Edge(Y) 2	4.16	22.74
HT Edge(Y) 3	1.76	14.78
HT Edge(Y) 4	0.61	8.69
HT Edge(Y) 5	2.25	16.70
HT Edge(Y) Avg	2.16	15.77
HT Vertical(Z) 1	14.07	58.32
HT Vertical(Z) 2	19.10	67.95
HT Vertical(Z) 3	4.31	32.27
HT Vertical(Z) 4	2.09	22.47
HT Vertical(Z) 5	1.52	19.19
HT Vertical(Z) Avg	8.22	40.04

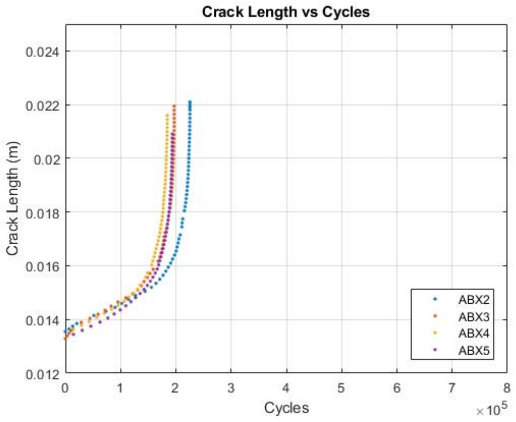

(a) AB

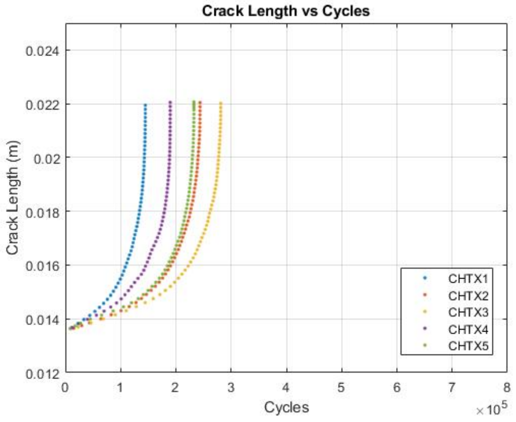

(b) CHT

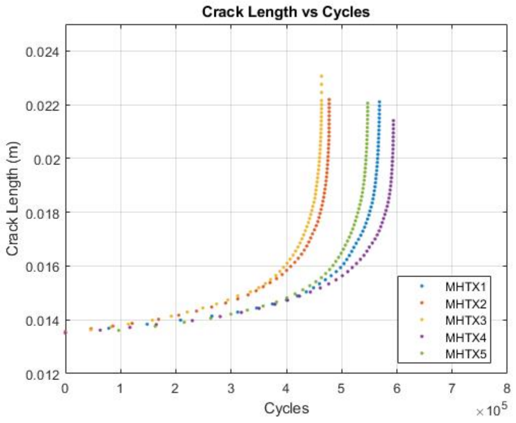

(c) MHT

Figure A.3. Flat Build Orientation Crack Length vs Cycles to Failure, data points shown for a/W > 0.8 but excluded from calculations

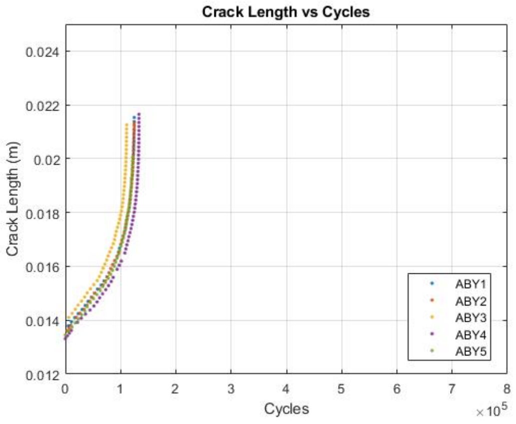

(a) AB

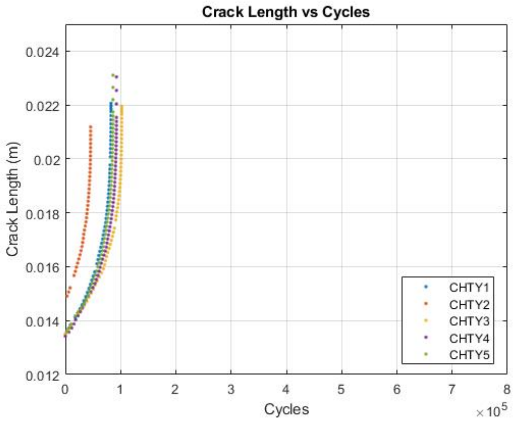

(b) CHT

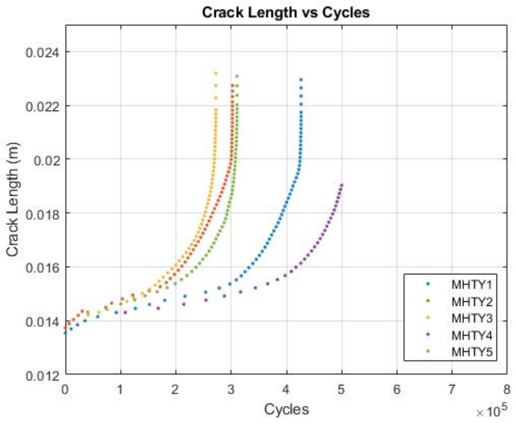

(c) MHT

Figure A.4. Edge Build Orientation Crack Length vs Cycles to Failure, data points shown for a/W > 0.8 but excluded from calculations

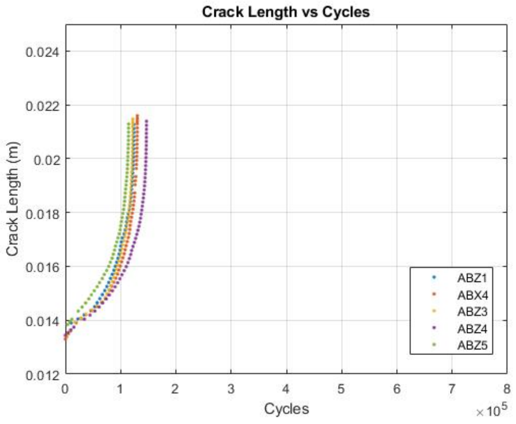

(a) AB

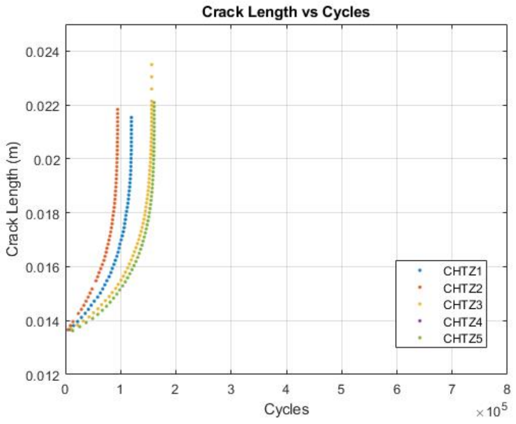

(b) CHT

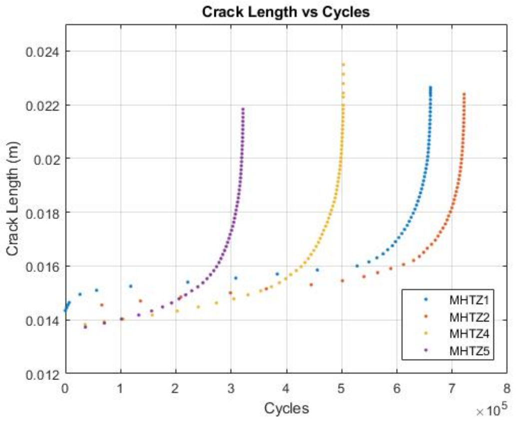

(c) MHT

Figure A.5. Vertical Build Orientation Crack Length vs Cycles to Failure, data points shown for a/W $>$ 0.8 but excluded from calculations

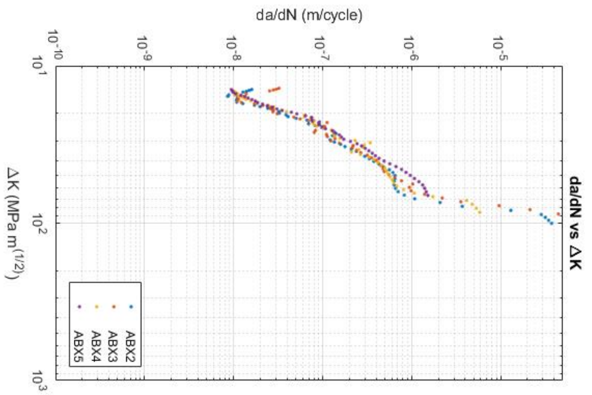

(a) AB

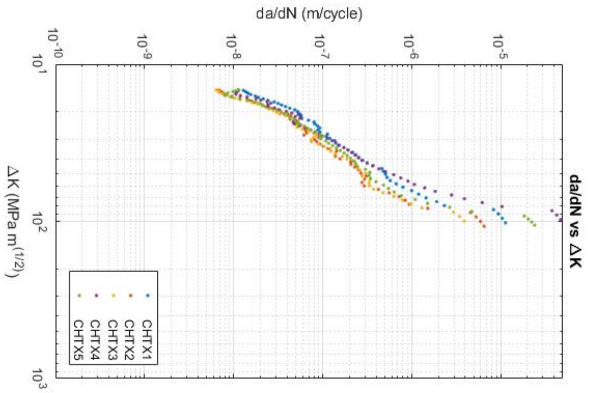

(b) CHT

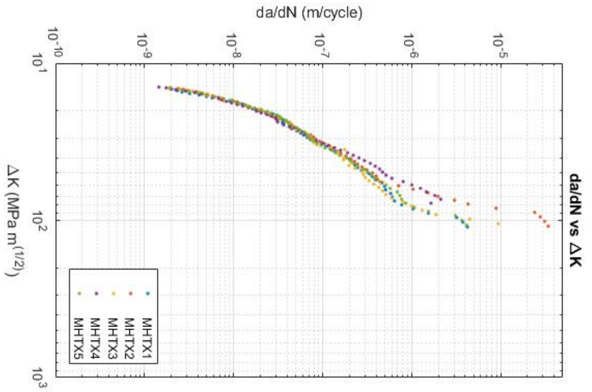

(c) MHT

Figure A.6. Flat Build Orientation da/dN vs ΔK, data points shown for a/W > 0.8 but excluded from calculations

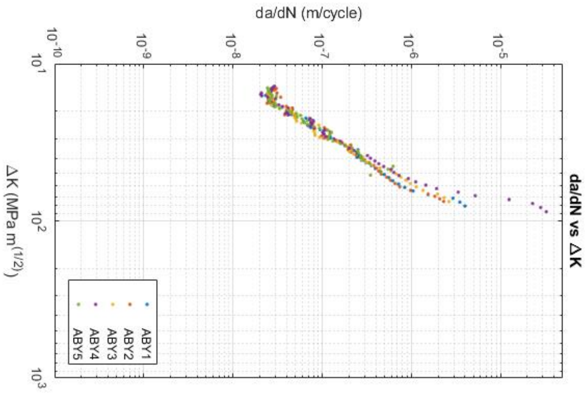

(a) AB

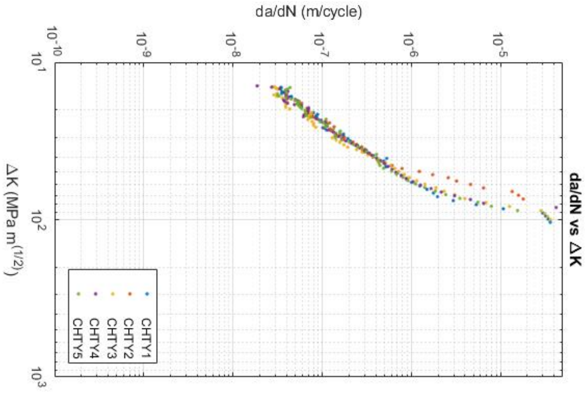

(b) CHT

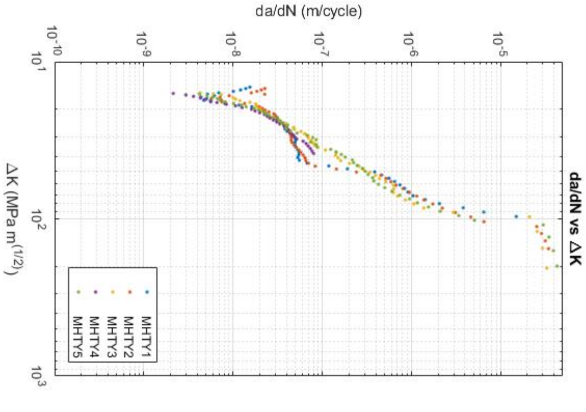

(c) MHT

Figure A.7. Edge Build Orientation da/dN vs ΔK, data points shown for a/W > 0.8 but excluded from calculations

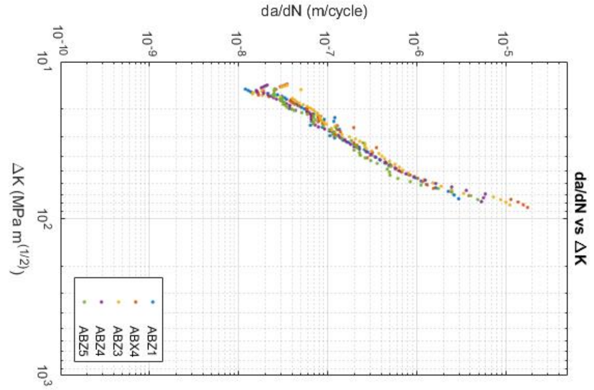

(a) AB

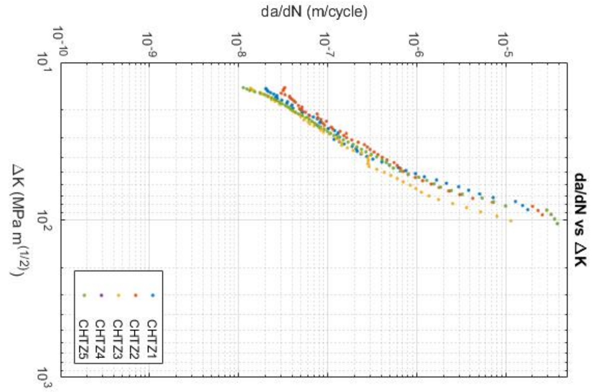

(b) CHT

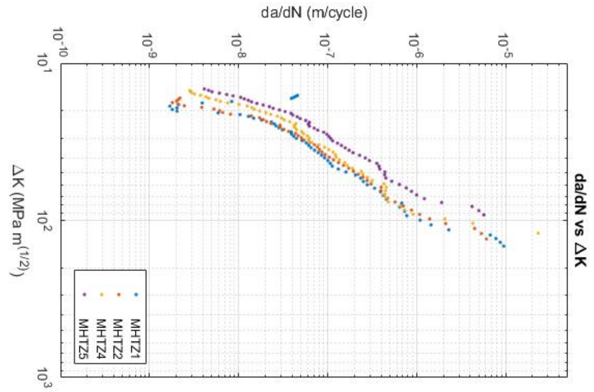

(c) MHT

Figure A.8. Vertical Build Orientation da/dN vs ΔK, data points shown for a/W > 0.8 but excluded from calculations

Appendix B. MATLAB Code

B.1 MATLAB Code for FT Testing

```

clc,clear,close all
% Initial Inputs
%Individual specimen values
W = [.02548 .02532 .02552 .02545 .02543 .02562 .02543 .02552 .02543 ...
    .02557 .02550 .02545 .02555 .02541 .02539 .02544 .02549 .02541 ...
    .02538 .02541 .02545 .02546 .02538 .02542 .02541 .02537 .02548 ...
    .02527 .02517]; %(m) Specimen width from center of loading pins ...
    ASTM 399 A3.5.3
B = [.01226 .01221 .01261 .01221 .01226 .01238 .01242 .01250 .01257 ...
    .01259 .01234 .01233 .01246 .01239 .01240 .01234 .01230 .01236 ...
    .01222 .01264 .01266 .01267 .01264 .01266 .01267 .01267 .01266 ...
    .01267 .01267];%(m) Specimen thickness ASTM 399 A3.5.3
ao = [.012686 .012846 .013119 .012913 .012927 .013250 .012647 ...
    .013219 .012662 .012806 .012948 .013214 .012809 .012594 .012821 ...
    .012693 .012659 .012451 .012665 .012586 .012784 .012673 .012572 ...
    .012585 .012769 .012613 .012751 .012488 .012750];%(m) original ...
    crack size ASTM 1820 3.2.18
v = 0.3;% poisson ratio
E = [1.66*10^11 1.66*10^11 1.66*10^11 1.66*10^11 1.66*10^11 ...
    1.13*10^11 1.13*10^11 1.13*10^11 1.13*10^11 1.66*10^11 ...
    1.66*10^11 1.66*10^11 1.66*10^11 1.66*10^11 204*10^9 204*10^9 ...
    204*10^9 204*10^9 204*10^9 207*10^9 207*10^9 207*10^9 207*10^9 ...
    207*10^9 204*10^9 204*10^9 204*10^9 204*10^9 204*10^9];%(Pa) ...
    Modulus of Elasticity
Faow = ...
    (2+ao/W)*(.886+4.64*ao/W-13.32*(ao/W)^2+14.72*(ao/W)^3-5.6*(ao/W)^4)/((1-ao/W)^1.5);
```

```
yts = [6.02*10^8 6.02*10^8 6.02*10^8 6.02*10^8 6.02*10^8 5.86*10^8 ...
    5.86*10^8 5.86*10^8 5.86*10^8 6.02*10^8 6.02*10^8 6.02*10^8 ...
    6.02*10^8 6.02*10^8 10.96*10^8 10.96*10^8 10.96*10^8 10.96*10^8 ...
    10.96*10^8 10.92*10^8 10.92*10^8 10.92*10^8 10.92*10^8 ...
    10.92*10^8 10.96*10^8 10.96*10^8 10.96*10^8 10.96*10^8 ...
    10.96*10^8]; %(Pa) yield strength
uts = [9.32*10^8 9.32*10^8 9.32*10^8 9.32*10^8 9.32*10^8 8.11*10^8 ...
    8.11*10^8 8.11*10^8 8.11*10^8 9.32*10^8 9.32*10^8 9.32*10^8 ...
    9.32*10^8 9.32*10^8 1.365*10^9 1.365*10^9 1.365*10^9 1.365*10^9 ...
    1.365*10^9 1.306*10^8 1.306*10^8 1.306*10^8 1.306*10^8 ...
    1.306*10^8 1.365*10^9 1.365*10^9 1.365*10^9 1.365*10^9 ...
    1.365*10^9]; %(Pa) ultimate strength
%a_optical = [0.012686  0.012846    0.013119    0.012913    ...
    0.012927    0.01325 0.012958    0.012647    0.013219    ...
    0.012662    0.012806    0.012948    0.013214    0.012809    ...
    0.012594    0.012821    0.012693    0.012659    0.012451    ...
    0.012665    0.012586    0.012784    0.012673    0.012572    ...
    0.012585    0.012769    0.012613    0.012751    0.012488    ...
    0.01275];
sigy = (yts+uts)/2; %(Pa) average of yts and uts



% Look for Mat files
dats=dir('*.dat');

%% One Big For Loop
for n=1:length(dats)
    close all
    clear data;
    FileName=dats(n).name;
    PathName=pwd;
```

```
    File = FileName(1:findstr(FileName,'.')-1);
    Ext = FileName((findstr(FileName,'.')+1):length(FileName));

    k = strfind(PathName,'\');
    figTitle = PathName(k(end-1)+1:k(end)-1);

    us=strfind(figTitle,'_'); % Find Underscores
    figTitle(us)=' '; % Replace Underscores with Spaces

    %% Prep File for Import
    columnNums=4;
    columnFormat=repmat('%f ',1,columnNums);

    headerlines = 5;
    blockLines = 4;
    fid=fopen([PathName '\' FileName],'r');

        block=1;
        for m=1:headerlines;
            tline = fgetl(fid);
        end

        while ~feof(fid);
            tline = fgetl(fid);
            sline = sscanf(tline, columnFormat)';

            if isempty(sline)==0
                data(block,1:columnNums) = sscanf(tline, columnFormat)';
                block = block + 1;
            end
        end
    fclose(fid);
```

```


    %% Assign Data


    time   = data(:,1); % s
    disp  = data(:,2)/1E3; % mm->m
    cmod   = data(:,3)/1E3; % mm->m
    force   = data(:,4); % N


    %% Calculate Crack Length, alpha for front face cmod ASTM 647 ...
       Fig A1.4
    ux = (1+(sqrt(E(n)*B(n)*cmod./force))).^(-1);

aW = 1.0010 + -4.6695*ux + 18.460*ux.^2 + -236.82*ux.^3 + ...
    1214.9*ux.^4  + -2143.6*ux.^5 ;
a = aW.*W(n); %(m) crack length
b = W(n)-a; %(m) remaining ligament

%% Rotation correction
Ci = cmod./force;
H = .007; %m
Ri = (W+a)/2;
D = .0025; %m
theta = asin((D+cmod./2)./sqrt(D^2 + Ri.^2)) - atan(D./Ri);

Cci = Ci./((H*sin(theta)./Ri - cos(theta)).*(D*sin(theta)./Ri - ...
    cos(theta)));

%% Re-Calculate Crack Length, alpha for front face cmod ASTM 647 Fig ...
    A1.4
```

```
    ux2 = (1+(sqrt(E(n)*B(n)*Cci))).^(-1);

aW2 = 1.0010 + -4.6695*ux2 + 18.460*ux2.^2 + -236.82*ux2.^3 + ...
    1214.9*ux2.^4  + -2143.6*ux2.^5 ;
a2 = aW2.*W(n); %(m) crack length
b2 = W(n)-a2; %(m) remaining ligament

%% J-integral calculation

[xData, yData] = prepareCurveData( cmod, force );
ft = fittype( 'poly7' );
[fitresult, gof] = fit( xData, yData, ft );

fx = fitresult(cmod);

Apl = cumtrapz(cmod,fx);


%% Apply down sample data here to fix
J = 2*(Apl)./(B(n)*b);

da=(a-min(a));

    cline = 2*sigy(n)*da;
    cline015 = 2*sigy(n)*da - 0.00015*(2*sigy(n));
    cline02 = 2*sigy(n)*da - 0.0002*(2*sigy(n));
    cline15 = 2*sigy(n)*da - 0.002*(2*sigy(n));

    plot(da,J,'.-');
    hold on
    plot(da,cline)
    hold on
```

```
plot(da,cline015)
hold on
plot(da,cline02)
hold on
plot(da,cline15)
title('J vs Crack Extension')
xlabel('Crack Extension (m)')
ylabel('J J/m^2')
hold off

axis([0 max(da) 0 max(J)]);


%% Auto Trim the Data on the Left hand side

jThresh=0.25E5;jThreshIdx=find(J>jThresh);
xA=min(da(jThreshIdx));

Jold=J;
daOld=da;

da=da(jThreshIdx); % Trim the Data
J=J(jThreshIdx);% Trim the Data
da0=da-xA; %shift the data

cline = 2*sigy(n)*da;
cline015 = 2*sigy(n)*da - 0.00015*(2*sigy(n));
cline02 = 2*sigy(n)*da - 0.0002*(2*sigy(n));
cline15 = 2*sigy(n)*da - 0.0015*(2*sigy(n));

plot(da0,J,'.-');
%axis([0 5*10^-3 0 5*10^5])
```

```
axis([0 max(da) 0 max(J)])
hold on
plot(da,cline)
hold on
plot(da,cline015)
hold on
plot(da,cline02)
hold on
plot(da,cline15)
title('J vs Crack Extension')
xlabel('Crack Extension (m)')
ylabel('J J/m^2')
hold off
grid on

%% Power Law fit

[intercept015,interceptIdx015]=min(abs(J-cline015));
[intercept15,interceptIdx15]=min(abs(J-cline15));

fitIdx = interceptIdx015:interceptIdx15;

axis([0 max(da) 0 max(J)]);


[xData, yData] = prepareCurveData(da(fitIdx), J(fitIdx));
pl = fittype( 'C1*(x/.001)^C2' );
[fitresult, gof] = fit( xData, yData, pl );

JQ = fitresult(da);
dai = JQ./(2*sigy) + 0.0002; % From ASTM 1820 A.9.6.6.2

```

```

PowerLaw = fit(da,JQ,pl,'StartPoint',[1,1]);
axis([0 5*10^-3 0 5*10^5]);

C1 = PowerLaw.C1;
C2 = PowerLaw.C2;

JQi = C1*(dai/0.001).^C2; % From ASTM 1820 A.9.6.6.3




%% Calculate intercept
% Find min Value of PVForce-Force (smallest value = intercept)
% *Small Difference since lines are fitted
[interceptValue,interceptIdx]=min(abs(JQ-cline02));

JQintercept=JQ(interceptIdx);

for ii = 1:length(a)-1;
   if abs(JQi(ii+1)-JQi(ii)) <= 0.02*JQi(ii+1);
      JIC = JQi(ii);
      break
   end
end

KJIC = (E(n)*JIC/(1-v^2))^.5; % From ASTM 1820 A.9.11

%% Store mat file of all data
goAway=strfind(File,' '); % Find Spaces
File(goAway)=''; % Remove Spaces
eval(['save ' File]);
```

```
    %% Plots of CMOD vs Force
% figure(n)
%     fig1=plot(cmod*1000,force/1000,'.')
%     title([FileName(1:end-18)], 'interpreter', 'none')
%     xlabel('CMOD (mm)')
%     ylabel('Force (kN)')
%     xlim([0 3.5])
%     ylim([0 35])
%     %legend('Location','southeast','MHT','CHT','AB')
%     grid on
%     saveas(fig1, [FileName(1:end-18), 'cmodforce.jpg'])


end
```

B.2 MATLAB Code for FCGR Testing

```
clc,clear,close all
%% Batch process
%Vectors with individual values for each specimen.
a_optical = [0.012777   0.013529    0.013315    0.013421    ...
    0.013287    0.013649    0.013559    0.013537    0.013338    ...
    0.013463    0.01342 0.01339 0.013459    0.013437    0.013757    ...
    0.013511    0.013488    0.013552    0.013566    0.01342 ...
    0.013459    0.013517    0.014062    0.013446    0.013615    ...
    0.013249    0.013426    0.013448    0.013427    0.014357    ...
    0.013861    0.013712    0.013389    0.013533    0.013517    ...
    0.013846    0.014767    0.013298    0.013436    0.013462    ...
    0.013748    0.014655    0.013425    0.013468    0.014104];
a_fracture = [0.022012667   0.022115667 0.021444333 0.021732667 ...
    0.021702667 0.021518    0.021767333 0.021327333 0.021453333 ...
```

```
    0.021596    0.021599333 0.021268    0.021518    0.021493667 ...
    0.021498    0.022110667 0.022015333 0.022329    0.022269333 ...
    0.02217 0.022367667 0.022153667 0.021938667 0.022245333 ...
    0.022545    0.022031667 0.022135667 0.022005    0.022738    ...
    0.021984333 0.021616333 0.022074667 0.022020333 0.022017333 ...
    0.022178333 0.023714667 0.022576333 0.022635    0.022287    ...
    0.022860333 0.02175 0.022411    0.020382    0.021944    ...
    0.022032667];
W = [25.54  25.6    25.45   25.45   25.42   25.55   25.51   25.43   ...
    25.45   25.39   25.48   25.48   25.44   25.49   25.47   25.38   ...
    25.37   25.52   25.45   25.44   25.47   25.41   25.45   25.45   ...
    25.39   25.37   25.5    25.48   25.46   25.47   25.38   25.5    ...
    25.38   25.51   25.39   25.29   25.36   25.37   25.4    25.3    ...
    25.37   25.31   25.37   25.37   25.51];
B = [12.35  12.63   12.61   12.67   12.64   12.64   12.65   12.65   ...
    12.66   12.62   12.63   12.6    12.63   12.62   12.58   12.63   ...
    12.63   12.63   12.63   12.63   12.64   12.62   12.64   12.63   ...
    12.62   12.63   12.63   12.63   12.63   12.62   12.65   12.65   ...
    12.62   12.66   12.66   12.65   12.65   12.67   12.67   12.67   ...
    12.68   12.65   12.66   12.67   12.65];
E = [1.66*10^11 1.66*10^11 1.66*10^11 1.66*10^11 1.66*10^11 ...
    1.13*10^11 1.13*10^11 1.13*10^11 1.13*10^11 1.13*10^11 ...
    1.66*10^11 1.66*10^11 1.66*10^11 1.66*10^11 1.66*10^11 204*10^9 ...
    204*10^9 204*10^9 204*10^9 204*10^9 207*10^9 207*10^9 207*10^9 ...
    207*10^9 207*10^9 204*10^9 204*10^9 204*10^9 204*10^9 204*10^9 ...
    208*10^9 208*10^9 208*10^9 208*10^9 208*10^9 205*10^9 205*10^9 ...
    205*10^9 205*10^9 205*10^9 208*10^9 208*10^9 208*10^9 208*10^9 ...
    208*10^9];%(Pa) Modulus of Elasticity
yts =[6.02*10^8 6.02*10^8 6.02*10^8 6.02*10^8 6.02*10^8 5.86*10^8 ...
    5.86*10^8 5.86*10^8 5.86*10^8 5.86*10^8 6.02*10^8 6.02*10^8 ...
    6.02*10^8 6.02*10^8 6.02*10^8 10.96*10^8 10.96*10^8 10.96*10^8 ...
    10.96*10^8 10.96*10^8 10.92*10^8 10.92*10^8 10.92*10^8 ...
```

```
    10.92*10^8 10.92*10^8 10.96*10^8 10.96*10^8 10.96*10^8 ...
    10.96*10^8 10.96*10^8 1236*10^6 1236*10^6 1236*10^6 1236*10^6 ...
    1236*10^6 1138*10^6 1138*10^6 1138*10^6 1138*10^6 1138*10^6 ...
    1236*10^6 1236*10^6 1236*10^6 1236*10^6 1236*10^6]; ; %(Pa) ...
    yield strength


specimen_number = 1

a_optical = a_optical(specimen_number); %m - optical crack length ...
    measurements at 1000 cycles
a_fracture = a_fracture(specimen_number); %m -crack length at fracture
W = W(specimen_number)/1000; %m - Specimen Thickness
B = B(specimen_number)/1000; %m
E = E(specimen_number); %modulus Pa
yts = yts(specimen_number); %yield strength Pa

lowfilter = 0.0001;
highfilter = 0.0005;

P = 3000; %peak Load in N

%% User Picks File to Convert
[FileName,PathName] = uigetfile('*.dat*','Select the data file');
File = FileName(1:findstr(FileName,'.')-1);
Ext = FileName((findstr(FileName,'.')+1):length(FileName));

k = strfind(PathName,'\');
figTitle = PathName(k(end-1)+1:k(end)-1);

us=strfind(figTitle,'_'); % Find Underscores
figTitle(us)=' '; % Replace Underscores with Spaces
```

```

if exist([pwd '\' File '.mat']) ==2
    load([File '.mat']); % Load Pre-Existing Matlab
    fprintf('Load Pre-Existing Matlab\n');
else
   fprintf('Load Dat File\n');
   % Pre-Allocate Memory
   data=NaN*ones(1E7,7);
   % Prep File for Import
   headerlines = 5;
   blockLines = 4;
   fid=fopen([PathName '\' FileName],'r');

       block=1;
       for m=1:headerlines
           tline = fgetl(fid);
       end

       while ~feof(fid)
           tline = fgetl(fid);
           sline = sscanf(tline, '%f %f %f %f %f %f %f')';

           if isempty(sline)==0
               data(block,1:5) = sscanf(tline, '%f %f %f %f %f %f ...
                  %f')';
               block = block + 1;
           end
       end
   fclose(fid);
   disp(['Successfully Read      ' PathName FileName])

   % Save Loaded Dat file in Native Matlab Format
```

```
    save(File);
 end

%% Trim and Assign Data
% Account for Nan's
tf=isnan(data); % Binary Matrix of NaN's

% Remove Data with No Cycles
cycles = data(:,5)/2;
idxCycles=find(cycles<1);
data(idxCycles,:)=[]; % Remove All Data with No cycles

time   = data(:,1); % s
disp  = data(:,2); % mm
force   = data(:,3); % N
cmod   = data(:,4)/1E3; % mm->m
segments = data(:,5);

[cmodMax,cmodMaxIdx] = findpeaks(cmod);



[cmodMin,cmodMinIdx] = findpeaks(-cmod);
cmodMin=-cmodMin; % push back to original values.

%used to adjust the length of the matrix to match cmodMin, uncomment ...
   both
%       lines below
%cmodMax=cmodMax(1:end-1); % trim off last entry of Value (since ...
   diff trims data by 1)
%cmodMaxIdx=cmodMaxIdx(1:end-1); % trim off last entry of Value ...
    (since diff trims data by 1)
```

```

%used to adjust the length of the matrix to match cmodMax, uncomment ...
    both
%   lines below
%cmodMin=cmodMin(1:end-1); % trim off last entry of Value (since ...
    diff trims data by 1)
%cmodMinIdx=cmodMinIdx(1:end-1); % trim off last entry of Value ...
    (since diff trims data by 1)



Dcmod = (cmodMax - cmodMin)./(force(cmodMaxIdx)-force(cmodMinIdx));


%% Initial Crack Length Calculation

ux = ((E*Dcmod*B).^.5 + 1).^-1;

a = W*(1.0010 - 4.6695*ux + 18.460*ux.^2 - 236.82*ux.^3 + ...
    1214.9*ux.^4 - 2143.6*ux.^5);

%% Solver function to find elastic constraint modulus
[Eprime,difference]=elastic_constraint_solver_dcmod_func(E,W,B,P,Dcmod(segments(2000)),

%% Initial Crack Length Calculation

ux_prime = ((Eprime*Dcmod*B).^.5 + 1).^-1;

a_prime = W*(1.0010 - 4.6695*ux_prime + 18.460*ux_prime.^2 - ...
    236.82*ux_prime.^3 + 1214.9*ux_prime.^4 - 2143.6*ux_prime.^5);


```

```
max_Cycles=segments(cmodMaxIdx)/2;





%% Increase range between points to 0.1mm

clear a_short
m=1;
d=2;
a_short1(1) = a_prime(1);
for i = 10000:length(a_prime)
    if (a_prime(i)-a_prime(m) > lowfilter) && (a_prime(i)-a_prime(m) ...
          < highfilter)
        a_short1(d) = a_prime(i);

        m = i;
        shortCycles(d)= max_Cycles(i);
        d=d+1;
    end
end

a_short1(end+1) = a_prime(end);
shortCycles(end+1) = max_Cycles(end);
a_short1 = transpose(a_short1);
shortCycles = transpose(shortCycles);

%% Linearize with optical measurements

acorr = [a_optical a_fracture];
acmod = [a_short1(1) a_short1(end)];
```

```

[xData, yData] = prepareCurveData( acorr, acmod );

% Set up fittype and options.
ft = fittype( 'poly1' );

% Fit model to data.
[fitresult, gof] = fit( xData, yData, ft );

a_short = fitresult(a_short1);

%% Delta K calculations
for i = 1:length(a_short)-1
alpha(i) = 0.5*(a_short(i)+a_short(i+1))/W;
end
dP=2700; % Force Range - Difference between max/min Force
shortdK = ...
    dP*(2+alpha).*(0.866+4.64*alpha-13.32*(alpha).^2+14.72*(alpha).^3-5.6*(alpha).^4)./(
shortdK = transpose(shortdK);
Kmax = ...
    P*(2+alpha).*(0.866+4.64*alpha-13.32*(alpha).^2+14.72*(alpha).^3-5.6*(alpha).^4)./(B

ligament = (4/pi)*(Kmax/yts).^2;
ligreq = (W-a_short(1:end-1));
test = ligreq-transpose(ligament);


dadn=diff(a_short)./diff(shortCycles);

fig = loglog(shortdK/(10^6),dadn,'.');
grid on
title(FileName(1:end-4), 'Interpreter', 'none')
```

```
xlabel('\DeltaK (MPa m^{(1/2)})')
ylabel('da/dN (m/cycle)')
xlim([1 1000])
ylim([10^-10 10^-5])
set(gcf,'position',[10,10,400,600])






save(strcat(FileName,'done.mat'))
```

Bibliography

[1] W. Callister, *Materials Science and Engineering: An Introduction (2nd Edition)*, vol. 12. Wiley, 1991.

[2] G. K. Bouse, “Application of a Modified Phase Diagram to the Production of Cast Alloy 718 Components,” *Metallurgy and Applications*, pp. 69 – 79, 1989.

[3] L. University, “About Additive Manufacturing.”

[4] D. J. Newell, *Solution Anneal Heat Treatments to Enhance Mechanical Performance of Additively Manufactured IN718.* PhD thesis, Air Force Institute of Technology, Wright Patterson AFB, 2018.

[5] T. L. Anderson, *Fracture Mechanics - Fundamentals and Applications.* Taylor and Francis, 3 ed., 2005.

[6] A. Fatemi, “Fundamentals of Lefm and Applications to Fatigue Crack Growth,” *University of Toledo*, p. 133, 2010.

[7] E. R. Sadiku, G. Phiri, T. Jayaramudu, K. Sudhakar, L. Moropeng, M. C. Khoathane, T. A. Adegbola, and W. K. Kupolati, “Mechanisms of Toughening in Nanostructured Polymer Blends,” *Design and Applications of Nanostructured Polymer Blends and Nanocomposite Systems*, no. December, pp. 365–384, 2015.

[8] G. Cobb, “Scan Strategy Effects on Microstructure and Hardness of SLM IN718,” in *Materials Science and Technology* (R. O’Hara, ed.), (Columbus Ohio), AFIT, 2018.

[9] A. E399-17, “ASTM E399-17,” *Annual Book of ASTM Standards*, pp. 1–33, 2011.

[10] D. N. Mohamed (2015), “Fracture Mechanics Based Fatigue and Fracture Toughness Evaluation of SLM Ti-6Al-4V,” Tech. Rep. May, University of Cape Town, Cape Town, South Africa, 2015.

[11] ASTM E1820-17a, “Standard Test Method for Measurement of Fracture Toughness 1,” *Standardization*, no. April 2000, pp. 1–56, 2017.

[12] A. E647-15, “ASTM E647 - Standard Test Method for Measurement of Fatigue Crack Growth Rates,” *ASTM Book of Standards*, vol. 03, no. July, pp. 1–49, 2016.

[13] R. Konecna, L. Kunz, G. Nicoletto, and A. Baca, “Fatigue Crack Growth Behavior of Inconel 718 Produced by Selective Laser Melting,” *Frattura ed Integrita Strutturale*, vol. 10, no. 36, pp. 36–45, 2016.

[14] ASTM B637, “B637 121: Standard Specification for Precipitation-Hardening and Cold Worked Nickel Alloy Bars , Forgings , and Forging Stock for Moderate or High Temperature Service 1,” *Astm*, no. Section 13, pp. 1–7, 2015.

[15] Additive Manufacturing Today, “SpaceX Uses DMLS to 3D Print Inconel SuperDraco Engine Chamber,” 2016.

[16] W. Marcus, “US Air Force Is Waiting a Year for Parts That It Could 3D-Print,” 2018.

[17] R. Schafrik, D. Ward, and J. Groh, “Application of Alloy 718 in GE Aircraft Engines: Past, Present and Next Five Years,” *Superalloys 718, 625, 706 and Various Derivatives (2001)*, pp. 1–11, 2001.

[18] L. Morris, “STUDY OF ABNORMAL GRAIN GROWTH IN BETA ANNEALED TI-6AL-4V FORGINGS,” tech. rep., Air Force Institute of Technology, 2018.

[19] B. Hutchinson, “Critical Assessment 16: Anisotropy in metals,” *Materials Science and Technology*, vol. 31, no. 12, pp. 1393–1401, 2015.

[20] A. Mostafa, I. Picazo Rubio, V. Brailovski, M. Jahazi, and M. Medraj, “Structure, Texture and Phases in 3D Printed IN718 Alloy Subjected to Homogenization and HIP Treatments,” *Metals*, vol. 7, no. 12, p. 315, 2017.

[21] B. Ahmad, S. O. van der Veen, M. E. Fitzpatrick, and H. Guo, “Residual Stress Evaluation in Selective-Laser-Melting Additively Manufactured Titanium (Ti-6Al-4V) and Inconel 718 Using the Contour Method and Numerical Simulation,” *Additive Manufacturing*, vol. 22, no. June, pp. 571–582, 2018.

[22] Miami Valley Materials Testing Center, “MVMTC Tensile Test Results,” tech. rep., Miami Valley Materials Testing Center, 2018.

[23] SAE International, “Heat Treatment Wrong Nickel Alloy and Cobalt Alloy Parts,” tech. rep., SAE International, 2016.

[24] P. C. Paris, M. P. Gomez, and W. E. Anderson, “A Rational Analytic Theory of Fatiuge,” 1961.

[25] Special Metals, “INCONEL alloy 718,” tech. rep., Special Metals, 2007.

[26] I. Nikulin, R. Kaibyshev, and V. Skorobogatykh, “High Temperature Properties of an Austenitic Stainless Steel,” *Journal of Physics: Conference Series*, vol. 240, 2010.

[27] Y. Sduwv, Z. Jhduv, N. H. V. Dlufudiw, D. Dqg, G. Dssolfdwlrqv, E. Iudphv, D. O. O. Whuudlq, R. Lqirupdwlrq, S. E. Wkh, O. Vvrfldwlrq, D. Q. G. Lv, and Q. R. W. Iru, “Al 7075 Fact Sheet,” tech. rep., Clinton Aluminum, 2018.

[28] K. N. Amato, S. M. Gaytan, L. E. Murr, E. Martinez, P. W. Shindo, J. Hernandez, S. Collins, and F. Medina, “Microstructures and Mechanical Behavior of Inconel 718 Fabricated by Selective Laser Melting,” *Acta Materialia*, vol. 60, no. 5, pp. 2229–2239, 2012.

[29] R. Konečná, G. Nicoletto, L. Kunz, and A. Bača, “Microstructure and Directional Fatigue Behavior of Inconel 718 Produced by Selective Laser Melting,” *Procedia Structural Integrity*, vol. 2, pp. 2381–2388, 2016.

[30] D. Krueger, “The Development of Direct Age 718 for Gas Turbine Engine Disk Applications,” *Superalloys 718 Metallurgy and Applications (1989)*, pp. 279–296, 1989.

[31] M. Slama, C Abdellaoui, “Structural Characterization of the Aged Inconel 718,” *Journal of Alloys and Compounds*, vol. 306, pp. 2–3, 2000.

[32] T. Gladman, “Precipitation Hardening in Metals,” *Materials Science and Technology*, vol. 15, no. 1, pp. 30–36, 1999.

[33] M. Jouiad, E. Marin, R. S. Devarapalli, J. Cormier, F. Ravaux, C. Le Gall, and J. M. Franchet, “Microstructure and mechanical properties evolutions of alloy 718 during isothermal and thermal cycling over-aging,” *Materials and Design*, vol. 102, pp. 284–296, 2016.

[34] Goldberg, “History of 3D Printing: It’s Older Than You Think,” 2018.

[35] K. Moussaoui, W. Rubio, M. Mousseigne, T. Sultan, and F. Rezai, “Effects of Selective Laser Melting Additive Manufacturing Parameters of Inconel 718 on Porosity, Microstructure and Mechanical properties,” *Materials Science and Engineering A*, vol. 735, no. April, pp. 182–190, 2018.

[36] AMETEK Metal Products, “Surface Finishes Datasheet,” 2014.

[37] D. M. Lambert and R. Jacobs, “Evaluation of the Effect of Surface Finish on High Cycles Fatigue fo SLM-IN718,” tech. rep., Marshall Space Flight Center, 2016.

[38] B. Stephenson, “What is Gorilla Glass?,” 2018.

[39] M. Ford, “How is Tempered Glass Made?,” 2001.

[40] D. Lambert, “IN718 Additive Manufacturing Properties and Influences,” *Additive Manufacturing Consortium Meeting*, no. June, pp. 1–23, 2014.

[41] D. Roylance, “Introduction to Fracture Mechanics,” tech. rep., Massachusetts Institute of Technology, Cambridge, MA, 2001.

[42] A. A. Griffith, “The Phenomena of Rupture and Flow In Solids,” *Philisophical Transactions of the Royal Society of London*, vol. 221, pp. 163–198, 1921.

[43] G. R. Irwin, “Analysis of Stresses and Strains Near the End of a Crack Traversing a Plate,” *Applied Mechanics Division Summer Conference, ASME*, pp. 361–364, 1957.

[44] J. R. Rice, “Mathematical Analysis in the Mechanics of Fracture,” *Mathematical Fundamentals*, vol. 2, pp. 191–311, 1968.

[45] J. R. Rice and G. F. Rosengren, “Plane Strain Deformation Near a Crack Tip in a Power-Law Hardening Material,” *Journal of the Mechanics and Physics of Solids*, vol. 16, no. 1, pp. 1–12, 1968.

[46] S. Ramsey, “Basic Fracture Mechanics,” 2013.

[47] D. H. Herring, “Grain Size and Its Influence on Material Properties,” *The Heat Treat Doctor*, no. August, pp. 1–2, 2005.

[48] B. Pieraggi and J. Uginet, "Fatigue and Creep Properties in Relation with Alloy 718 Microstructure," *Superalloys 718, 625, 706 and Various Derivatives (1994)*, pp. 535–544, 1994.

[49] W. L. Li and J. C. Li, "The Effect of Grain Size on Fracture Toughness," *Philosophical Magazine A: Physics of Condensed Matter, Structure, Defects and Mechanical Properties*, vol. 59, no. 6, pp. 1245–1261, 1989.

[50] W. J. Mills, "Fracture Toughness of Thermally Aged Alloy 718 Weld Metal," *Welding Research Supplement*, vol. 324, pp. 1451–1457, 1987.

[51] D. Krueger, S. Antolovich, and R. Van Stone, "Effects of Grain Size and Precipitate Size on the Fatigue Crack Growth Behavior of Alloy 718 at 427 °C," *Metallurgical Transactions A*, vol. 18A, no. August, pp. 1431–1449, 1987.

[52] T. M. Mower, "Degradation of Titanium 6Al-4V Fatigue Strength due to Electrical Discharge Machining," *International Journal of Fatigue*, vol. 64, pp. 84–96, 2014.

[53] N. David, O. Ryan, C. Gregory, P. Anthony, K. Michael, B. Larry, and H. Joshua, "Mitigation of Scan Strategy Effects and Material Anisotropy Through Supersolvus Annealing in LPBF IN718.," in *Materials Science and Technology*, (Columbus Ohio), pp. 8–9, 2018.

[54] K. Shi, L. Cai, Y. Hu, D. Salmon, and C. Bao, "Experimental Estimation of J Resistance Curves From Load-CMOD Record for FFCT Specimens," *Journal of Testing and Evaluation*, vol. 44, no. 6, p. 20140173, 2016.

[55] V. Sharma, V. Dikwakar, K. S. Kumar, B. N. Rao, and P. SD, "A Simple J-Integral Approach for Fracture Toughness Assessment on Invalid Test Data of

Standard CT Specimens," *Trends in Applied Sciences Research*, vol. 2, pp. 132–143, 2006.

[56] J. M. Larsen, J. R. Jira, and K. S. Ravichandran, "Measurement of Small Cracks by Photomicroscopy: Experiments and Analysis," *Small-Crack Test Methods, ASTM STP 1149*, pp. 57–80, 1992.

[57] S. Suresh, *Fatigue of Materials.* Cambridge, UK: Press Syndicate of the University of Cambridge, 2nd ed., 2003.

[58] K. America, "Wide Area 3D Measurement System Head."

[59] W. J. Mills, "Fracture Toughness Variations for Alloy 718 Base Metal and Welds," *Superalloy 718 - Metallurgy and Applications*, pp. 517–532, 1989.

[60] S. R. Lampman, *ASM Handbook: Volume 19: Fatigue and Fracture.* Materials Park, OH: ASM International, 1 ed., 1996.

REPORT DOCUMENTATION PAGE

Form Approved
OMB No. 0704–0188

1. REPORT DATE *(DD–MM–YYYY)*
21-03-2019

2. REPORT TYPE
Master's Thesis

3. DATES COVERED *(From — To)*
Sept 2018 — 21 March 2019

4. TITLE AND SUBTITLE

Fracture Toughness and Fatigue Crack Growth Rate of Inconel 718
Formed by Laser Powder Bed Fusion

5a. CONTRACT NUMBER

5b. GRANT NUMBER

5c. PROGRAM ELEMENT NUMBER

6. AUTHOR(S)

Hohnbaum Charles C. , Captain

5d. PROJECT NUMBER

5e. TASK NUMBER

5f. WORK UNIT NUMBER

7. PERFORMING ORGANIZATION NAME(S) AND ADDRESS(ES)

Air Force Institute of Technology
Graduate School of Engineering and Management (AFIT/EN)
2950 Hobson Way
WPAFB OH 45433-7765

8. PERFORMING ORGANIZATION REPORT NUMBER

AFIT-ENY-MS-19-M-310

9. SPONSORING / MONITORING AGENCY NAME(S) AND ADDRESS(ES)

AFIT/ENY
Att: Maj Ryan O'Hara
2950 Hobson Way
WPAFB OH 45433
ryan.ohara@afit.edu

10. SPONSOR/MONITOR'S ACRONYM(S)

AFIT/EN

11. SPONSOR/MONITOR'S REPORT NUMBER(S)

12. DISTRIBUTION / AVAILABILITY STATEMENT

DISTRIBUTION STATEMENT A:
APPROVED FOR PUBLIC RELEASE; DISTRIBUTION UNLIMITED.

13. SUPPLEMENTARY NOTES

This material is declared a work of the U.S. Government and is not subject to copyright protection in the United States.

14. ABSTRACT

Continuing improvement in the field of AM of metals provides the opportunity for direct fabrication of aerospace parts. AM was once used in large part for rapid prototyping but improvements in technology and increases in the knowledge base of AM materials has provided the opportunity for manufacture of AM parts for operational use. The ability to create low numbers of unique parts without having to invest in expensive tooling provides great economic incentive to utilize this technique. IN718 is the most common high temperature alloy used in the aerospace industry and lends itself readily to formation by LPBF. The superior strength of IN718 at temperatures up to 650°C and its excellent corrosion resistance make it the alloy of choice for compressor blades in jet turbines. Extensive data exists for conventionally produced IN718 but gaps in the data are present for AM material. Two of these gaps that are addressed by this research are FT and FCGR. A primary driver of the differences in behavior between conventionally manufactured and AM IN718 are the microstructural differences. Conventionally produced material has an equiaxed microstructure that provides isotropic material behavior. Conversely production by AM methods results in a highly directional microstructure related to the build direction of the part that drives anisotropy in material performance. It is hypothesized that a modified heat treatment that allows for re-crystallization of the columnar grains to grains that are more equiaxed will mitigate anisotropic material effects. This research will characterize the FCGR of AB, CHT, and MHT conditions. Results of FCGR indicate the the MHT is successful at reducing the overall FCGR of LPBF IN718. The standard heat treatment for wrought IN718 is shown to increase anisotropy in FCGR and give no improvement to the FCGR when compared to material in the AB condition.

15. SUBJECT TERMS

Inconel 718; IN718; Fracture Toughness; Fatigue Crack Growth Rate; Build Direction; Laser Powder Bed Fusion, Selective Laser Melting, Additive Manufacturing

16. SECURITY CLASSIFICATION OF:			**17. LIMITATION OF ABSTRACT**	**18. NUMBER OF PAGES**	**19a. NAME OF RESPONSIBLE PERSON**
a. REPORT	**b. ABSTRACT**	**c. THIS PAGE**			Maj Ryan O'Hara, AFIT/ENY
					19b. TELEPHONE NUMBER *(include area code)*
U	U	U	UU	83	(937)255-3636, x4542; ryan.ohara@afit.edu